CHARACTERIZATION OF HETEROGENEOUS MEDIA WITH MULTICOMPONENT LASER ULTRASONICS

by

Thomas E. Blum

A dissertation

submitted in partial fulfillment

of the requirements for the degree of

Doctor of Philosophy in Geophysics

Boise State University

May 2013

BOISE STATE UNIVERSITY GRADUATE COLLEGE

DEFENSE COMMITTEE AND FINAL READING APPROVALS

of the dissertation submitted by

Thomas E. Blum

Dissertation Title: Characterization of Heterogeneous Media with Multicomponent Laser Ultrasonics

Date of Final Oral Examination: 10 December 2012

The following individuals read and discussed the dissertation submitted by student Thomas E. Blum, and they evaluated his presentation and response to questions during the final oral examination. They found that the student passed the final oral examination.

Kasper van Wijk, Ph.D.	Chair, Supervisory Committee
Mark D. Schmitz, Ph.D.	Member, Supervisory Committee
Hans-Peter Marshall, Ph.D.	Member, Supervisory Committee
Dmitri Tenne, Ph.D.	Member, Supervisory Committee
Laura Pyrak-Nolte, Ph.D.	External Examiner

The final reading approval of the dissertation was granted by Kasper van Wijk, Ph.D., Chair of the Supervisory Committee. The dissertation was approved for the Graduate College by John R. Pelton, Ph.D., Dean of the Graduate College.

ACKNOWLEDGMENTS

First and foremost, I would like to thank Dr. Kasper van Wijk for the support, patience, and leadership he has given me throughout my journey at Boise State University. This collaboration made the past four and a half years a very enriching experience at both a personal and professional level. I would also like to extend my sincere appreciation to the members of the Physical Acoustics Laboratory for their enduring support and camaraderie over the years. A very special thanks goes to Dylan Mikesell, Andy Lamb, and Mila Adam, for their many contributions to my research and writing, as well as their everlasting friendship.

Much of my time at Boise State was supported and funded by a research grant from ConocoPhillips, and I would like to thank Dr. Phil Anno and Dr. Mark Willis for this opportunity. I would also like to extend my appreciation to Bossa Nova Technologies, in particular Dr. Bruno Pouet and Alexis Wartelle, for their assistance in funding the beginning of my research and providing technical help with this two component sensor.

I would like to express many thanks to my committee members, Dr. Hans-Peter Marshall, Dr. Dmitri Tenne, and Dr. Mark Schmitz, for their commitment and diligence in helping me compose and improve this manuscript. I also thank Dr. Roel Snieder from Colorado School of Mines, who welcomed me for a short stay in his

group and helped me grasp scattering theory, as well as Dr. John Scales and Dr. Martin Smith for fruitful discussions about processing and experimental aspects of my work. Most of this experimental work would not have been possible without the help of Randy Nuxoll, from the BSU machine shop, who helped me build the sample holder, and whatever else I needed.

Finally, I would like to thank my family, especially my parents, Suzanne and Dominique, and my brothers, Benoît and Clément, for accepting and supporting my choice to study abroad. Last but not least, I would not have enjoyed this experience nearly as much without all the help and support from Amaya, who cared for me during long evenings and weekends of work, and did a tremendous job editing my writing, including this very manuscript.

ABSTRACT

Wave propagation in scattering media is a complicated topic, but scattered elastic waves carry important information about the internal structure of the medium. It is a current topic of research and for the foreseeable future. Advances in theory and applications described in this manuscript benefit from new ways to collect more densely sampled, multicomponent, true-amplitude data.

Thus far, most fracture characterization experiments in the laboratory involve contacting transducers as elastic wave sources and receivers. Similarly, rock properties such as anisotropy and attenuation are also measured with contacting techniques. These type of measurements are well-suited for time-of-flight measurements, but for scattering experiments issues arise. These include coupling issues between transducers and sample, ringing of the mechanical transducer, time-consuming steps to repeat the measurements with different source/receiver locations, and the relatively large sensor size. As a result, contacting techniques are less than ideal to the study of heterogeneous and anisotropic media.

In this work, we show that contacting devices can successfully be replaced by remote laser ultrasonic sources and receivers. Using fully non-contact measurement techniques, we are able to avoid the aforementioned drawbacks, acquire high-quality laboratory data with dense source and/or receiver locations, and with computer-

controlled acquisition that is fully automated and takes on the order of hours to complete.

First, we describe the experimental setup used throughout this work to acquire laboratory data on small-scale samples. We show that using a novel laser interferometer design allows us to measure two components of the elastic displacement field. Combined with a laser source, this results in a fully non-contacting system that makes automated scanning acquisition possible with a source/receiver footprint small compared to the wavelength.

Second, we study a single fracture, whose size is comparable to the elastic wavelength, in an otherwise homogeneous medium. In a first step, we apply the linear slip model to a single finite planar fracture under the Born approximation. We derive new expressions for the scattering amplitude in the frequency domain and illustrate this theoretical work with a laboratory experiment. We measure the scattering amplitudes and estimate the compliance of a single fracture generated in a clear plastic sample, which shows good agreement between the theoretical and experimental results. We also show that the laser-based experimental setup allows us to directly excite elastic waves at a fracture inside a solid sample. We measure the associated displacement field, and use tip diffractions to estimate the size of the fracture.

Finally, we investigate the properties of an anisotropic medium with vertical transverse isotropic (VTI) symmetry. We can accurately measure the P-wave arrival along a dense range of angles, but also the S-wave arrival, for selected directions. We therefore estimate the elastic constants and Thomsen parameters of the medium, as well as the attenuation anisotropy. This series of results demonstrate the potential of laser-based ultrasonics for laboratory measurements. In particular, we are able to rapidly

acquire high-quality, densely sampled data in situations where contacting transducers would introduce issues related to their size, and ringing. These findings pave the way for wider use of laser ultrasonics in rock physics applications.

TABLE OF CONTENTS

LIST OF FIGURES

LIST OF TABLES

CHAPTER 1:

INTRODUCTION

Characterizing the elastic properties of complex media with elastic waves is a challenging problem. Nevertheless, elastic waves propagating through either non-scattering or scattering materials carry important information about their internal structure.

Generally, heterogeneities vary in size, but scatterers on the order of a wavelength are an especially difficult topic. For example, faults and fractures are important features of the subsurface. They can act as conduits or barriers to fluid flow of hydrocarbons, water, and magma (Haney *et al.*, 2005; Brandsdóttir and Einarsson, 1979). Changes in the fracture system lead to changes in scattered waves (Groenenboom and Fokkema, 1998; Groenenboom and van Dam, 2000; Pyrak-Nolte, 2000), as well as wave attenuation and seismic anisotropy. Collettini *et al.* (2009) show that the mechanical properties of fractures and fault zones are related to the fabric and microstructure of these features. Understanding the interaction of fractures with elastic waves is crucial in order to characterize fracture properties remotely.

Historically, fractures have been studied for two end-member situations. When the fracture size is small compared to the elastic wavelength, wave propagation is expressed in terms of effective medium theory (Crampin, 1981; Hudson, 1981).

Changes in fracturing lead to changes in coda waves as well as attenuation and seismic anisotropy. Conversely, large fractures compared to the wavelength are treated like regular interfaces, and are characterized by their reflection and transmission coefficients (Pyrak-Nolte *et al.*, 1990b; Pyrak-Nolte and Nolte, 1992; Zhu and Snieder, 2002). On the other hand, for multiple sets of parallel fractures that are small compared to the dominant wavelength, wave propagation can be expressed in terms of effective medium theory (Crampin, 1981; Hudson, 1981; Schoenberg and Sayers, 1995; Schoenberg and Douma, 1988). This theory accounts for an effective velocity and attenuation across many parallel slip interfaces. Pyrak-Nolte *et al.* (1990b) show that waves in such a medium are dispersive in nature and present laboratory anisotropy measurements in agreement with effective medium theory. In the case of an effective medium, fracture information can be obtained from laboratory measurements of rock properties, including velocity and attenuation anisotropy (Hsu and Schoenberg, 1993; Kachanov and Sevostianov, 2005).

Traditionally, laboratory measurements of elastic rock properties in general, whether they intend to characterize fractures, attenuation, or anisotropy, are done using strain gages at low frequencies (in the seismic range, up to a few tens of Hz), or, at ultrasonic frequencies, with contact transducers (Pyrak-Nolte *et al.*, 1990b; Groenenboom and Falk, 2000). Such laboratory setups allow for measurements in load cells, or under confining pressure. However, their contacting character makes them subject to coupling issues, rending experiments involving multiple sources and receiver locations very time-consuming. Moreover, piezoelectric transducers at ultrasonic frequencies have a narrow frequency response, and are sometimes prone to ringing. Their size is often in the order of the wavelength, so they can act as scatterers themselves. Trans-

ducers can also be used remotely in water-based experiments, where water is used as a couplant between the studied material and the sources and receiver. In this case, the wavefield is not strictly measured at the sample surface, but rather a some short distance away from it. To avoid some of these challenges, elastic waves in the ultrasonic range can be generated and detected using laser beams. Laser sources and receivers are marginally used for seismic modeling (Pouet and Rasolofosaon, 1990; Bretaudeau *et al.*, 2011), and anisotropy estimation (Lebedev *et al.*, 2011). These measurements involve a laser source that generates elastic waves via thermal expansion, and a laser interferometer as a receiver.

In this dissertation, we use and advance this technique, known as laser ultrasonics, and apply it to rock properties measurements and fracture characterization. Unprecedented data quality allowed us to push advances in understanding fractures and anisotropic materials. Each of the chapters is briefly introduced next.

1.1 Laser Generation and Detection of Ultrasounds

The development and characterization of the two-component laser interferometer used throughout this work is detailed in Chapter 2. The majority of it is published as Blum *et al.* (2010). We first describe how the laser ultrasonic interferometer collects light scattered away from the angle of incidence to provide the absolute ultrasonic displacement for both the out-of-plane and an in-plane component. We then calibrate this new system by measuring the radial and vertical polarization of a Rayleigh wave in an aluminum half-space. The estimated amplitude ratio of the horizontal and vertical

displacement agrees well with the theoretical value. The phase difference exhibits a small bias ($\sim 10\%$) between the two components due to a different frequency response between the two processing channels of the prototype electronic circuitry. The acquisition of a line scan with the interferometer moving away from the Rayleigh wave source demonstrates the scanning capabilities of the laboratory setup.

1.2 Scattered Waves from a Single Fracture

Chapter 3 first introduces an analytic expression of the scattering amplitude of circular fractures under some assumptions, and then describes the experimental results confirming the theoretical results. It is for the most part published as Blum *et al.* (2011b). While previous analytic descriptions of scattering mostly deal with very large or very small fractures (compared to the dominant wavelength), in this chapter we present an analytic solution for the scattering of elastic waves from a fracture of arbitrary size. Based on the linear-slip model for a dry fracture, we derive the scattering amplitude in the frequency domain under the Born approximation for all combinations of incident and scattered wave modes. We then verify the theory by performing laser-based ultrasonic laboratory measurements of a single fracture in clear plastic. Our analytic results match the experimental data, and allow us to estimate the orientation of the fracture, as well as quantify the normal component of its compliance.

1.3 Scattering Amplitude of a Single Fracture under Load

In Chapter 4, we show that with a well-designed, non-contact experiment, we can measure the amplitude of the displacement field scattered by a disk-shaped crack, without and with static load. Moreover, by looking at both the P- to P-wave and S- to S-wave scattering modes, we estimate the size, orientation, and both normal and tangential components of the compliance of the crack, again assuming a linear-slip behavior under the conditions described in Chapter 3. Finally, we show that by increasing uniaxial static stress in the plane of the fracture, the normal compliance decreases linearly.

1.4 Laser Excitation of a Fracture Source for Elastic Waves

Beyond the study of scattering by the fracture of an incoming elastic wave, in Chapter 5, published as Blum *et al.* (2011a), we show that elastic waves can be directly excited at a fracture inside a transparent sample. Indeed, by focusing laser light directly onto this fracture, we generate an internal source of elastic waves. The associated displacement field, measured by our laser interferometer, has pronounced waves that are diffracted at the fracture tips. We confirm that these are tip diffractions from direct excitation of the fracture by comparing them with tip diffractions from scattered elastic waves excited on the exterior of the sample, as in the previous chapters. Being able to investigate fractures — in this case, in an optically-transparent material

— via direct excitation opens the door to more detailed studies of fracture properties in general.

1.5 Measurements of the Elastic Properties of Shales

Finally, we present a laser-based, non-contacting method to measure elastic anisotropy of horizontal shale cores. We estimate the elastic constants c_{11}, c_{33}, and c_{55} directly from ultrasonic waveforms, and c_{13} from a least-squares fit of estimated to modeled group velocities. Significant P-wave velocity and attenuation anisotropy in dry shales are almost surely exaggerated by delamination of clay platelets and microfracturing, but provide an illustration of the new measurement technique. While challenges lie ahead to measure preserved shales at *in situ* conditions in the future, we discuss the fundamental advantages of the proposed method over more traditional laboratory measurements involving contact transducers. Chapter 6 is published as Blum *et al.* (2013).

CHAPTER 2:

LASER GENERATION AND DETECTION OF ULTRASOUNDS

2.1 Introduction

Ultrasonic measurements are commonly used in scaled modeling for seismology. Contacting piezoelectric transducers have traditionally been used as both source and receiver, but using these can result in mechanical ringing and variations in coupling. In addition, transducers are on the order of the size of the resonant wavelength, which can make them scatter the wavefield. Laser-based ultrasound has become an alternative non-contacting technique to transducers (Scruby and Drain, 1990). Ultrasonic laser interferometers and vibrometers have a broadband response, going from kHz to GHz or more, and a sub-millimeter spot size. Since these laser-based sensors do not require physical coupling, one can scan a surface under computer control.

Generating elastic waves is done by illuminating a solid sample with a high-energy pulsed laser. We use a Q-switched Nd:YAG laser, generating a pulse of ≈ 15 ns at a wavelength of 1064 nm. When an energy pulse from the laser hits an optically absorb-

ing surface, part of that energy is absorbed and converted into heat. The resulting localized heating causes thermal expansion, which in turn results in elastic waves in the ultrasonic range (Scruby and Drain, 1990). The laser source has a repetition rate of up to 8 Hz and generates highly repeatable pulses. The temperature distribution resulting from localized laser heating is extensively described in Section 5.2 of Scruby and Drain (1990). In particular, Figure 5.3 shows that in metals, the temperature rise is steep, but then decreases to less than half the maximum within a time on the order of the pulse length. In any case, the temperature increase due to a laser pulse at the time just prior to the following pulse is on the order of a few hundredth of a Kelvin, and we therefore neglect the temperature increase of the sample in the following experiments.

Typically, only the out-of-plane component of the wavefield is recorded with laser-based ultrasonic sensors. Nishizawa *et al.* (1998) performed two mutually orthogonal laser measurements at 45° incidence in addition to a normally incident measurement to get the in-plane component of the wavefield. Cand *et al.* (1994), on the other hand, used a two-channel confocal Fabry-Perot interferometer and collected scattered light in two symmetrical directions with respect to the plane of normal incidence. Here, we show that a new interferometer design allows the detection of both the out-of plane and the horizontal in-plane displacement components, simultaneously. As an example, we describe calibration measurements of the Rayleigh wave in a large aluminum sample.

2.2 Description of the Sensor

The laser ultrasonic receiver is based on a constant-wave laser generating a stable 250 mW beam at a wavelength of 532 nm. The beam is split into a probe beam, which is reflected by the sample surface, and a reference beam, which follows a fixed optical path inside the device. The reference and object beam are combined in a photo-refractive crystal to form a real-time hologram that diffracts each beam into the direction of the other beam.

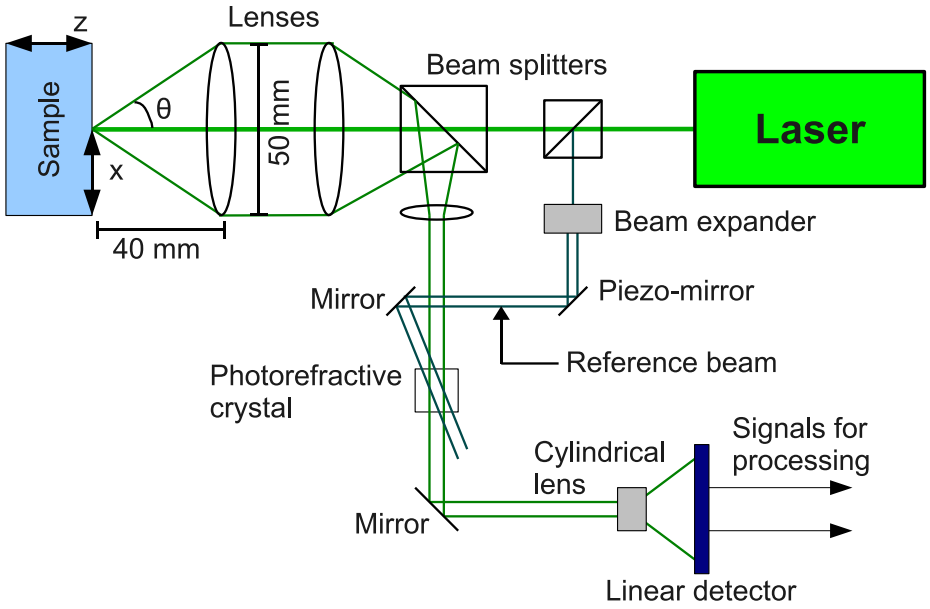

Figure 2.1: A diagram of the optical setup.

The optical setup is shown in Figure 2.1. We take advantage of the roughness of the material surface by collecting the light scattered away from the angle of incidence, which carries information on the in-plane displacement. After the reference and probe wavefront interfere in the photo-refractive crystal, the circular beam goes through a cylindrical lens and is imaged on a linear 16-element photodiode. The optical setup is symmetric, so that elements can be treated in pairs corresponding to the same

absolute angle. We number the elements $e_{\pm i}$ with $i = 1$ for the center pair and $i = 8$ for the outside pair; positive-numbered elements belong to one half of the photo diode and negative-numbered elements to the other. Each detector element corresponds to an angle θ_i at which the collected light is scattered by the sample surface. Since out-of-plane motion is symmetric with respect to the probe beam axis, but in-plane motion is asymmetric, the motion recorded by the element e_i is $s_{\pm i} = \cos(\theta_i)u_z \pm \sin(\theta_i)u_x$, where u_z and u_x are the displacements along the (out-of-plane) z-axis and (horizontal in-plane) x-axis.

For small angles θ_i, we find that

$$\begin{aligned} u_z &= (s_i + s_{-i})/(2\cos(\theta_i)) \approx (s_i + s_{-i})/2 \\ u_x &= (s_i - s_{-i})/(2\sin(\theta_i)) \approx (s_i - s_{-i})/2\theta_i. \end{aligned}$$

As a result, the out-of-plane displacement is obtained by summing over all elements. For the in-plane motion, each element pair is treated with a differential amplifier proportional to $1/\theta_i$, before the resulting signals are summed together.

To calibrate the measured particle displacements, a piezoelectric transducer mounted with a mirror introduces a known displacement at a low frequency f_c on the reference beam. This signal is band-pass filtered and feeds an amplification loop controlled by the reference voltage V_{ref}, to calibrate the in- and out-of-plane signals at 100 mV/nm.

2.3 Point Measurement

We measure the amplitude and phase of a Rayleigh wave in a homogeneous aluminum block (214 x 232 x 277 mm). Elastic waves are generated by the laser source. The

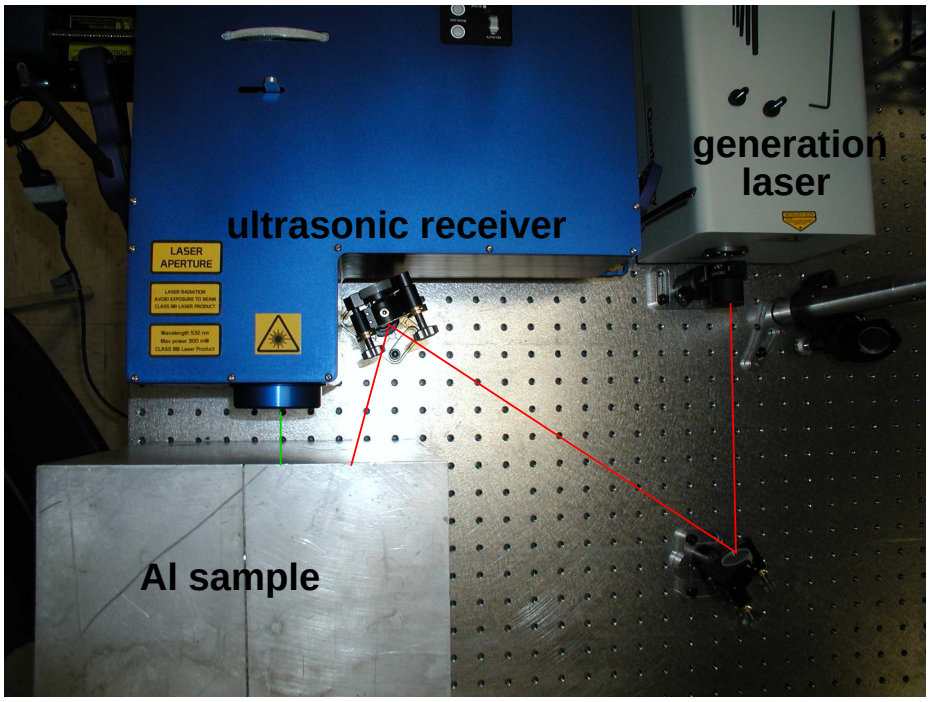

Figure 2.2: Top view of the experimental setup with the generation beam marked in red and the receiver beam in green.

source beam is partially focused, resulting in a circular source spot approximately 4 mm in diameter and 77 mm away from the receiver (Figure 2.2). We band-pass filter the signal between 300 and 900 kHz, so that all edges of the sample, as well as the source spot, are tens of wavelengths away. We therefore consider the detection to be in the far field, where the wave modes are fully established. The Rayleigh wave in this effectively homogeneous isotropic half-space is characterized by elliptical retrograde motion at the free surface; the horizontal and vertical components of the displacement are 90° out of phase. Furthermore, the ratio between the maximum amplitudes of the two components (the so-called H/V ratio) is $2\sqrt{1-c_x^2/\beta^2}/\left(2-c_x^2/\beta^2\right)$, where β is the shear wave velocity and c_x the Rayleigh wave velocity (Malischewsky and Scherbaum, 2004; Stein and Wysession, 2002). Based on our data and previous studies in this

sample, $\alpha = 6060$ m/s, $\beta = 3120$ m/s and $c_x = 2905$ m/s, resulting in an H/V ratio of 0.64.

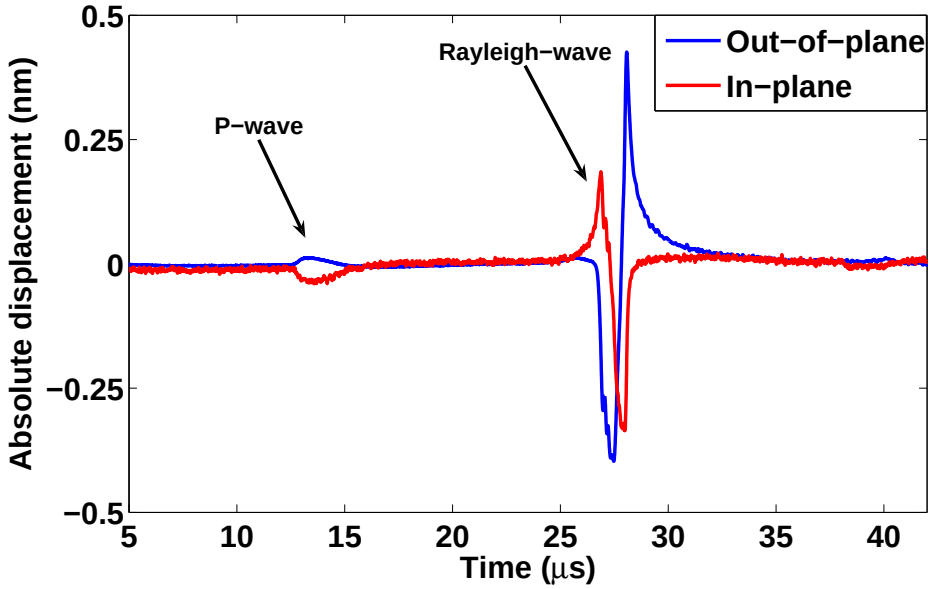

Figure 2.3: Unfiltered signal recorded by the interferometer 77 mm away from the source. Positive values are radially outward and up.

The absolute displacements from both channels are presented in Figure 2.3. We estimate the H/V ratio to be 0.64 ± 0.02 from the discrete amplitudes in the power spectrum and obtain the phase difference by subtracting the unwrapped phase angles of the complex part of the Fourier transform, similarly to Cand *et al.* (1994). However, the phase difference between the in- and out-of-plane wavefields is $97 \pm 1°$, a bias of 7°. All error bars represent the uncertainty at 2σ, where σ is the standard deviation in the phase and amplitude calculation over all frequencies, respectively. The most significant source of error in our H/V estimates is due to the in-plane signal, as described in details in Appendix A.

The phase offset originates from a difference in the frequency response between the electronic circuitry for calculation of the in-plane and out-of-plane signals, as

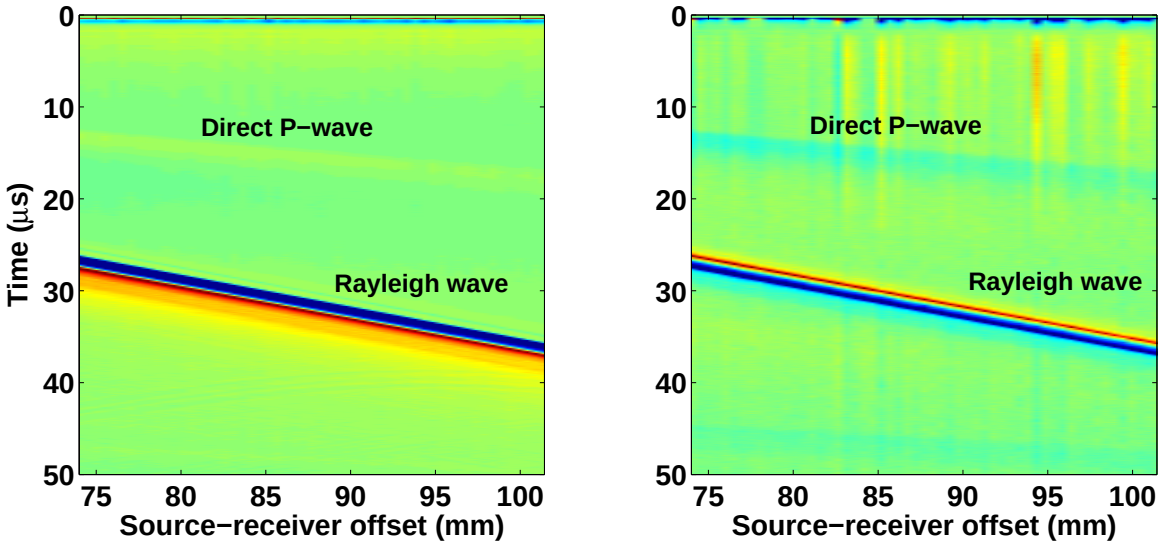

Figure 2.4: Line scan for the out-of-plane component (left), and the in-plane component (right).

explained previously. The phase difference might be eliminated by carefully matching the frequency response of both in-plane and out-of-plane circuits.

2.4 A Preliminary Line Scan

We place the receiver on a motorized stage to record the ultrasonic signals at source-detector offsets between 74 and 101 mm, acquired every half millimeter (Figure 2.4). Once we focus the beam in the center of the acquisition line, the entire scan is automatic and lasts on the order of minutes. Figure 2.5 displays an average H/V ratio of 0.63 ± 0.05, and a phase difference of $100 \pm 4°$. We attribute variations in the scan results to small variations in detector focus caused by a variable distance to the sample on the order of tens of μm. Because a large collecting angle is required for good in-plane sensitivity, it is critical to be well positioned at the focus to achieve accurate in-plane measurements. We measure this sensitivity to focus positioning in

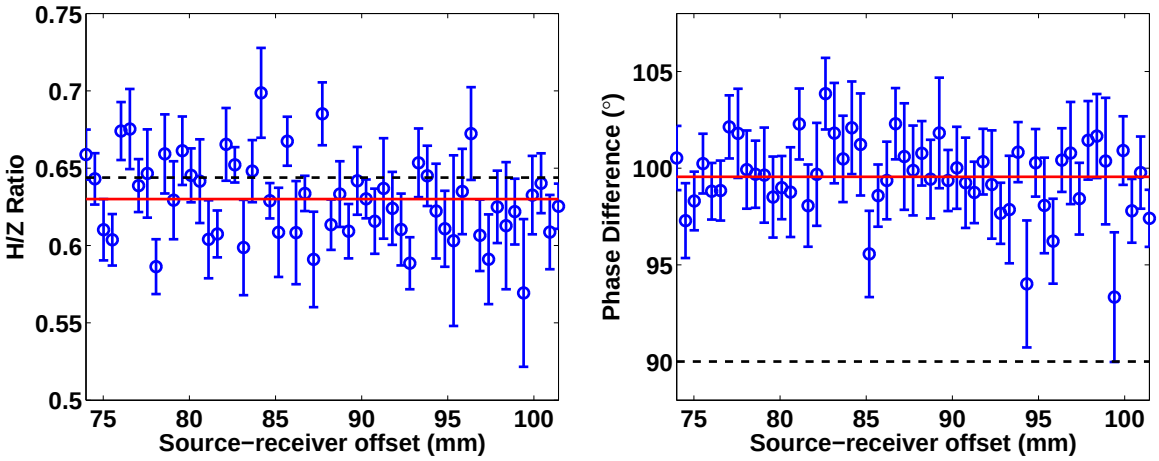

Figure 2.5: Amplitude ratio (left) and phase difference (right) as a function of source-detector offset. The average and theoretical values are plotted in red (solid line) and black (dashed line), respectively.

Appendix A.

2.5 Conclusion

A new laser interferometer takes advantage of the surface roughness of the sample for light to scatter away from the angle of the incident laser beam. The reflected light is recorded on a linear array of photo diodes, after which in- and out-of-plane particle displacements are determined. First results indicate that the amplitudes match theoretical calculations. The phase information is slightly biased because of a difference in the frequency response of electronic circuitry to measure in- and out-of-plane motion. The sensor allows for rapid scanning of the wavefield, which we will illustrate in the following chapters.

CHAPTER 3:

SCATTERED WAVES FROM A SINGLE FRACTURE

3.1 Introduction

Faults and fractures in the subsurface can act as conduits or barriers to fluid flow of hydrocarbons, water, and magma (Haney *et al.*, 2005; Brandsdóttir and Einarsson, 1979). Changes in fracturing lead to changes in coda waves as well as attenuation and seismic anisotropy. Collettini *et al.* (2009) show that the mechanical properties of fractures and fault zones are related to the fabric and micro-structure of these features. Understanding the interaction of fractures with elastic waves is crucial in order to characterize fracture properties remotely. In hydrocarbon reservoirs, hydraulic fractures are generated to stimulate production and can be monitored with active or passive sources (Wills *et al.*, 1992; Meadows and Winterstein, 1994). Moreover, scattered waves can be used as a tool for monitoring fracture growth and fracture evolution (Groenenboom and Fokkema, 1998; Groenenboom and van Dam, 2000; Pyrak-Nolte, 2000). Besides geophysical applications, scattering from fractures is

important in non-destructive testing applications (Langenberg *et al.*, 2002).

Gubernatis *et al.* (1977a) derive the general integral equation for an elastic scatterer, which they solve using the Born approximation (Gubernatis *et al.*, 1977b; Wu and Aki, 1985). Their work is based on a volumetric flaw with specified contrast in density and elastic properties. In contrast, the linear slip model handles planar fractures of negligible aperture by linking the discontinuity of the displacement field at the fracture plane to the traction at the slip interface (Schoenberg, 1980). This model can be directly applied to fractures with a spatial extent comparable to the wavelength. The extreme case where the fracture plane is infinite leads to frequency-dependent reflection and transmission coefficients (Pyrak-Nolte *et al.*, 1990b; Pyrak-Nolte and Nolte, 1992; Zhu and Snieder, 2002). The linear slip model is often used to describe dry fractures (Coates and Schoenberg, 1995), and can also be used for fluid-filled fractures (Wu *et al.*, 2005; Groenenboom and Falk, 2000). It was also investigated experimentally (Pyrak-Nolte *et al.*, 1992, 1996). In addition, Sánchez-Sesma and Iturrarán-Viveros (2001) use the Sommerfeld optical diffraction theory to derive an approximate analytic expression for the scattering of SH-waves by a planar fracture of finite width (or opening) and infinite length. Fang *et al.* (2010) present finite-difference numerical simulations of the scattering of P-waves by a finite circular fracture.

For multiple sets of parallel fractures of a small size compared to the dominant wavelength, wave propagation can be expressed in terms of effective medium theory (Crampin, 1981; Hudson, 1981; Schoenberg and Sayers, 1995; Schoenberg and Douma, 1988; Kachanov and Sevostianov, 2005). This theory accounts for an effective velocity and attenuation across many parallel slip interfaces. Pyrak-Nolte

et al. (1990a) show that waves in such a medium are dispersive in nature and present laboratory anisotropy measurements in agreement with effective medium theory.

Here, we apply the linear slip model to a single finite planar fracture under the Born approximation. From this, we develop an analytic expression for the general scattering amplitude without making assumptions about the fracture size or wavelength, and therefore are not restricted to small scatterers as used in earlier studies (e.g., Gubernatis *et al.* 1977b; Smyshlyaev and Willis 1994). We derive expressions for the scattering amplitude in the frequency domain for every combination of incoming and scattered body wave modes. We illustrate this theoretical work with a novel laboratory experiment by estimating the components of the compliance for a single crack generated in a clear plastic sample, and show that the measured scattering amplitude is explained by values of the compliance that are consistent with values reported in other studies.

3.2 General Expressions for Scattering by a Fracture

We present the derivation in a frequency domain formulation based on the following Fourier convention: $f(t) = \int F(\omega) e^{-i\omega t} d\omega$. For brevity, we do not make the frequency-dependence explicit, and use the Einstein summation convention. We first derive a general expression of the wave scattered by a fracture of arbitrary size. The stress across the fracture is continuous, but the displacement across the fracture is not necessarily continuous. We denote the discontinuity in the displacement by $[\mathbf{u}]$. According to Equation (3.2) of Aki and Richards (2002), the displacement at location

$\mathbf{x}$ due to the discontinuity of the displacement at the fracture Σ is given by

$$u_n(\mathbf{x}) = \iint_{\Sigma} [u_i(\mathbf{s})]\, c_{ijkl} f_j G_{nk,l}(\mathbf{x}, \mathbf{s}) d^2 s \ , \tag{3.1}$$

where $\iint_{\Sigma}(\cdots)d^2s$ denotes the integration over the surface of the fracture, $\hat{\mathbf{f}}$ is the normal vector to the fracture as shown in Figure 3.1, c_{ijkl} is the elasticity tensor, and $G_{nk,l}$ is the gradient of the displacement Green's function defined as

$$G_{nk,l}(\mathbf{x}, \mathbf{s}) = \frac{\partial G_{nk}(\mathbf{x}, \mathbf{s})}{\partial s_l} \ . \tag{3.2}$$

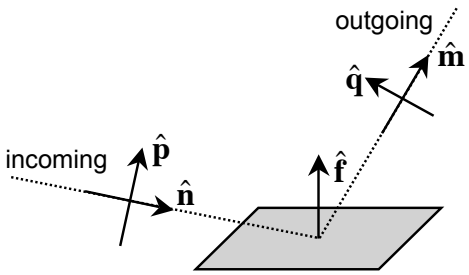

Figure 3.1: Definition of the normal vector $\hat{\mathbf{f}}$ to the fracture (shaded), the directions $\hat{\mathbf{n}}$ and $\hat{\mathbf{m}}$ of the incoming wave and outgoing waves, respectively. These vectors are also the polarization vectors in case of P-waves. For S-waves, the polarization vectors of incoming and outgoing waves are $\hat{\mathbf{p}}$ and $\hat{\mathbf{q}}$, respectively.

We next relate the discontinuity in the displacement to the stress field. We follow Schoenberg (1980) and assume that the slip discontinuity is related to the traction $\mathbf{T}$ at the fracture by a compliance matrix η:

$$[u_i] = \eta_{ir} T_r \ . \tag{3.3}$$

Although this approximation may break down towards the edges of the fracture, it is

commonly used in geophysics and considered accurate in far-field (Wu *et al.*, 2005). Expressing the traction in the stress σ_{ij} and the normal vector to the fracture yields

$$[u_i] = \eta_{ir}\sigma_{rs}f_s \ , \tag{3.4}$$

hence

$$[u_i]\, c_{ijkl}f_j = \eta_{ir}f_s f_j c_{ijkl}\sigma_{rs} \ . \tag{3.5}$$

Renaming the indices ($r \to i$, $s \to j$, $i \to p$, $j \to q$) and inserting this result in Equation (3.1) gives

$$u_n(\mathbf{x}) = \iint_\Sigma \sigma_{ij}N_{ijkl}G_{nk,l}(\mathbf{x},\mathbf{s})d^2s \ , \tag{3.6}$$

with

$$N_{ijkl} = \eta_{pi}f_j f_q c_{pqkl} \ . \tag{3.7}$$

We assume that the properties of the fracture can be characterized by a normal compliance η_N and a shear compliance η_T. In that case, one can use a dyadic decomposition to write the compliance matrix as $\eta = \eta_N\hat{\mathbf{f}}\hat{\mathbf{f}}^T + \eta_T(\mathbf{I} - \hat{\mathbf{f}}\hat{\mathbf{f}}^T)$, where $\mathbf{I}$ is the identity matrix. This identity is, in component form, given by

$$\eta_{ij} = \eta_N f_i f_j + \eta_T\left(\delta_{ij} - f_i f_j\right) \ , \tag{3.8}$$

where δ_{ij} is the Kronecker delta. We show in Appendix C.1 that this compliance matrix in an isotropic medium gives

$$N_{ijkl} = \lambda\eta_N f_i f_j \delta_{kl} + 2\mu\left(\eta_N - \eta_T\right) f_i f_j f_k f_l + \mu\eta_T\left(\delta_{ik}f_j f_l + \delta_{il}f_j f_k\right) \ , \tag{3.9}$$

where λ and μ are the Lamé parameters. Inserting Equation (3.9) into Equation (3.6) does not give the scattered waves because Expression (3.6) constitutes an integral equation for the scattered field. (The stress σ_{ij} in the integrand of Equation (3.6) depends on the displacement field that we aim to compute.) We solve this integral equation in the Born approximation by replacing the stress in the right-hand side of Equation (3.6) by the stress $\sigma_{ij}^{(0)}$ for a P-or S-wave propagating through a homogeneous medium, depending on the type of incident wave. In that case, the scattered wave is given by

$$u_n(\mathbf{x}) = \iint_{\Sigma} \sigma_{ij}^{(0)} N_{ijkl} G_{nk,l}(\mathbf{x}, \mathbf{s}) d^2 s \ . \tag{3.10}$$

Since N_{ijkl} is known, we can solve the scattering problem using the Born approximation. Replacing the stress field σ_{ij} by the stress field $\sigma_{ij}^{(0)}$ of the incident wave is only valid when the perturbation of the stress state by the fracture is small. This is certainly not valid in the case of fluid-filled fractures, because for such fractures the shear traction vanishes at the fracture surface. For this reason, the theory presented here is only applicable to dry fractures.

Consider first an incoming plane P-wave that propagates in the $\hat{\mathbf{n}}$-direction (Figure 3.1). Since such a wave is polarized in the longitudinal direction,

$$\mathbf{u}^{(P)}(\mathbf{s}) = \hat{\mathbf{n}} e^{ik_\alpha(\hat{\mathbf{n}}\cdot\mathbf{s})} \ , \tag{3.11}$$

where

$$k_\alpha = \omega/\alpha \ , \tag{3.12}$$

with α the P-wave velocity and ω the angular frequency. For an isotropic medium

$\sigma_{ij} = \lambda\delta_{ij}\partial_k u_k + \mu(\partial_i u_j + \partial_j u_i)$ and the stress associated with this plane P-wave is

$$\sigma_{ij}^{(P)} = ik_\alpha \left(\lambda\delta_{ij} + 2\mu n_i n_j\right) e^{ik_\alpha(\hat{\mathbf{n}}\cdot\mathbf{s})} \ . \tag{3.13}$$

For a plane S-wave arriving from the $\hat{\mathbf{n}}$-direction and polarized in the $\hat{\mathbf{p}}$-direction (Figure 3.1), the displacement is given by

$$\mathbf{u}^{(S)}(\mathbf{s}) = \hat{\mathbf{p}} e^{ik_\beta(\hat{\mathbf{n}}\cdot\mathbf{s})} \ , \tag{3.14}$$

where

$$k_\beta = \omega/\beta \ , \tag{3.15}$$

and β is the S-wave velocity. The shear wave is transversely polarized, hence $(\hat{\mathbf{p}}\cdot\hat{\mathbf{n}}) = 0$. For an isotropic medium, the associated stress is given by

$$\sigma_{ij}^{(S)} = ik_\beta\mu \left(n_i p_j + n_j p_i\right) e^{ik_\beta(\hat{\mathbf{n}}\cdot\mathbf{s})} \ . \tag{3.16}$$

Inserting the stress (3.13) or (3.16) into Equation (3.10) gives the scattered field for incoming P- and S-waves, respectively.

3.3 Scattering Amplitudes

The scattered field can effectively be expressed by a scattering amplitude (Merzbacher, 1970). According to Expression (3.10), the scattered field depends on $G_{nk,l}$, which is the gradient of the Green's function. Expression (4.29) of Aki and Richards (2002) gives the gradient of the Green's function in the time domain for a homogeneous,

isotropic infinite space. Retaining the far-field terms only and replacing the time derivative with $-i\omega$ gives, in the frequency domain

$$G_{nk,l}(\mathbf{x},\mathbf{s}) = \frac{-i\omega m_k m_n m_l}{4\pi\rho\alpha^3 r} e^{ik_\alpha r} + \frac{-i\omega(\delta_{nk} - m_k m_n)m_l}{4\pi\rho\beta^3 r} e^{ik_\beta r} \ , \tag{3.17}$$

where the unit vector $\hat{\mathbf{m}}$ defines the direction of the outgoing wave (Figure 3.1) and $r = |\mathbf{x} - \mathbf{s}|$ denotes the distance between the observation point $\mathbf{x}$ and the integration point $\mathbf{s}$ on the fracture (Figure 3.2). In dyadic form, the term $(\delta_{nk} - m_k m_n)$ can be written as $\mathbf{I} - \hat{\mathbf{m}}\hat{\mathbf{m}}^T = \sum_{\text{pol}} \hat{\mathbf{q}}\hat{\mathbf{q}}^T$, where $\hat{\mathbf{q}}$ is the polarization of the outgoing S-wave (Figure 3.1), and $\sum_{\text{pol}}$ represents the sum over the two orthogonal shear wave polarizations perpendicular to the direction of the outgoing wave. With this replacement, Expression (3.17) can be written as

$$G_{nk,l}(\mathbf{x},\mathbf{s}) = \frac{-i\omega m_k m_n m_l}{4\pi\rho\alpha^3 r} e^{ik_\alpha r} + \frac{-i\omega \sum_{\text{pol}} q_n q_k m_l}{4\pi\rho\beta^3 r} e^{ik_\beta r} \ . \tag{3.18}$$

We choose the origin of our coordinate system near the center of the fracture, and denote the distance from the origin to the observation point by R (Figure 3.2). When this distance is large compared to the size of the fracture, we can approximate

$$r = R - (\hat{\mathbf{m}} \cdot \mathbf{s}) \ , \tag{3.19}$$

where $\hat{\mathbf{m}}$ is the unit vector from the center of the fracture to the observation point $\mathbf{x}$ (Figure 3.1), and $\mathbf{s}$ the location of the integration point on the fracture. Equation (3.18) varies most rapidly with r through the exponents e^{ikr}. For this reason, we replace r by Equation (3.19) in the exponents, and replace r in the denominator by

R. Inserting these results into Equation (3.10) gives the following expressions for the radiated P- and S-waves:

$$u_n^{(P)}(\mathbf{x}) = \iint_\Sigma \sigma_{ij}^{(0)} N_{ijkl} e^{-ik_\alpha(\hat{\mathbf{m}}\cdot\mathbf{s})} d^2s \left(\frac{-i\omega m_n m_k m_l}{4\pi\rho\alpha^3} \right) \frac{e^{ik_\alpha R}}{R} \ , \tag{3.20}$$

$$u_n^{(S)}(\mathbf{x}) = \iint_\Sigma \sigma_{ij}^{(0)} N_{ijkl} e^{-ik_\beta(\hat{\mathbf{m}}\cdot\mathbf{s})} d^2s \left(\frac{-i\omega \sum_{\text{pol}} q_n q_k m_l}{4\pi\rho\beta^3} \right) \frac{e^{ik_\beta R}}{R} \ . \tag{3.21}$$

In these expressions, $\sigma_{ij}^{(0)}$ is given by Equations (3.13) or (3.16), depending on whether the incoming wave is a P-wave or S-wave. We next define the scattering amplitude f for outgoing P- and S-waves by

$$u_n^{(P)}(\mathbf{x}) = f_{\cdot P} \frac{e^{ik_\alpha R}}{R} m_n \ , \tag{3.22}$$

$$u_n^{(S)}(\mathbf{x}) = \sum_{\text{pol}} f_{\cdot S} \frac{e^{ik_\beta R}}{R} q_n \ . \tag{3.23}$$

These equations are similar to the general expression of the scattering pattern in the far-field for a heterogeneous inclusion, such as Equation (6.72) in Martin (2006), see also Gubernatis *et al.* (1977a). Note the presence of the polarization vectors for both types of waves (m_n and q_n, respectively). In the following, $f_{P,P}$ is the scattering amplitude from a P-wave into a P-wave, $f_{S,P}$ is an S to P conversion, etc. Since the incoming wave in Equations (3.22) and (3.23) can still be either a P-wave or an S-wave, we use the dot ($\cdot$) in the first argument of the scattering amplitudes. A comparison with Equations (3.20) and (3.21) shows that the scattering amplitude is given by

$$f_{\cdot P} = \iint_\Sigma \sigma_{ij}^{(0)} N_{ijkl} e^{-ik_\alpha(\hat{\mathbf{m}}\cdot\mathbf{s})} d^2s \left(\frac{-i\omega m_k m_l}{4\pi\rho\alpha^3} \right) \ , \tag{3.24}$$

$$f_{.S} = \iint_{\Sigma} \sigma_{ij}^{(0)} N_{ijkl} e^{-ik_\beta(\hat{\mathbf{m}}\cdot\mathbf{s})} d^2s \left(\frac{-i\omega q_k m_l}{4\pi\rho\beta^3} \right) . \tag{3.25}$$

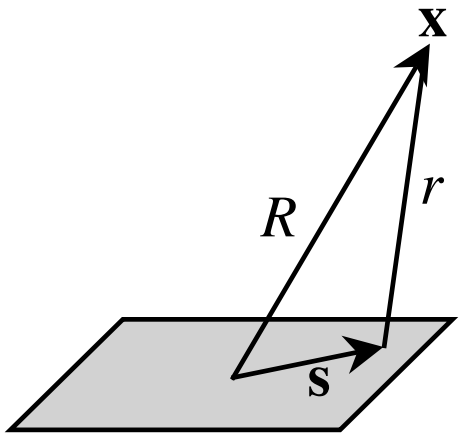

Figure 3.2: Definition of distance R between the observation point $\mathbf{x}$ and the center of the fracture, and the distance r between the observation point $\mathbf{x}$ and the integration point $\mathbf{s}$ on the fracture.

In the following expressions, it is convenient to use a form factor $F(\mathbf{k})$ that is defined as

$$F(\mathbf{k}) = \frac{\iint_{\Sigma} e^{i(\mathbf{k}\cdot\mathbf{s})} d^2s}{\iint_{\Sigma} d^2s} = A^{-1} \iint_{\Sigma} e^{i(\mathbf{k}\cdot\mathbf{s})} d^2s \, , \tag{3.26}$$

where A is the surface area of the fracture. Explicit expressions for the scattering amplitude follow by inserting Expressions (3.9) and (3.13) or (3.16) into the equations above. From here on, the polarization of the outgoing S-wave is explicitly defined along $\hat{\mathbf{q}}$, as shown in Figure 3.1. As shown in Appendix C.2, this gives the following

scattering amplitudes for the different types of scattering

$$\begin{aligned} f_{P,P}(\hat{\mathbf{n}};\hat{\mathbf{m}}) = \frac{\omega^2}{4\pi\rho\alpha^4} AF\left(k_\alpha(\hat{\mathbf{n}}-\hat{\mathbf{m}})\right)\Big\{&\lambda^2\eta_N + 2\lambda\mu\eta_N\left((\hat{\mathbf{n}}\cdot\hat{\mathbf{f}})^2+(\hat{\mathbf{m}}\cdot\hat{\mathbf{f}})^2\right)\\ &+4\mu^2(\eta_N-\eta_T)(\hat{\mathbf{n}}\cdot\hat{\mathbf{f}})^2(\hat{\mathbf{m}}\cdot\hat{\mathbf{f}})^2\\ &+4\mu^2\eta_T(\hat{\mathbf{n}}\cdot\hat{\mathbf{m}})(\hat{\mathbf{n}}\cdot\hat{\mathbf{f}})(\hat{\mathbf{m}}\cdot\hat{\mathbf{f}})\Big\}, \end{aligned} \tag{3.27}$$

$$\begin{aligned} f_{P,S}(\hat{\mathbf{n}};\hat{\mathbf{m}},\hat{\mathbf{q}}) = \frac{\omega^2}{4\pi\rho\alpha\beta^3}\mu AF\left(k_\alpha\hat{\mathbf{n}}-k_\beta\hat{\mathbf{m}}\right)\Big\{&2\lambda\eta_N(\hat{\mathbf{m}}\cdot\hat{\mathbf{f}})(\hat{\mathbf{q}}\cdot\hat{\mathbf{f}})\\ &+4\mu(\eta_N-\eta_T)(\hat{\mathbf{n}}\cdot\hat{\mathbf{f}})^2(\hat{\mathbf{q}}\cdot\hat{\mathbf{f}})(\hat{\mathbf{m}}\cdot\hat{\mathbf{f}})\\ &+2\mu\eta_T(\hat{\mathbf{n}}\cdot\hat{\mathbf{f}})\left((\hat{\mathbf{n}}\cdot\hat{\mathbf{q}})(\hat{\mathbf{m}}\cdot\hat{\mathbf{f}})+(\hat{\mathbf{n}}\cdot\hat{\mathbf{m}})(\hat{\mathbf{q}}\cdot\hat{\mathbf{f}})\right)\Big\}, \end{aligned} \tag{3.28}$$

$$\begin{aligned} f_{S,P}(\hat{\mathbf{n}},\hat{\mathbf{p}};\hat{\mathbf{m}}) = \frac{\omega^2}{4\pi\rho\alpha^3\beta}\mu AF\left(k_\beta\hat{\mathbf{n}}-k_\alpha\hat{\mathbf{m}}\right)\Big\{&2\lambda\eta_N(\hat{\mathbf{n}}\cdot\hat{\mathbf{f}})(\hat{\mathbf{p}}\cdot\hat{\mathbf{f}})\\ &+4\mu(\eta_N-\eta_T)(\hat{\mathbf{n}}\cdot\hat{\mathbf{f}})(\hat{\mathbf{p}}\cdot\hat{\mathbf{f}})(\hat{\mathbf{m}}\cdot\hat{\mathbf{f}})^2\\ &+2\mu\eta_T(\hat{\mathbf{m}}\cdot\hat{\mathbf{f}})\left((\hat{\mathbf{p}}\cdot\hat{\mathbf{m}})(\hat{\mathbf{n}}\cdot\hat{\mathbf{f}})+(\hat{\mathbf{n}}\cdot\hat{\mathbf{m}})(\hat{\mathbf{p}}\cdot\hat{\mathbf{f}})\right)\Big\}, \end{aligned} \tag{3.29}$$

$$\begin{aligned} f_{S,S}(\hat{\mathbf{n}},\hat{\mathbf{p}};\hat{\mathbf{m}},\hat{\mathbf{q}}) = \frac{\omega^2}{4\pi\rho\beta^4}\mu^2 AF\left(k_\beta(\hat{\mathbf{n}}-\hat{\mathbf{m}})\right)&\\ \times\Big\{4(\eta_N-\eta_T)(\hat{\mathbf{n}}\cdot\hat{\mathbf{f}})(\hat{\mathbf{p}}\cdot\hat{\mathbf{f}})(\hat{\mathbf{m}}\cdot\hat{\mathbf{f}})(\hat{\mathbf{q}}\cdot\hat{\mathbf{f}})&\\ +\eta_T(\hat{\mathbf{n}}\cdot\hat{\mathbf{q}})(\hat{\mathbf{p}}\cdot\hat{\mathbf{f}})(\hat{\mathbf{m}}\cdot\hat{\mathbf{f}})+\eta_T(\hat{\mathbf{n}}\cdot\hat{\mathbf{f}})(\hat{\mathbf{p}}\cdot\hat{\mathbf{q}})(\hat{\mathbf{m}}\cdot\hat{\mathbf{f}})&\\ +\eta_T(\hat{\mathbf{n}}\cdot\hat{\mathbf{m}})(\hat{\mathbf{p}}\cdot\hat{\mathbf{f}})(\hat{\mathbf{q}}\cdot\hat{\mathbf{f}})+\eta_T(\hat{\mathbf{n}}\cdot\hat{\mathbf{f}})(\hat{\mathbf{p}}\cdot\hat{\mathbf{m}})(\hat{\mathbf{q}}\cdot\hat{\mathbf{f}})\Big\}.& \end{aligned} \tag{3.30}$$

Note that the P to P scattering amplitude $f_{P,P}(\hat{\mathbf{n}};\hat{\mathbf{m}})$ depends only on the directions of incoming and outgoing waves, respectively, because these directions determine the polarization of the incoming and outgoing P-waves. In contrast, the P to S scattering amplitude $f_{P,S}(\hat{\mathbf{n}};\hat{\mathbf{m}},\hat{\mathbf{q}})$ depends explicitly on the polarization of the outgoing S-wave as well. This dependence of the S-wave polarization appears whenever an S-wave is

involved, either as incoming or outgoing wave. Expressions (3.27) through (3.30) do not change when $\hat{\mathbf{f}}$ is replaced by $-\hat{\mathbf{f}}$. This reflects the fact that both $\hat{\mathbf{f}}$ and $-\hat{\mathbf{f}}$ are normal to the fracture, and reversing the direction of the normal vector should not change the scattering of waves.

For all incoming and outgoing waves in Equations (3.27)–(3.30), the form factor (3.26) is evaluated at wavenumber $\mathbf{k}_{\text{in}} - \mathbf{k}_{\text{out}}$, where $\mathbf{k}_{\text{in}}$ is the wavenumber of the incoming wave and $\mathbf{k}_{\text{out}}$ is that of the outgoing wave. It may appear that $F(\mathbf{k}_{\text{in}} - \mathbf{k}_{\text{out}})$ violates reciprocity because it turns into its complex conjugate upon interchanging $\mathbf{k}_{\text{in}}$ and $\mathbf{k}_{\text{out}}$. Reciprocity is, however, not violated for the expressions of the scattered waves in Expressions (3.22) and (3.23). The exponential in these expressions is given by $\exp(i\mathbf{k}_{\text{out}}R)$, and the form factor contains another exponential $\exp\left(i(\mathbf{k}_{\text{in}} - \mathbf{k}_{\text{out}}) \cdot \mathbf{s}\right)$. The combination of the exponentials gives a total contribution $\exp\left(i\mathbf{k}_{\text{out}}R + i(\mathbf{k}_{\text{in}} - \mathbf{k}_{\text{out}}) \cdot \mathbf{s}\right)$. Using Expression (3.19), and using that $\mathbf{k}_{\text{out}} = k_{\text{out}}\hat{\mathbf{m}}$, the phase is given by $k_{out}r + \mathbf{k}_{\text{out}} \cdot \mathbf{s} + (\mathbf{k}_{\text{in}} - \mathbf{k}_{\text{out}}) \cdot \mathbf{s} = k_{out}r + \mathbf{k}_{\text{in}} \cdot \mathbf{s}$. This expression is the sum of the phase of the incident plane wave and the outgoing spherical wave for every integration point on the fracture, and the total scattered field obeys reciprocity.

3.4 Scattering by a Plane Crack

We next derive explicit expressions for the scattering amplitudes in terms of the directions of the incoming and scattered waves for the special case of a plane crack that is either small or circular. We define a crack to be "small" when the argument $(\mathbf{k} \cdot \mathbf{s})$ in Expression (3.26) is much smaller than 1. This is the case when

$$k_{\|}a \ll 1 \,, \tag{3.31}$$

where $k_\parallel$ is the absolute value of the component of $\mathbf{k}$ parallel to the crack, and a is the size of the crack. In Equation (3.28), the form factor is given by $F\left(k_\alpha \hat{\mathbf{n}} - k_\beta \hat{\mathbf{m}}\right)$. The incoming P-wave has wave number $k_\alpha \hat{\mathbf{n}}$, while the outgoing scattered S-wave has wave number $k_\beta \hat{\mathbf{m}}$. The difference $k_\alpha \hat{\mathbf{n}} - k_\beta \hat{\mathbf{m}}$ thus denotes the change in the wave number during the scattering. In Expressions (3.27)–(3.30), the form factor $F(\mathbf{k})$ is always evaluated at the wave number *change* during the scattering. Therefore, condition (3.31) does not necessarily imply that the fracture must be small compared to a wavelength. For example, for forward scattering of P-waves, $k_\parallel = k_\alpha(\hat{\mathbf{n}} - \hat{\mathbf{m}}) = 0$ in Expression (3.27), and condition (3.31) is satisfied for a fracture of any size. When condition (3.31) is satisfied, the exponent in Equation (3.26) can be ignored and

$$F(\mathbf{k}) = 1 \qquad \text{(small fracture)}. \tag{3.32}$$

We show in Appendix C.3 that for a circular fracture with radius a

$$F(\mathbf{k}) = \frac{2}{k_\parallel a} J_1(k_\parallel a) \qquad \text{(circular fracture)}, \tag{3.33}$$

where J_1 is the Bessel function of order 1. In the following, we retain $F(\mathbf{k})$, but Expressions (3.32) and (3.33) can be inserted for small cracks and circular cracks, respectively. According to Expression (11.5) of Arfken and Weber (2001), $J_1(x) = x/2 + O(x^2)$, hence Expression (3.33) reduces to Equation (3.32) for a small crack as $k_\parallel a \to 0$, and this holds independently of the incidence and scattering angles.

In order to express the scattering amplitude in the angles that define the incoming and outgoing waves, we must define these angles and the orientation of the fracture. We use a coordinate system where the z-axis is perpendicular to the fracture, and the

x-axis is chosen in such a way that the incoming wave propagates in the (x, z) plane coming from the $-x$ direction (Figure 3.3). The direction of the incoming wave makes an angle ψ with the z-axis, while the direction of the outgoing wave is defined by the angles θ and φ that are commonly used in a spherical coordinate system. Referring to Figure 3.3, this means that the vector normal to the fracture and the directions of incoming and outgoing waves are given by

$$\hat{\mathbf{f}} = \begin{pmatrix} 0 \\ 0 \\ 1 \end{pmatrix} \quad , \quad \hat{\mathbf{n}} = \begin{pmatrix} \sin\psi \\ 0 \\ \cos\psi \end{pmatrix} \quad , \quad \hat{\mathbf{m}} = \begin{pmatrix} \cos\varphi \sin\theta \\ \sin\varphi \sin\theta \\ \cos\theta \end{pmatrix} . \tag{3.34}$$

For a circular crack, these angles determine $k_{\|}$. For example, for P to S scattering, it follows from Expression (3.28), the definition of $k_{\|}$, and Equation (3.34) that

$$k_{\| \, P,S} = (k_\alpha \hat{\mathbf{n}} - k_\beta \hat{\mathbf{m}})_{\|} = \sqrt{(k_\alpha \sin\psi - k_\beta \cos\varphi \sin\theta)^2 + (k_\beta \sin\varphi \sin\theta)^2} \, . \tag{3.35}$$

In the following, we do not make this dependence on the angles explicit, but it should be kept in mind that for a circular crack one needs to account for the directions of incoming and outgoing waves in $F(\mathbf{k})$.

We next specify the polarization vectors for shear waves. Using the terminology for layered media, we define a polarization vector $\hat{\mathbf{q}}^{SH}$ to be parallel to the fracture (Figure 3.4). Following Figures 3.3 and 3.4, the polarization vector for the SH-wave satisfies

$$\hat{\mathbf{q}}^{SH} = \begin{pmatrix} -\sin\varphi \\ \cos\varphi \\ 0 \end{pmatrix} . \tag{3.36}$$

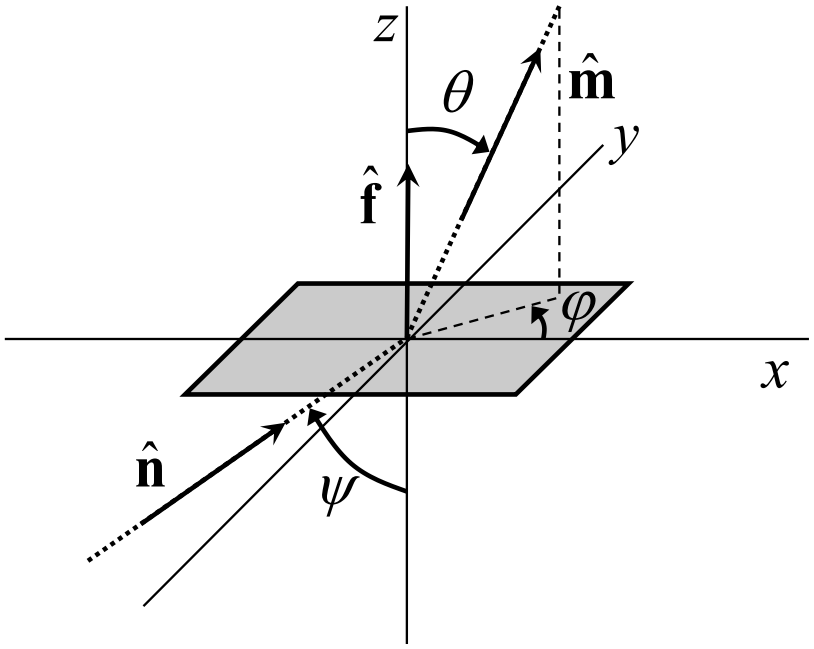

Figure 3.3: Definition of angles for incoming and outgoing waves from a fracture (shaded area).

The other S-wave polarization ($\hat{\mathbf{q}}^{SV}$) is oriented in the plane spanned by the normal vector $\hat{\mathbf{f}}$ and the propagation direction $\hat{\mathbf{m}}$ (Figure 3.4), and is given by

$$\hat{\mathbf{q}}^{SV} = \hat{\mathbf{m}} \times \hat{\mathbf{q}}^{SH} = \begin{pmatrix} -\cos\varphi\cos\theta \\ -\sin\varphi\cos\theta \\ \sin\theta \end{pmatrix} . \tag{3.37}$$

Since the fracture is finite, the label SH should not be taken to mean that the shear wave with this polarization is decoupled from the SV polarization and the P-waves. Indeed, the diffraction from the edges of the fracture contributes to non-zero scattering amplitudes $f_{SH,P}$ and $f_{SH,SV}$. The polarization vectors from incoming shear waves

follow from Expressions (3.36) and (3.37); by replacing $\varphi \to 0$ and $\theta \to \psi$, this gives

$$\hat{\mathbf{p}}^{SH} = \begin{pmatrix} 0 \\ 1 \\ 0 \end{pmatrix} \quad , \quad \hat{\mathbf{p}}^{SV} = \begin{pmatrix} -\cos\psi \\ 0 \\ \sin\psi \end{pmatrix} \quad . \tag{3.38}$$

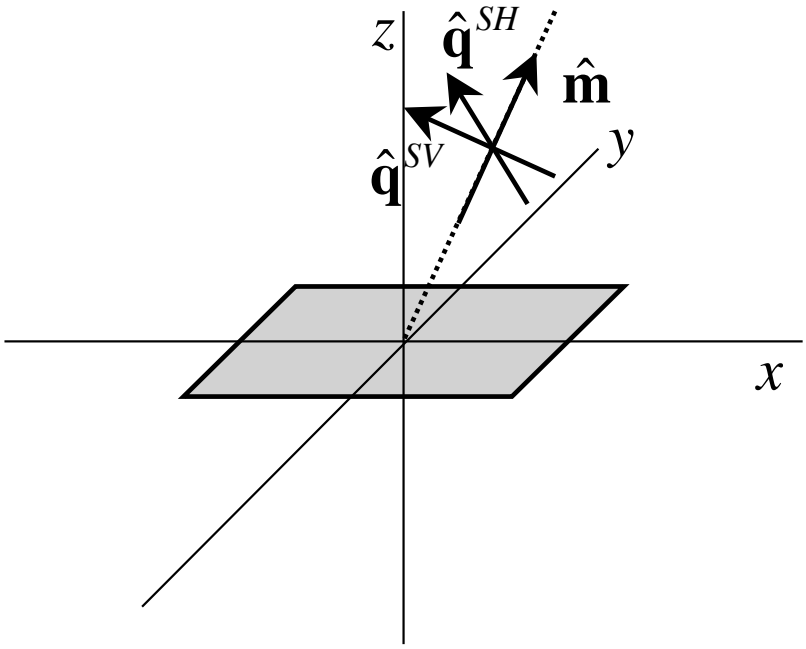

Figure 3.4: Polarization vectors for outgoing shear waves.

Inserting the direction vectors (3.34) and polarization vectors (3.36) and (3.37) into Expressions (3.27) through (3.30) gives the angular dependence of the scattering amplitude. The scattering amplitude, which is different for the two S polarizations,

is given by

$$f_{P,P}(\hat{\mathbf{n}};\hat{\mathbf{m}}) = \frac{\omega^2}{4\pi\rho\alpha^4} AF\left(k_\alpha(\hat{\mathbf{n}}-\hat{\mathbf{m}})\right) \times \Big\{(\lambda+\mu)^2\eta_N + (\lambda+\mu)\mu\eta_N\left(\cos 2\psi + \cos 2\theta\right) + \mu^2\eta_N \cos 2\psi\cos 2\theta + \mu^2\eta_T \sin 2\psi \sin 2\theta\cos\varphi\Big\} \ , \tag{3.39}$$

$$f_{P,SH}(\hat{\mathbf{n}};\hat{\mathbf{m}},\hat{\mathbf{q}}) = \frac{\omega^2}{4\pi\rho\alpha\beta^3} AF\left(k_\alpha\hat{\mathbf{n}} - k_\beta\hat{\mathbf{m}}\right) \times \Big\{-\mu^2\eta_T \sin 2\psi\cos\theta\sin\varphi\Big\} \ , \tag{3.40}$$

$$f_{P,SV}(\hat{\mathbf{n}};\hat{\mathbf{m}},\hat{\mathbf{q}}) = \frac{\omega^2}{4\pi\rho\alpha\beta^3} AF\left(k_\alpha\hat{\mathbf{n}} - k_\beta\hat{\mathbf{m}}\right) \times \Big\{(\lambda+\mu)\mu\eta_N \sin 2\theta + \mu^2\eta_N\cos 2\psi\sin 2\theta - \mu^2\eta_T \sin 2\psi\cos 2\theta\cos\varphi\Big\} \ , \tag{3.41}$$

$$f_{SH,P}(\hat{\mathbf{n}},\hat{\mathbf{p}};\hat{\mathbf{m}}) = \frac{\omega^2}{4\pi\rho\alpha^3\beta} AF\left(k_\beta\hat{\mathbf{n}} - k_\alpha\hat{\mathbf{m}}\right)\mu^2\eta_T\cos\psi\sin 2\theta\sin\varphi \ , \tag{3.42}$$

$$f_{SV,P}(\hat{\mathbf{n}},\hat{\mathbf{p}};\hat{\mathbf{m}}) = \frac{\omega^2}{4\pi\rho\alpha^3\beta} AF\left(k_\beta\hat{\mathbf{n}} - k_\alpha\hat{\mathbf{m}}\right) \times \Big\{(\lambda+\mu)\mu\eta_N \sin 2\psi + \mu^2\eta_N\sin 2\psi\cos 2\theta - \mu^2\eta_T\cos 2\psi\sin 2\theta\cos\varphi\Big\} \ , \tag{3.43}$$

$$f_{SH,SH}(\hat{\mathbf{n}},\hat{\mathbf{p}};\hat{\mathbf{m}},\hat{\mathbf{q}}) = \frac{\omega^2}{4\pi\rho\beta^4} AF\left(k_\beta(\hat{\mathbf{n}}-\hat{\mathbf{m}})\right)\mu^2\eta_T\cos\psi\cos\theta\cos\varphi \ , \tag{3.44}$$

$$f_{SH,SV}(\hat{\mathbf{n}},\hat{\mathbf{p}};\hat{\mathbf{m}},\hat{\mathbf{q}}) = \frac{\omega^2}{4\pi\rho\beta^4} AF\left(k_\beta(\hat{\mathbf{n}}-\hat{\mathbf{m}})\right)\left(-\mu^2\eta_T\right)\cos\psi\cos 2\theta\sin\varphi \ , \tag{3.45}$$

$$f_{SV,SH}(\hat{\mathbf{n}},\hat{\mathbf{p}};\hat{\mathbf{m}},\hat{\mathbf{q}}) = \frac{\omega^2}{4\pi\rho\beta^4} AF\left(k_\beta(\hat{\mathbf{n}}-\hat{\mathbf{m}})\right)\mu^2\eta_T\cos 2\psi\cos\theta\sin\varphi \ , \tag{3.46}$$

$$f_{SV,SV}(\hat{\mathbf{n}},\hat{\mathbf{p}};\hat{\mathbf{m}},\hat{\mathbf{q}}) = \frac{\omega^2}{4\pi\rho\beta^4} AF\left(k_\beta(\hat{\mathbf{n}}-\hat{\mathbf{m}})\right) \times \Big\{\mu^2\eta_N\sin 2\psi\sin 2\theta + \mu^2\eta_T\cos 2\psi\cos 2\theta\cos\varphi\Big\} \ . \tag{3.47}$$

Expressions (3.27) through (3.30) each contain a contribution $4(\eta_N - \eta_T)$. In the derivation of Equations (3.39) through (3.47), the contribution from the terms proportional to $4(\eta_N - \eta_T)$ is canceled by other terms containing η_T, which results in a considerable simplification of the resulting expressions. Note that any scattering coefficient with an SH-wave as an incoming or outgoing wave depends on μ and η_T, but not on λ and η_N, which reflects that SH-waves do not depend on the compressive response of the medium. As a result, only the shear properties of the fracture influence the scattering to and from SH-waves.

3.5 Laboratory Experiments

We carry out laboratory experiments in order to measure P- to P-scattering and test our theoretical model. We use ultrasonic frequencies in plastic samples. The samples are Poly(methyl methacrylate) (PMMA) cylinders with a diameter of 50.8 mm and a height of 150 mm (Figure 3.5). Elastic waves are generated with a 5 MHz disk-shaped piezoelectric transducer (PZT) with a diameter of 7.5 mm attached to the curved surface of the cylinder using phenyl salicylate as a glue. Because this glue has a melting point of 41.5°C, slight heating is enough to melt it and use it to attach the transducer to a curved surface. The PZT is driven by a 400 V pulse with maximum energy at its natural frequency.

We measure the elastic displacement with the laser interferometer described in Chapter 2. Since the sample material is transparent for green light, we apply a reflective tape to the surface to reflect light back to the laser receiver.

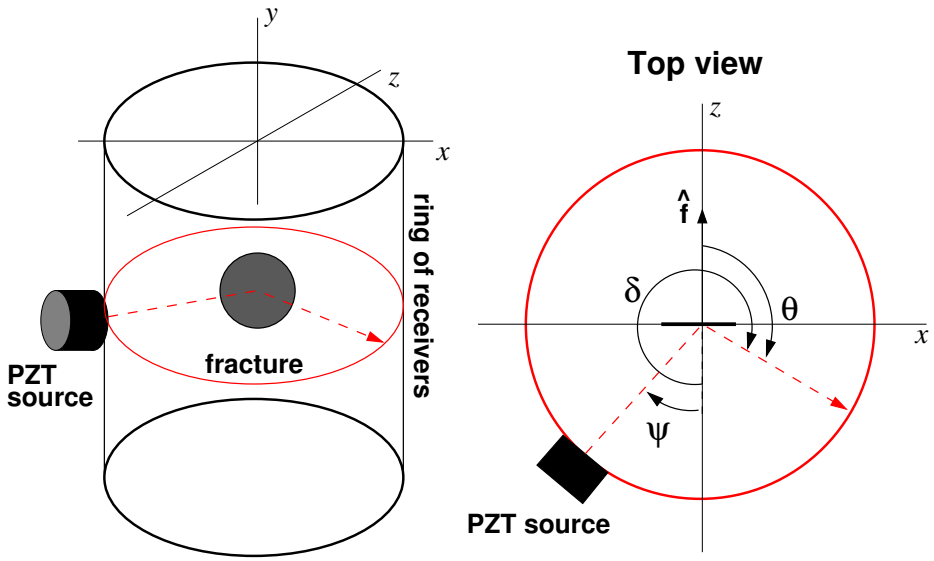

Figure 3.5: Geometry of the experimental setup with the angles as defined in Figure 3.3.

3.5.1 Measurements on a Blank Sample

We first carry an experiment out on a sample with no cracks, also called a blank cylinder. This measurement is used as a reference of the background field propagating in the absence of a scatterer. The sample is mounted on a computer-controlled rotational stage. We focus the laser receiver beam on the sample in a plane normal to the cylinder axis (taken as the y-axis). This plane also contains the PZT source, the source and receiver are thus located in the (x, z) plane. By computer-controlled rotation of the stage, we measure the elastic field in this plane every degree with respect to the center of the cylinder, except for a small range of angles blocked by the PZT source. The signal is digitized with 16-bit precision and a sampling rate of 100 MS/s (mega samples per second) and recorded on a computer acquisition board. For each receiver location, 256 waveforms are acquired and averaged after digitization.

Figure 3.6 shows the raw ultrasonic displacement field for all recorded azimuths.

The horizontal axis represents the angle δ between the source and the receiver directions, $\delta = \theta + 180^\circ$ (for θ defined in Figure 3.3; see also Figure 3.5). The main events on this scan are the direct P-wave displacement with a curved moveout and the Rayleigh wave traveling around the sample with a linear moveout. Some ringing of the source is present after the direct arrival and is strongest for δ angles close to 180°. The frequency content of these data ranges from 250 kHz to 1.2 MHz. In order to remove the high-amplitude Rayleigh wave arrival, we apply an f-k filter to the data. The resulting displacement field is presented in Figure 3.7. All measurements following these are performed in the (x, z) plane and f-k filtered.

From these data, we find the P- and S-wave velocities of the material to be respectively $\alpha = 2600$ m/s and $\beta = 1400$ m/s. For a PMMA density of $\rho = 1190$ kg/m^3, these values correspond to Lamé coefficients $\lambda = 3.4$ GPa and $\mu = 2.3$ GPa, respectively.

3.5.2 Fractured Sample

We create a single fracture in a different cylinder of PMMA by focusing a high power Q-switched Nd:YAG laser in the sample. The laser generates a short pulse ($\sim$ 20 ns) of infrared (IR) light that is absorbed by the sample material at the focal point and is converted into heat. The sudden thermal expansion generates stress and forms a fracture at the focal point location. Anisotropy in the elastic moduli, caused by the extrusion process, results in a fracture with an orientation parallel to the cylindrical axis. Zadler and Scales (2008) give a more extensive description of the fracture generation process. The laser-generated fracture, shown in Figure 3.8, has a roughly circular shape and a radius of approximately 7 mm. Figure 3.5 shows a diagram of

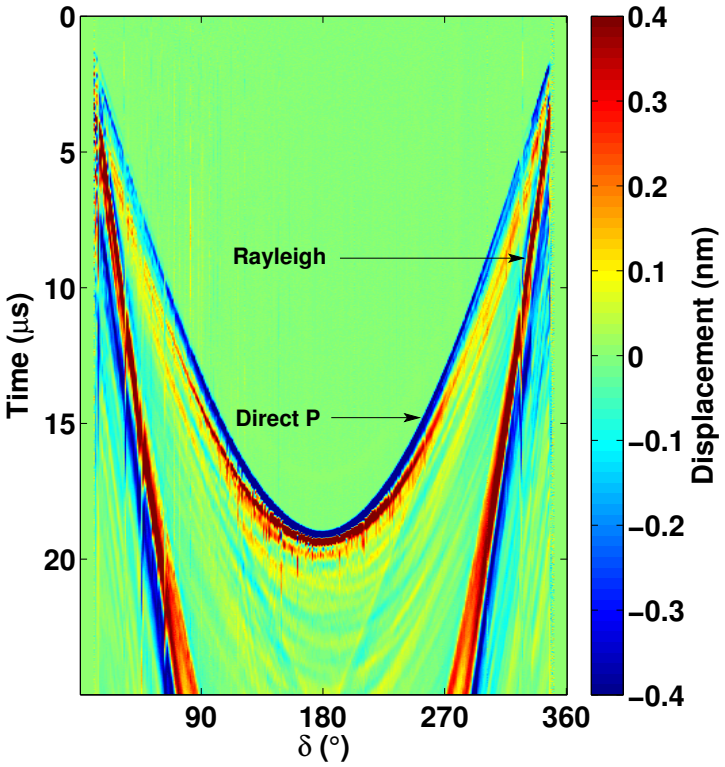

Figure 3.6: Displacement field for a homogeneous PMMA sample.

the fractured sample and the geometry of the experimental setup.

We show in Figure 3.9 the ultrasonic displacement after f-k filtering, measured with the PZT source at location S1 normal to the fracture plane (Figure 3.10). This source location corresponds to an angle $\psi = 0°$. In addition to the events present with the blank sample, Figure 3.9 shows a wave arriving at about 20 μs; this arrival corresponds to the P-P scattered field from the crack. The amplitude of this event is maximum for $\delta = 180°$ (forward scattering), and $\delta = 0°$ (backscattering), corresponding to the specular reflection (Figure 3.10). Note that this event is slightly asymmetric: for receiver angles $\delta < 180°$, the scattering arrival is earlier than 20 μs, whereas for angles $\delta > 180°$, the wave arrives slightly later than 20 μs. This is due to the fact that the fracture is not perfectly centered on the y-axis. For forward

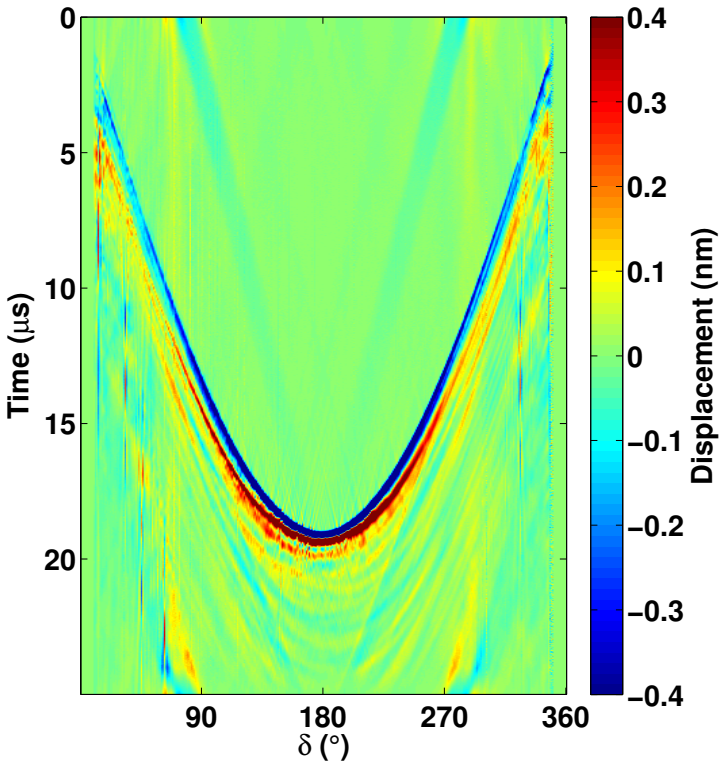

Figure 3.7: Displacement field for the homogeneous PMMA sample after f-k filtering of the Rayleigh wave, highlighting the direct P-wave arrival.

scattering, the scattered wave interferes with the direct wave (Figure 3.9), and the scattering amplitude cannot be measured accurately. The presence of the source transducer makes it difficult to measure the backscattered waves. For this reason, Figure 3.12 does not show the scattering amplitude for scattering angles near forward and backward scattering.

As we show in the next section, for this source position, the scattering amplitude is a function of η_N only. In an attempt to estimate η_T, we perform a last experiment with the PZT source at location S2, making an angle $\psi \approx 50°$ to the normal to the fracture plane, but still in the (x, z) plane (see Figure 3.9). The corresponding ultrasonic displacement field after f-k filtering is shown in Figure 3.11. Note that,

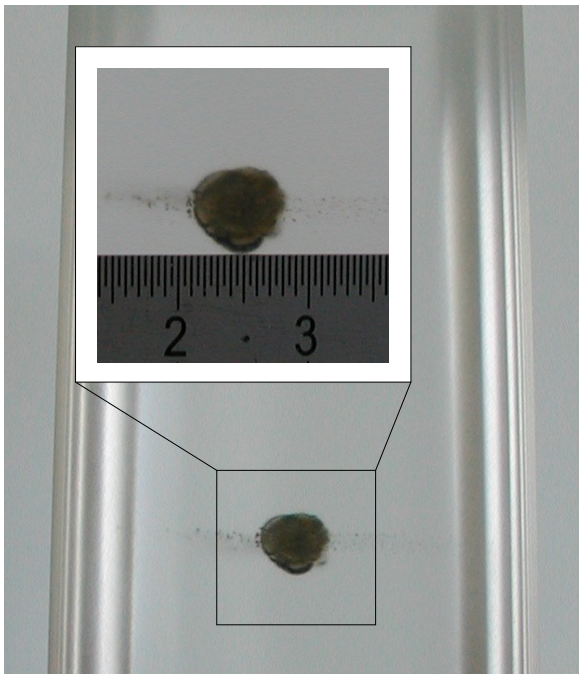

Figure 3.8: Photograph of the laboratory sample and zoom around the disk-shaped fracture, with ruler units in cm. The sample is longitudinally cut in half to display the fracture without optical deformation by the curvature of the sample. The diameter of the fracture is ~ 7 mm, and the diameter of the cylinder is 50.8 mm.

as shown in Figure 3.10, the scattering amplitude is largest for angles slightly larger than the specular reflection angle (corresponding to $\delta = 310°$).

3.5.3 Scattering Amplitudes

The theoretical scattering amplitudes for all combinations of waves are given by Expressions (3.39) through (3.47). Here, the source is at a fixed angle ψ to the normal to the fracture, hence $\hat{\mathbf{n}} = \sin\psi\ \hat{\mathbf{x}} + \cos\psi\ \hat{\mathbf{z}}$. The receiver is always in the (x, z) plane, therefore $\phi = 0°$ and $\hat{\mathbf{m}} = \sin\theta\ \hat{\mathbf{x}} + \cos\theta\ \hat{\mathbf{z}}$.

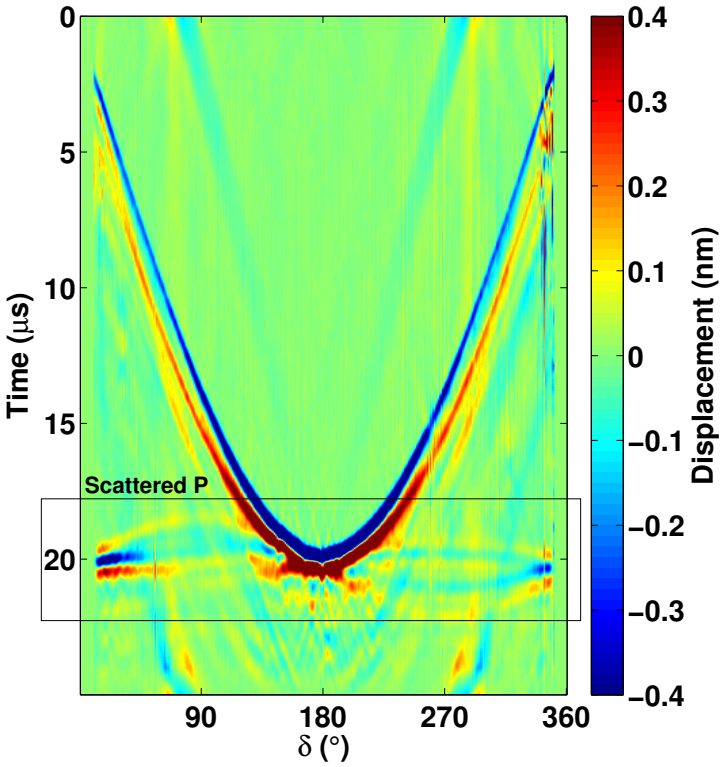

Figure 3.9: Displacement field for the fractured PMMA sample with the source at normal incidence (after f-k filtering).

For the case of both incoming and scattered P-wave, Equation (3.39) simplifies to

$$\begin{aligned} f_{P,P}(\hat{\mathbf{n}};\hat{\mathbf{m}}) =& \frac{\omega^2}{4\pi\rho\alpha^4} AF(k_\alpha(\hat{\mathbf{n}}-\hat{\mathbf{m}})) \\ & \times \Big[\eta_N \left((\lambda+\mu)^2 + (\cos 2\psi + \cos 2\theta)(\lambda+\mu)\mu \right. \\ & \left. +\mu^2(\cos 2\psi \cos 2\theta)\right) + \eta_T \mu^2 \left(\sin 2\psi \sin 2\theta\right)\Big] \,. \end{aligned} \tag{3.48}$$

Moreover, for a circular fracture, Equation (3.33) reduces for this geometry to

$$F\left(k_\alpha(\hat{\mathbf{n}}-\hat{\mathbf{m}})\right) \approx \frac{2\alpha}{a\omega(\sin\psi - \sin\theta)} J_1\left(\frac{\omega a}{\alpha}(\sin\psi - \sin\theta)\right) \,. \tag{3.49}$$

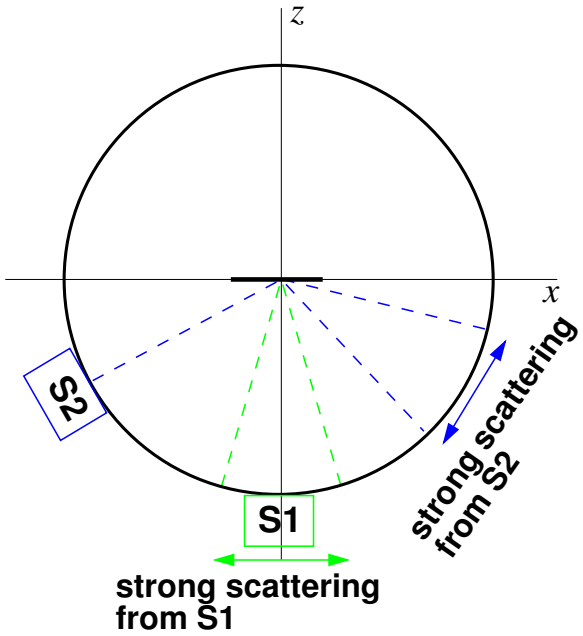

Figure 3.10: Schematic of the experimental setup with directions of maximum specular reflection for the two source positions.

For the experimental case, the scattering amplitude is thus given by

$$\begin{aligned} f_{P,P}(\psi,\theta) =& \frac{\omega a}{2\rho\alpha^3(\sin\psi-\sin\theta)} J_1\left(\frac{\omega a}{\alpha}(\sin\psi-\sin\theta)\right) \\ & \times \left[\eta_N\{(\lambda+\mu)^2+(\cos 2\psi+\cos 2\theta)(\lambda+\mu)\mu \right. \\ & \left. +\mu^2(\cos 2\psi\cos 2\theta)\} + \eta_T\mu^2\left(\sin 2\psi \sin 2\theta\right)\right] . \end{aligned} \tag{3.50}$$

Note that for a source at normal incidence, $\psi = 0°$ and therefore the term containing η_T vanishes. In this case, the scattering amplitude $f_{P,P}(\psi = 0°, \theta)$ depends only on the normal component η_N of the compliance tensor. On the other hand, for a non-normal incidence ψ, the scattering amplitude $f_{P,P}$ is a function of both η_N and η_T.

To compare the experimental results with the analytic expression, we measure

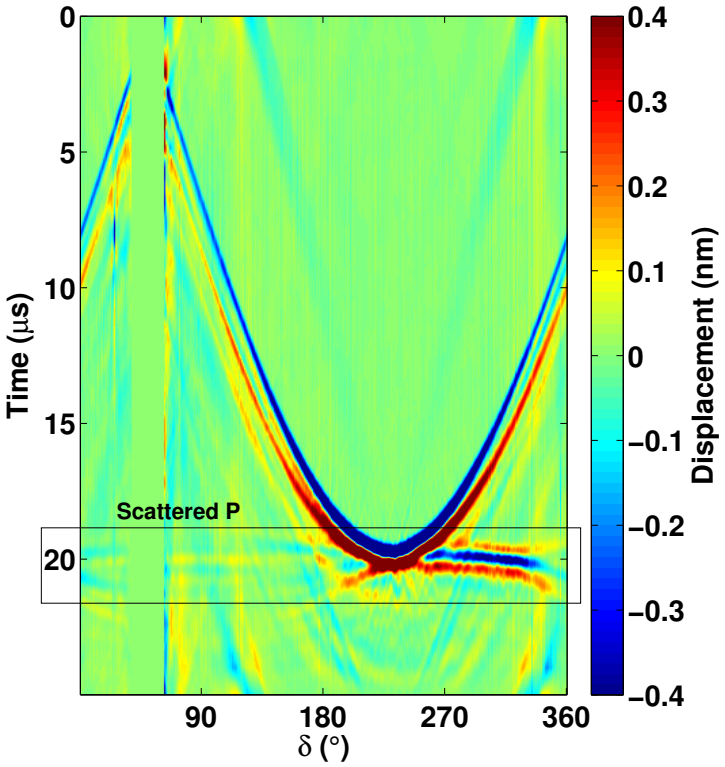

Figure 3.11: Displacement field for the fractured PMMA sample, where the source is at $\psi = 50°$ incidence (after f-k filtering).

the scattering amplitude. We apply a narrow band-pass filter centered around $f_0 =$ 1 MHz, corresponding to the dominant frequency of the scattered event. We then pick the amplitude of the scattered arrival at its maximum for a range of angles excluding traces close to the source, and for receivers facing the source, where the incident and scattered field overlap. We normalize the scattering amplitude by the amplitude of the direct P arrival at normal incidence, in order to compensate for differences in source coupling and strength between the two source locations. The experimental amplitudes for the valid range of angles are plotted in blue in Figures 3.12 and 3.13.

We compute the corresponding theoretical amplitudes for $f_0 = 1$ MHz, and use the Lamé coefficients computed from the measurement in the sample without fracture.

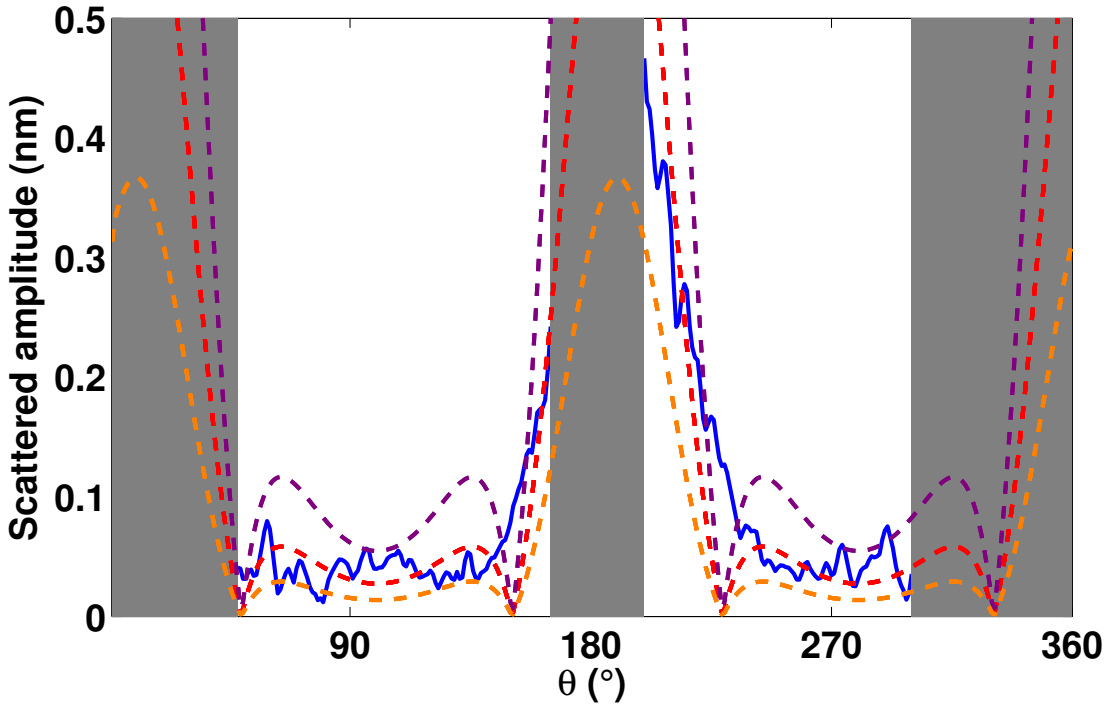

Figure 3.12: Scattering amplitude for the source at normal incidence in blue ($\psi = 0°$). The best theoretical fit corresponding to $\eta_N = 10^{-11}$ m/Pa is plotted in a thick, dashed red line. We also show the theoretical amplitudes corresponding to half (dotted orange) and twice (dotted purple) this value of η_N. The ranges of angles where the field cannot be measured are marked in gray.

We assume the created fracture behaves as a circular fracture with radius $a = 5$ mm, estimated visually. We first optimize the fit with the theoretical amplitude (displayed in red in the figures) for the normal incidence data since for this angle of incidence the scattering amplitude depends only on normal component of the compliance η_N, but not on η_T. The best fit is obtained for $\eta_N \approx 10^{-11}$ m/Pa, corresponding to the thick dashed red curve in Figure 3.12. We also display the computed scattering amplitude for $\eta_N = 2 \cdot 10^{-11}$ m/Pa (dotted purple line) and $\eta_N = 0.5 \cdot 10^{-11}$ m/Pa (dotted orange line) to show that the $\eta_N = 10^{-11}$ m/Pa value is a robust fit. Note that the fit with η_N only calibrates the overall amplitude of the scattering amplitude, but

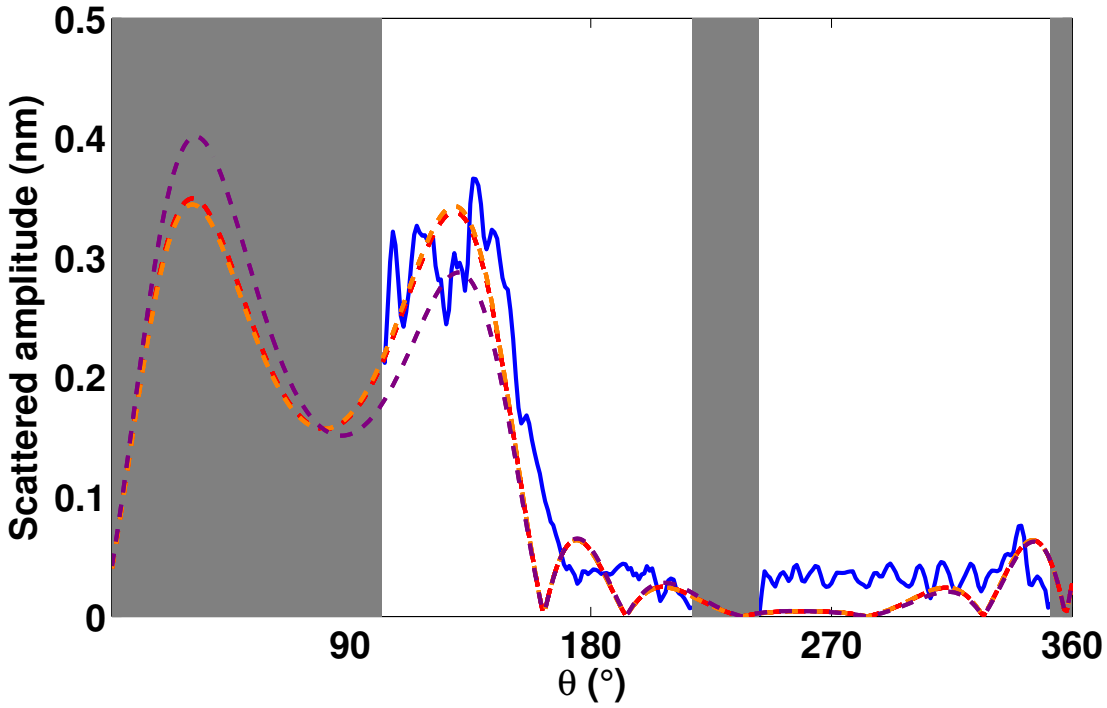

Figure 3.13: Scattering amplitude for the source at $\psi = 50°$ incidence in blue. The theoretical curve for $\eta_N = 10^{-11}$ m/Pa and $\eta_T = 10^{-12}$ m/Pa is plotted with a thick, dashed red line. We also show the theoretical amplitudes corresponding to one tenth (dotted orange) and ten times (dotted purple) this value of η_T. We see here that the value of η_T is not well constrained for this experimental configuration. The ranges of angles where the field cannot be measured are marked in gray.

that the dependence of the scattering amplitude on the scattering angle is completely determined by the theory.

We then use this value for η_N to optimize the fit of the second dataset by changing the shear compliance η_T. Figure 3.13 is a comparison between data and theoretical curves for $\eta_N = 10^{-11}$ m/Pa and three different values of the shear compliance: $\eta_T = 10^{-12}$ m/Pa (thick dashed red line) and $\eta_T = 10^{-11}$ m/Pa (dotted purple line) and $\eta_T = 10^{-13}$ m/Pa (dotted orange line). While according to Equation (3.50) the scattering amplitude depends on the shear compliance η_T, this dependence is

weak. The best fitting shear compliance $\eta_T = 10^{-12}$ m/Pa is an order of magnitude smaller than the estimated normal compliance, and the uncertainty in the estimate of the shear compliance ranges from 10^{-13} m/Pa to 10^{-11} m/Pa. These values of compliances are, however, in the same range as $\eta \sim 10^{-13} - 10^{-9}$ m/Pa found in the literature for the case of a single fracture in quartz monzonite (Pyrak-Nolte *et al.*, 1990b) and in various natural rocks (Worthington, 2007).

3.6 Conclusion

Because fractures play a key role in processes going from seismic activity to fluid flow, fracture characterization is a critical step in time-lapse monitoring of fluid flow in reservoirs. Based on a linear slip model, we derive the analytic expression of the scattered amplitude of a plane fracture of arbitrary size under the Born approximation. Of particular interest are the results for fractures of comparable size to the elastic wavelength. The theory provides scattering amplitudes for every combination of incident and scattered wave mode, which are expressed as a product of a Bessel function and trigonometric functions in the case of a circular fracture. Non-contacting ultrasonic data acquired on a plastic laboratory sample for P-wave to P-wave scattering from a circular fracture is in qualitative agreement with the theory, and the estimated compliance of the fracture agrees with the range of values reported in the literature. The theory presented here is not applicable to fluid-filled fractures, because the Born approximation used in Equation (3.10) and subsequent expressions break down when the fluid in the fracture causes the shear traction at the fracture to vanish.

CHAPTER 4:

SCATTERING AMPLITUDE OF A SINGLE FRACTURE UNDER LOAD

4.1 Introduction

Fully characterizing a fracture assuming linear slip behavior involves estimating both the normal and tangential components of the compliance. Moreover, in exploration geophysics, the ratio between normal and tangential compliance is used as a proxy for the presence of fluids in the fracture (Hudson *et al.*, 1997; Liu *et al.*, 2000; Lubbe *et al.*, 2008). Monitoring the stress dependence of fractures is also of high interest. In exploration, hydrocarbon (or possibly water) reservoirs see the local stresses change as a result of production. Time-lapse monitoring of stress through fractures properties could help assess reservoir conditions. Similarly, in volcanic environments, stresses are related to volcanic activity, and dikes, local fractures, as well as the volcanic conduit all respond to changes in stress (Gudmundsson, 2006). In seismology, Sawazaki and Snieder (2013) argue that the S-wave velocity recovery after earthquake-induced velocity changes can be explained by the closing of cracks in the shallow subsurface

caused by the earthquake dynamic strain.

In the previous chapter, we see that the estimation of the tangential compliance is ill-defined using only the P-P scattered event. Here, we use a different experimental setup and show that we can successfully measure the scattered field, including several distinct wave modes, without the limitations of Chapter 3. We therefore independently estimate the normal and tangential component of the compliance. This new setup allows us to apply an uniaxial stress to the sample, and we use it to measure the change in compliance of the fracture while increasing the static load.

4.2 Theoretical Background

We show in Chapter 3 that under the Born approximation and the assumption of incoming plane waves, the P-P scattered amplitude from a single fracture in the linear slip model is given in the frequency domain by Equation (3.27), where the angles ψ, φ and θ, as well as the incoming and outgoing unit vectors $\hat{\mathbf{n}}$ and $\hat{\mathbf{m}}$ are defined in Figure 3.3. Similarly, the SV-SV scattered amplitude under the same assumptions is given by Equation (3.30). For the case of a plane circular fracture, the form factor F is given by Equation (3.33). For the case of both incoming and outgoing waves in a common plane normal to the fracture, we finally get the simplified expression

$$\begin{aligned} f_{P,P}(\psi,\theta) =& \frac{\omega a}{2\rho\alpha^3(\sin\psi-\sin\theta)} J_1\left(\frac{\omega a}{\alpha}(\sin\psi-\sin\theta)\right) \\ & \times \left[\eta_N\{(\lambda+\mu)^2+(\cos 2\psi+\cos 2\theta)(\lambda+\mu)\mu \right. \\ & \left. +\mu^2(\cos 2\psi\cos 2\theta)\} +\eta_T\mu^2\left(\sin 2\psi\sin 2\theta\right)\right] , \end{aligned} \tag{4.1}$$

for the P to P scattered wave, where ω is the angular frequency, α the P-wave velocity and ρ the density of the material, λ and μ the Lamé parameters, a the radius of the fracture, and η_N and η_T the normal and tangential compliances, respectively. The angles ψ and θ are defined in Figure 3.3, and J_1 is the first order Bessel function. In a similar fashion, we get

$$f_{SV,SV}(\psi,\theta) = \frac{\omega a}{2\rho\beta^3(\sin\psi - \sin\theta)} J_1\left(\frac{\omega a}{\beta}(\sin\psi - \sin\theta)\right) \times \left[\eta_N \mu^2 \sin 2\psi \sin 2\theta + \eta_T \mu^2 \cos 2\psi \cos 2\theta \cos\varphi\right] \tag{4.2}$$

for the SV to SV scattered wave, with β the S-wave velocity. As shown previously, the η_N contribution of the P-P amplitude is maximum when θ or ψ are zeros, while the η_T contribution is null in that case. For the SV-SV amplitude, on the other hand, it is the opposite case where if θ or ψ is zero, the η_N contribution is null and the η_T contribution maximum. This highlights the fact that for most geometries, the shear wave is more sensitive to the tangential compliance than the primary wave. We will use these expressions of the scattering amplitudes to compare with our experimental results.

4.3 Experimental Setup

We use a similar sample to the one shown in Figure 3.8. Contrary to the experiment described in Chapter 3, we use here the pulsed Nd:YAG laser as a source, therefore we apply aluminum tape to the surface. The tape plays the role of the absorbing medium on the source side, and reflects light back for a wide range of angles to the laser receiver, allowing us to measure both out-of-plane and in-plane components.

The cylindrical PMMA sample is mounted on a rotational stage, whereas the locations of the non-contacting ultrasonic source and receiver are fixed in the laboratory frame of reference. The source-receiver angle δ (defined in Figure 4.1) is therefore constant, here $\delta = 20°$, and only the orientation of the fracture with respect to the frame of reference, characterized by the angle θ, changes. Moreover, the source and receiver are focused on the sample in an (x, y) plane normal to the cylinder axis (z-axis, Figure 4.1). While anisotropic, as mentioned above, the extruded PMMA is transversely isotropic, and its elastic properties are therefore invariant with respect to the defined angles of interest.

In order to put the sample under static stress, we furthermore load it by tightening a screw, pushing the top of the cylinder down. We use a bearing to accommodate the rotation of the loading screw, and insert a load gauge in between the bearing and the sample to measure the compressional stress. A picture of the laboratory setup is shown in Figure 4.2. We perform four measurements for different load settings; a first measurement with zero load (baseline), we next load it to a mid-load position corresponding to 5.5 Mpa, and then to full load position of 11.0 MPa, and finally a second measurement at zero load.

4.4 Results

4.4.1 Unloaded Sample

We first measure the scattered amplitudes for a sample under no static stress. The resulting out-of-plane and in-plane displacements are show in Figure 4.3. On the

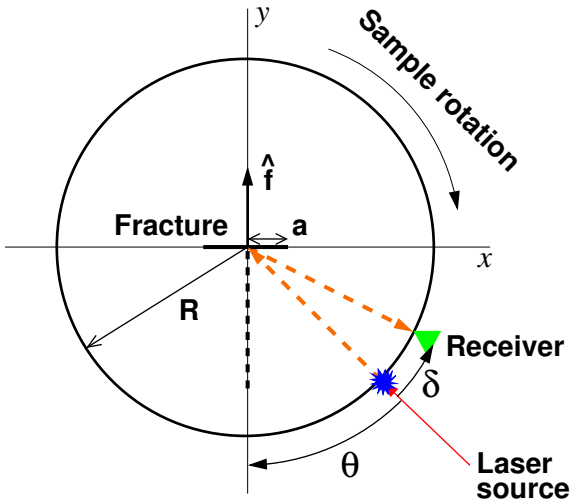

Figure 4.1: Schematic of the experimental setup. The source-receiver angle is fixed and the fracture rotates in respect to both source and receiver.

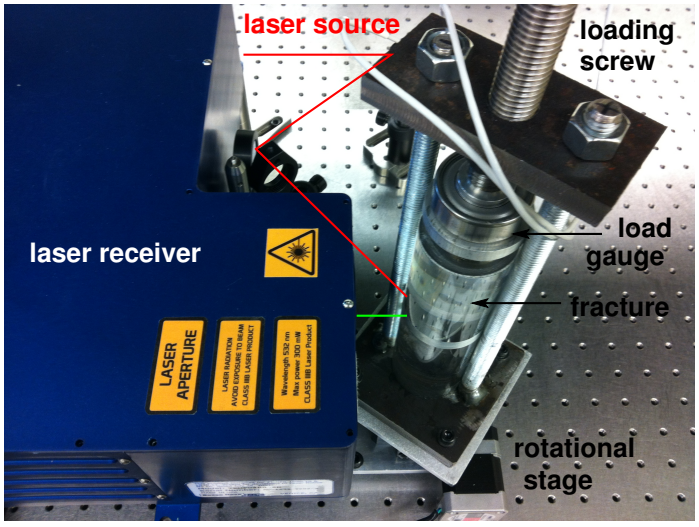

Figure 4.2: Photograph of the laboratory setup, including the source laser beam, laser receiver, load gauge above the sample and the load screw on top of the assembly.

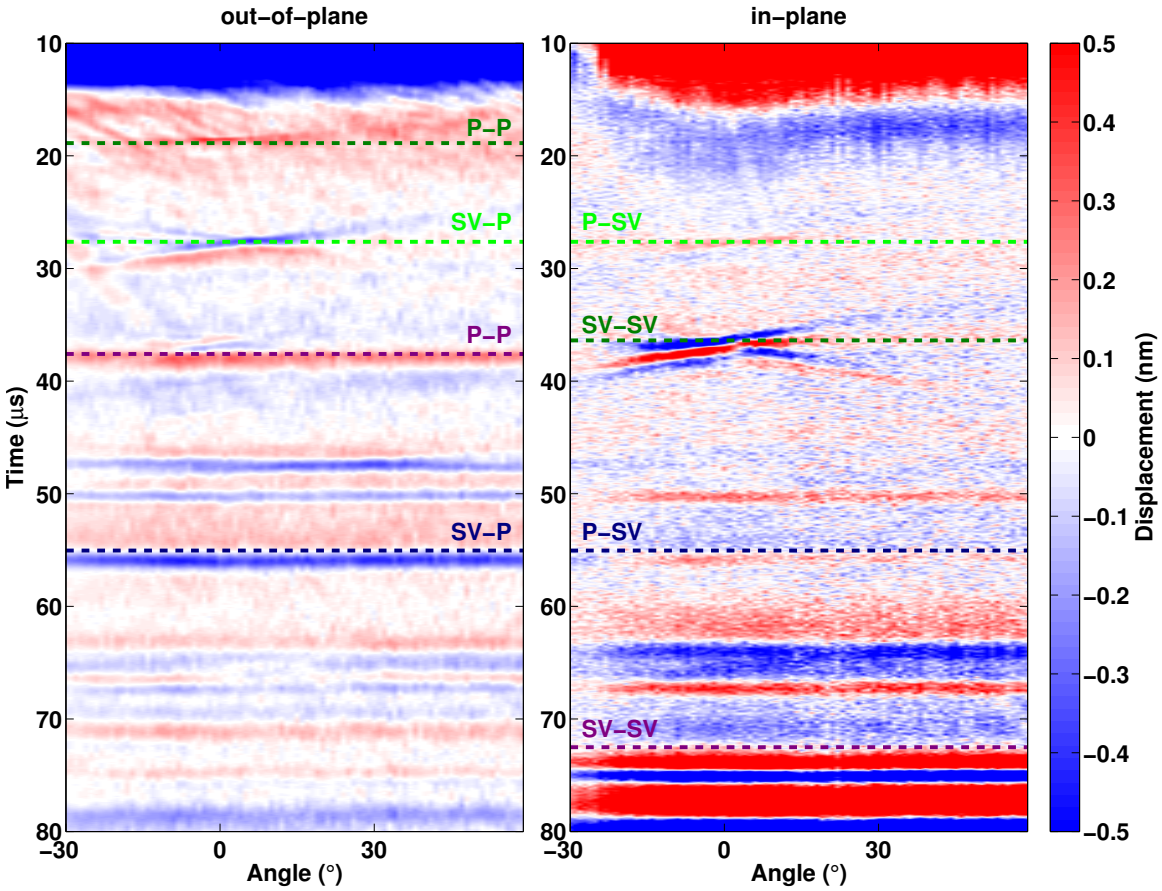

Figure 4.3: Displacement field for the unloaded sample. Left: out-of-plane channel, right: in-plane channel. Dark and light green dashed lines mark scattered arrivals, light green marks converted ones. Purple dashed lines mark reflections from the backwall of the sample, blue dashed lines mark mode conversions from the backwall.

out-of-plane channel, we first see the P-P scattered arrival around 18 μs, followed by the converted SV-P scattered event around 27 μs. We also see the P-P reflected from the back of the sample at 37 μs, and the converted SV-P reflection at 55 μs. The weaker unmarked events are side reflections and multiples. On the in-plane channel, we detect event with an outgoing SV phase, including the P-SV scattering conversion at 27 μs, followed by the SV-SV scattered wave at 36 μs, the P-SV reflection from the back of the sample at 55 μs, and finally the SV-SV reflection from the back of the sample at 73 μs. In order to extract the scattered amplitudes, we first band-pass the data around 1 MHz. We then pick the maximum amplitudes for two events of interest: the P-wave scattered from an incoming P-wave, that is detected on the out-of plane channel, and the SV-wave scattered from an incoming SV-wave, that is detected on the in-plane channel. Both the scattered P and scattered SV amplitudes are normalized by the amplitude of the wave with the same mode reflected from the backwall of the sample, and corrected for geometrical spreading, effectively reducing the scattered amplitude to a fraction of the incoming amplitude.

For this geometry, the amplitude of the P-P scattered is mostly sensitive to the normal component of the compliance η_N (see Equation (4.1)). Conversely, amplitude of the SV-SV scattered event is mostly sensitive to the tangential component η_T (see Equation (4.2)). We use a joint least square regression to obtain the parameters giving the best fit with the experimental data. We invert for the fracture radius a, the normal and tangential compliance, and the orientation of the fracture, given by the angle θ_0 relative to our best guess of $\theta = 0$. This last parameter does not vary significantly from one measurement to another. The measured amplitudes and corresponding fits are shown in Figure 4.4. The covariance matrix resulting from the inversion is shown

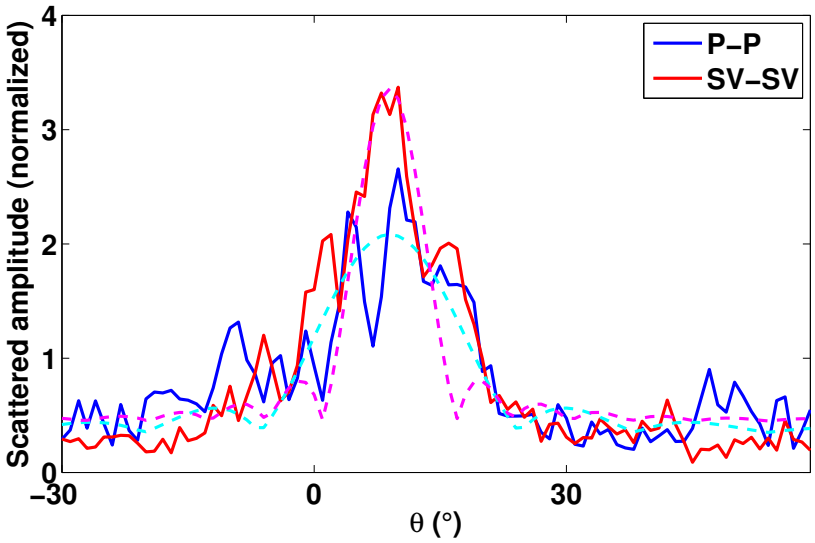

Figure 4.4: Measured (solid lines) and fitted amplitudes (dashed lines) for the P-P and SV-SV scattered events with an unloaded sample. From the fit, we get $a = 3.14 \pm 0.19$ mm, $\eta_N = 1.38 \pm 0.20 \cdot 10^{-11}$ m/Pa and $\eta_T = 2.69 \pm 0.34 \cdot 10^{-11}$ m/Pa.

in Figure 4.5.

4.4.2 Loading and Unloading of the Sample

The measured amplitudes and corresponding fits for the maximum load measurement are shown in Figure 4.6. The results are summarized in Figure 4.7. We see that when the load increases, the normal compliance η_N decreases. After the loading cycle, the estimated compliance is not exactly equal to the baseline value, but it is still higher than for the loaded case. The P-P and SV-SV backwall reflections stay constant in time for each loading stage, ruling out changes in the elastic properties of the homogeneous material.

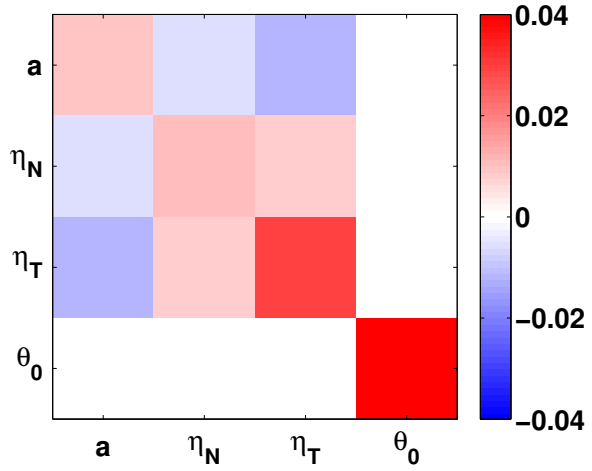

Figure 4.5: Covariance matrix resulting from the least square inversion of the unloaded scattering data. This matrix is computed with the parameters expressed in units so that their values are between one and ten, with a in mm, the compliances in 10^{-11} m/Pa, and θ_0 in degrees.

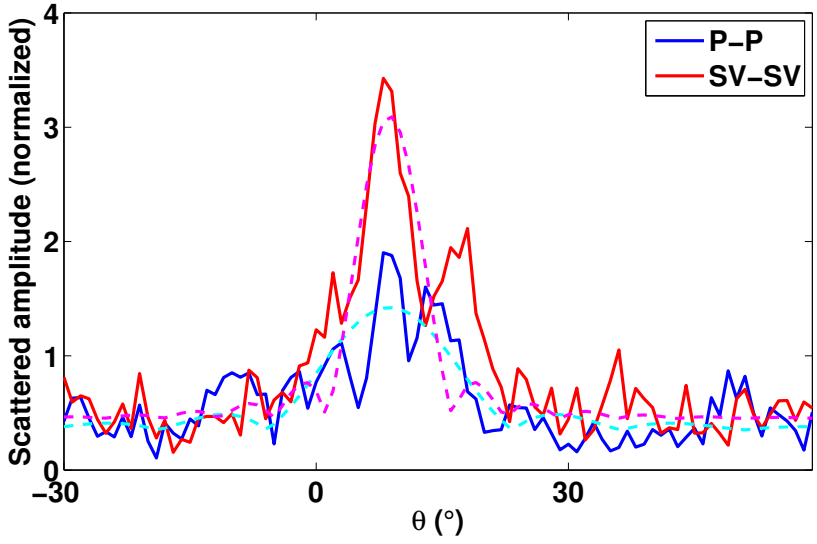

Figure 4.6: Measured (solid lines) and fitted amplitudes (dashed lines) for the P-P and SV-SV scattered events with a loaded sample at 11.0 MPa. From the fit we get $a = 3.32 \pm 0.22$ mm, $\eta_N = 0.77 \pm 0.14 \cdot 10^{-11}$ m/Pa and $\eta_T = 2.14 \pm 0.29 \cdot 10^{-11}$ m/Pa.

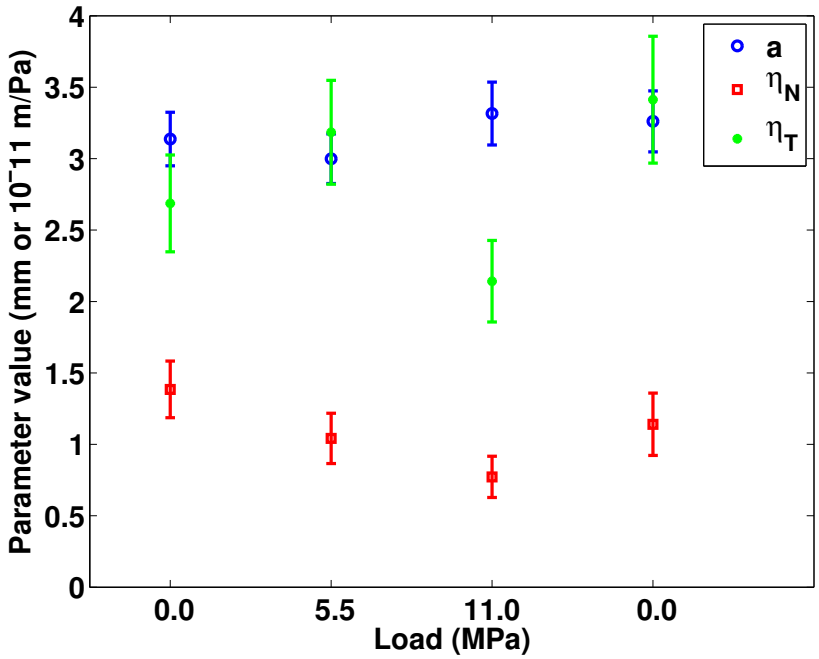

Figure 4.7: Estimates of the fracture radius a (in blue), and the normal and tangential compliances, η_N (in red) and η_T (in green), respectively, during the loading cycle. The errorbars correspond to the 95% confidence intervals.

4.5 Discussion

Again, the experimentally obtained scattering amplitudes are in good agreement with the theory described in the preceding chapter, and the estimated components of the compliance are on the same order of magnitude as the values obtained in Chapter 3. Moreover, by recording the SV-SV scattering event, we are able to estimate η_T with good confidence, and we observe $\eta_N/\eta_T \sim 0.5$, as noted in other studies (Worthington, 2007; Lubbe *et al.*, 2008). From the covariance matrix computed from the theoretical expressions, we note that both components of the compliance are negatively correlated to the fracture radius, and the estimated values represent a tradeoff between compliance and radius. The joint-inversion, however, ensures that the radius estimate is optimal for both P-P and SV-SV datasets.

As mentioned above, the reflection and scattering travel times stay constant with the increase in load, and show that the mechanical properties of the sample in the plane of the measurement are unchanged. We confirm it by looking at the amplitudes of the reflections from the back of the cylinder at zero load and maximum load. The resulting measurements, in Figure 4.8, do not show significant change between the two states of stress, for either the reflected P and SV waves. We, however, observe an increase in PP amplitude between 0 and 10°, corresponding to the forward scattered wave. The high variability of the measured reflected SS amplitude precludes us from making a similar observation for this mode.

The static uniaxial load results show that the estimated radius is nearly constant over the cycle of four measurements. This is in agreement with the assumption that the effective area (area of the fracture where a discontinuity is present in the material) of the fracture should not change for such stresses, as they are too weak to modify

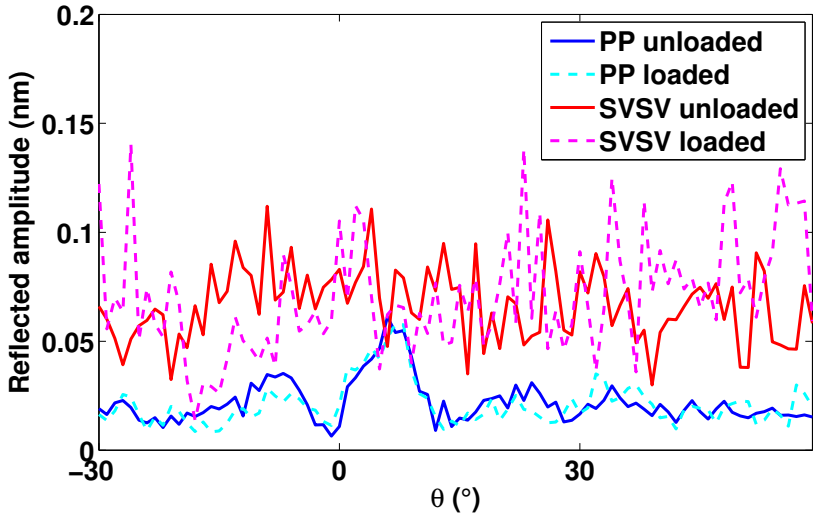

Figure 4.8: Amplitudes of the sample backwall reflection at zero and maximum stress (11.0 MPa). While there is no significant change introduced by the uniaxial stress, we observe a maximum in the reflected PP amplitude at angles between 0 and 10°, corresponding to the forward-scattering direction.

the structure of the fracture. We also observe a decrease in normal compliance as the stress increases, and the final value of the normal compliance, for a null static stress, is still lower than the initial η_T estimate. This effect could be due to a permanent plastic change of the fracture cause by the uniaxial stress. Most published laboratory studies of fractures involve uniaxial stresses normal to the fracture, and lead to a decrease in compliance with increasing load (Pyrak-Nolte *et al.*, 1990b), which can be explained by the fracture becoming stiffer as the stress helps "closing" it, and therefore increases the contact area of the fracture.

Here the stress axis is such that we would expect an opening of the fracture instead, leading to an increase in compliance. For bigger openings, however, the stiffness of round pores is greater than of fracture type shaped pores (Brie *et al.*, 1985; Saleh and Castagna, 2004); a schematic description is shown in Figure 4.9. By applying a load along a direction parallel to the fracture plane, the shape of the fracture changes

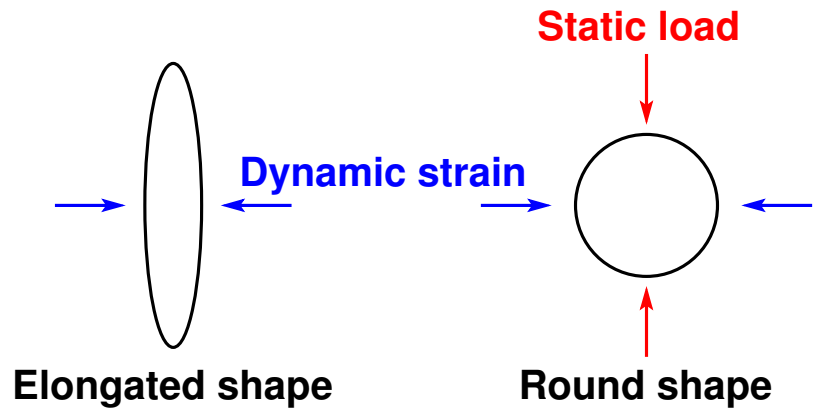

Figure 4.9: Schematic of pore shape responses. Left, an elongated pore is compliant to dynamic strains normal to the direction of elongation (blue arrows). This is analog to an unloaded fracture. Right, after applying a static load (represented by red arrows), the pore shape becomes round and stiff to the dynamic stain (blue arrows); this is analog to the loaded fracture.

from the ideal representation of a planar crack to a more rounded three-dimensional shape. Although this effect is small for the static load considered here, we nevertheless interpret the observed change in compliance as the result of a change in fracture shape from planar to more round-like.

Finally, it is hard to interpret the tangential compliance estimates. For these values, we are limited to relying only on the in-plane channel, which is susceptible to a bias on top of the variance (see Chapter 2). It is hence harder to see significant variations in the tangential component, and the errorbars shown in Figure 4.7 do not encompass the unknown bias. Therefore, we cannot conclude about the change in tangential compliance during the load of the fracture.

These results show that by combining measurements of two components of the displacement field, we are able to estimate the size as well as the normal and tangential compliance of the fracture, paving the way for measurements under confining pressure.

CHAPTER 5:

LASER EXCITATION OF A FRACTURE SOURCE FOR ELASTIC WAVES

5.1 Introduction

Being able to remotely sense the properties of fractures with elastic waves is of great importance in seismology (e.g., Nakahara *et al.*, 2011) and non-destructive testing (e.g., Larose *et al.*, 2010). For example, in geothermal and hydrocarbon reservoirs, it is very common to use hydraulic fracturing methods to attempt to increase the native permeability of the rocks above what is present in any naturally occurring fractures. The microseismic events associated with the fracturing process typically radiate seismic energy, which is recorded in nearby wells or at the surface. Much is left to be understood about the nature of such fractures and their relationship to elastic waves, but the scaling issues involved make numerical modeling a challenge. On the other hand, laboratory studies of fractures or faults are used to investigate their mechanical properties, such as stiffness (Pyrak-Nolte and Nolte, 1992), fracture slip-rate, stress drop, or rupture propagation (Ben-David *et al.*, 2010). Most microscopic

fractures under laboratory investigation are either on the surface of samples, or the result of new or growing fractures from an applied stress to induce fracture stick-slip creep (Thompson *et al.*, 2009; Gross *et al.*, 1993). Other laboratory studies focus on macroscopic fractures occurring naturally in rock samples (Pyrak-Nolte *et al.*, 1990b). In Chapter 3, we use non-contacting techniques to probe a fracture inside a clear sample to recover the fracture compliance. A high-powered laser excites the surface of the sample creating ultrasonic waves. These waves scatter from the fracture and are recorded at the surface of the sample with a laser interferometer (Scruby and Drain, 1990). Here, instead of only exciting the ultrasonic waves at the sample surface, we focus a IR laser beam at the fracture location, turning it into an ultrasonic source. This technique makes it possible to measure the fracture response as a function of source energy, stress on the sample, or the laser beam size and location. By scanning the fracture with a focused IR laser beam, it may be possible to measure spatial variations in the fracture properties and delineate barriers and asperities (Scholz, 1990), which are concepts of great importance in earthquake dynamics for example. A localized excitation, along the fracture, could also be used to excite interface waves traveling along the fracture (Roy and Pyrak-Nolte, 1997; Gu *et al.*, 1996) to probe for properties such as fault gouge or the fluids filling the fracture. Here, we illustrate the use of direct excitation of a fracture to investigate the elastic effective size of the fracture by means of tip diffractions. To date, these are most commonly studied on surface cracks (Masserey and Mazza, 2005).

5.2 Experiment

We consider the same PMMA sample containing a single disk-shaped fracture described in Section 3.5.2

Elastic waves are excited at the surface of the sample by using the high-power Q-switched Nd:YAG laser with a partially focused beam. Typically, the laser is focused on the outside of the sample — but as we explore here — the laser can also be focused inside the sample. In this case, the planar fracture has a visible contrast with the rest of the sample, seen as a darker region in Figure 3.8. The Nd:YAG pulsed laser generates energy at a wavelength of 1064 nm, in the near IR. Therefore, we assume that the optical contrast due to the fracture is also present at the IR wavelength, leading to energy absorption and thermoelastic expansion at the fracture location.

We measure elastic displacement with the laser interferometer. The location of the non-contacting ultrasonic source and receiver are fixed in the laboratory frame of reference, but the PMMA sample is mounted on a rotational stage. The source-receiver angle δ (defined in Figure 5.1) is therefore constant, here $\delta = 20°$, and only the orientation of the fracture with respect to the frame of reference, characterized by the angle θ, changes. Moreover, the source and receiver are focused on the sample in an (x, y) plane normal to the cylinder axis (z-axis, Figure 5.1). While anisotropic, as mentioned above, the extruded PMMA is transversely isotropic, and its elastic properties are therefore invariant with respect to the defined angles of interest.

By computer-controlled rotation of the stage, we measure the elastic field in the (x, y)-plane for values of θ in increments of 1 degree. The signal is digitized with 16-bit precision and a sampling rate of 100 MS/s (mega samples per second) and recorded on a computer acquisition board. For each receiver location, 256 waveforms

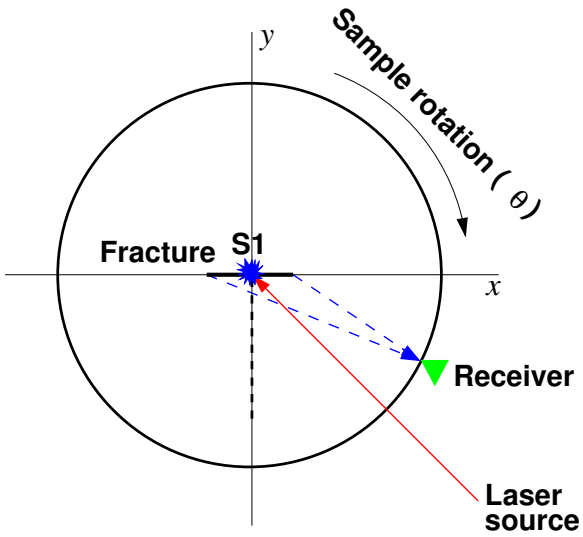

Figure 5.1: Top view of the experimental setup for direct fracture excitation. The laser source beam (red) excites elastic waves (blue) at S1.

are acquired and averaged after digitization.

Figure 5.2 shows the ultrasonic displacement field for the source S1 at the fracture for all recorded azimuths, after applying a 1-5 MHz band-pass filter. As defined in Figure 5.1, the horizontal axis represents the angle θ between the normal to the fracture and the source direction. Electromagnetic interferences are generated by the high-power source laser when the light pulse is emitted, and leads to noise being recorded for short arrival times (0 – 3 μs, highlighted in Figure 5.1). The arrival at approximately 10 μs denoted fP corresponds to the wavefield excited at the fracture. The fPP wave is excited at the fracture and reflects off the backside of the sample.

Next, we apply reflective tape where the source laser beam hits the sample surface at S2, increasing the IR light absorption at the surface and lowering the amount of energy reaching the fracture (Figure 5.3). We repeat with this configuration the acquisition procedure used in the first experiment (Figure 5.4). The PfP wave is

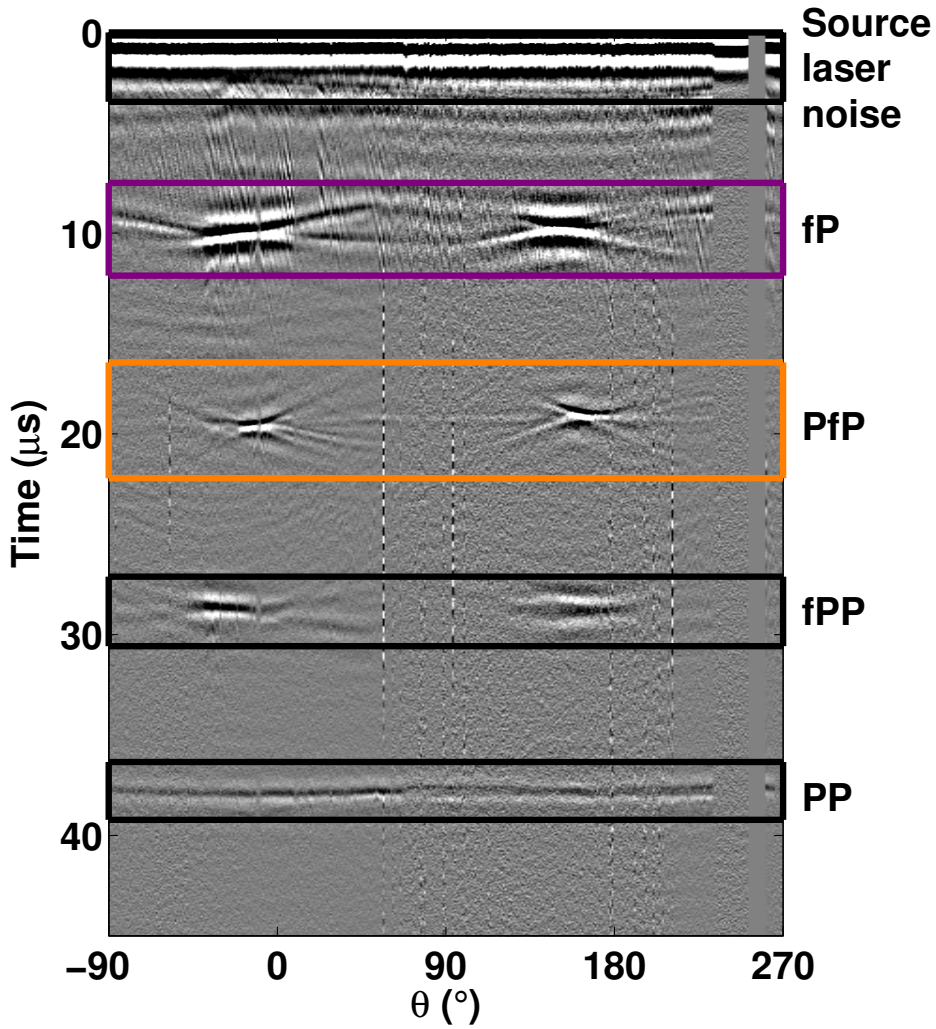

Figure 5.2: Displacement field generated by excitation of the fracture. fP is the P-wave generated at S1 and traveling directly to the receiver. PfP is the P-wave generated at S2 and scattered by the fracture before reaching the receiver. fPP is the P-wave generated at S1, traveling away from the receiver before bouncing back to the sample surface. Finally, PP is the P-wave generated at S2, that travels across the sample and bounces back to the receiver.

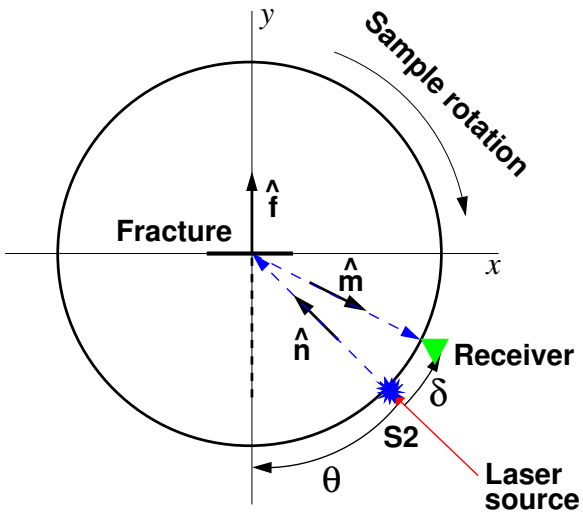

Figure 5.3: Top view of the experimental setup for elastic-wave excitation at the sample surface. The laser source beam (red) excites elastic waves (blue) at S2.

generated at the surface of the sample, and then scattered by the fracture, while PP is scattered from the backside of the sample. PfP and PP phases are stronger than fP and fPP in Figure 5.2, confirming that more of the thermoelastic expansion takes place at the surface of the cylinder.

5.2.1 Fracture Tip Travel Times

The waves fP and PfP in Figures 5.2 and 5.4 show a distinct lenticular pattern. For source angles $\theta = -10°$ and 170°, the PfP phase is a specular reflection, and the amplitude is a maximum. For intermediate angles, the scattered amplitude decreases (see in Chapter 3). Note splitting of the wave at intermediate angles into wavelets arriving before and after the specular reflection (see Figure 5.5). These waves have the travel time and phase of waves diffracted by the crack tips. In particular, for $\theta = 70°$, the receiver is in the plane of the fracture, and therefore the travel time difference between the tips of the fracture that are the closest and the farthest to the receiver

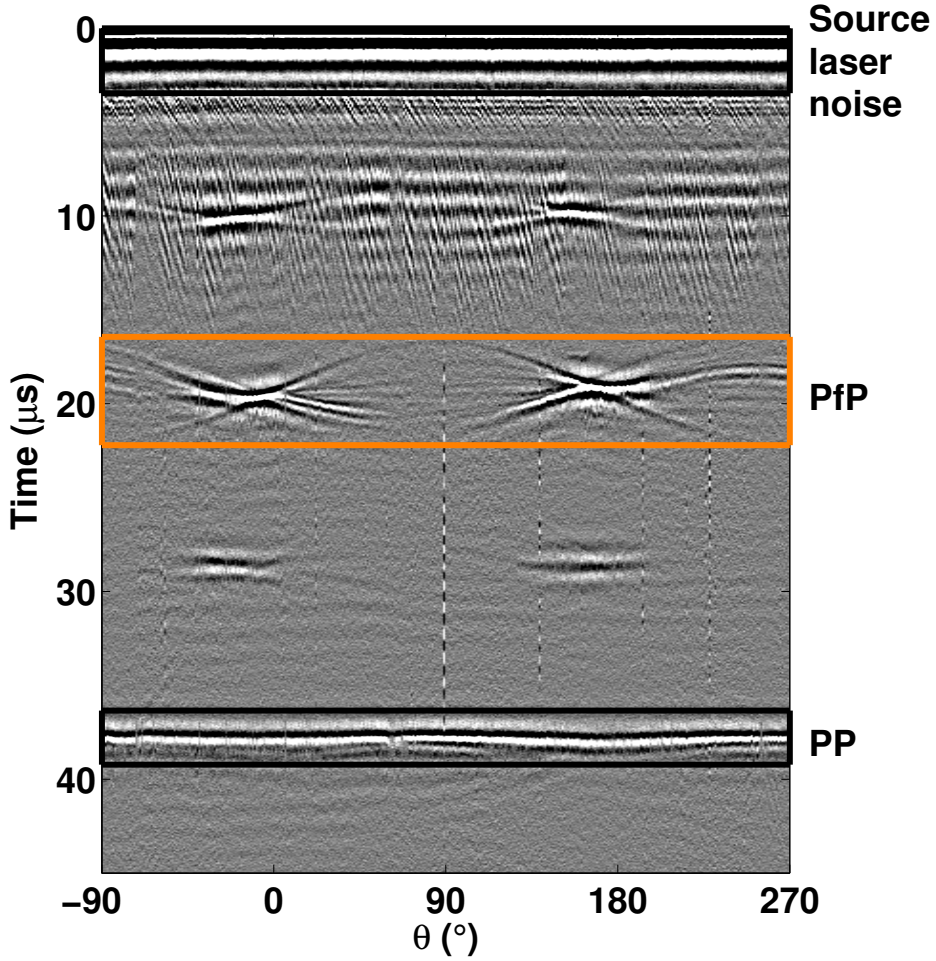

Figure 5.4: Displacement field generated by excitation at the sample interface. Signal for $t < 3$ μs corresponds to noise generated by the laser source, and to the direct P-wave traveling directly from the source S1 to the receiver. Other arrivals are defined in Figure 5.2.

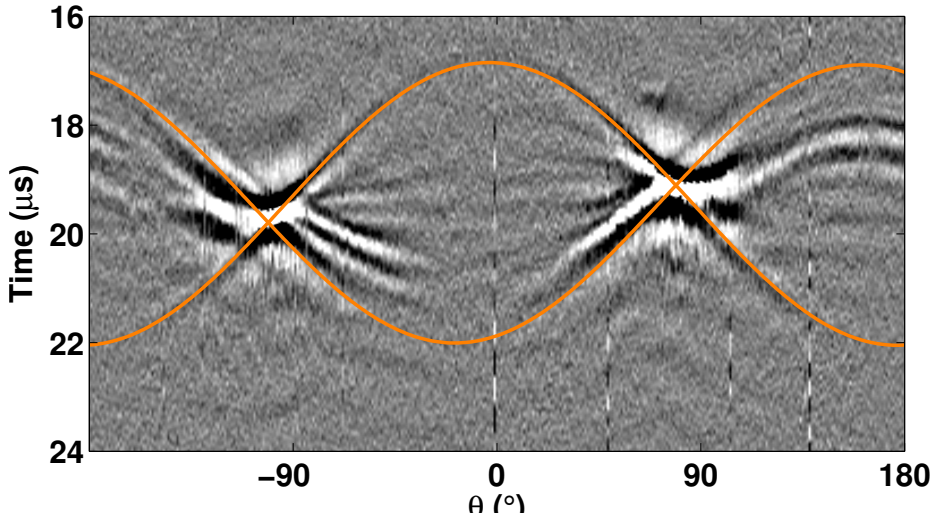

Figure 5.5: Detailed view of the scattered (PfP) arrival. The orange curves represent the tip arrival times computed from Equation (5.1).

is largest (Figure 5.3).

Equation (3.27) shows that the P to P scattered amplitude for a planar fracture in a linear-slip model under the Born approximation can be written in the frequency domain as a product of a scaling factor, a factor depending on the mechanical properties of the fracture and the propagation medium, and a *form factor* that depends on the fracture shape and the wave number change from the fracture scattering. Only this last factor carries time information. We show in Appendix D that the corresponding traveltimes are

$$t_{\text{tip-sc}} = \frac{R}{\alpha}\left(2 \pm \frac{a}{R}\left(\sin\theta(1+\cos\delta) + \sin\delta\cos\theta\right)\right), \tag{5.1}$$

where a is the radius of the fracture and R the radius of the cylinder. The P-wave velocity is $\alpha = 2600$ m/s (Section 3.5.1). Figure 5.5 shows the PfP arrival overlain by the computed traveltimes from equation (5.1) with a fracture radius $a_{PfP} = 3.3$ mm.

For the arrival time of the fP wave that is excited at the fracture, we consider the geometry of rays originating from the fracture tips and traveling directly to the receiver. The raypaths are shown in Figure 5.1. Using this geometry, the travel time can be expressed as

$$t_{\text{tip-direct}} = \frac{\sqrt{a^2 \pm 2aR\sin(\theta) + R^2}}{\alpha} \,. \tag{5.2}$$

Due to the fact that the size of the fracture is small compared to the radius of the sample, this travel time is to leading order in a/R given by

$$t_{\text{tip-direct}} = \frac{R}{\alpha}\left(1 \pm \frac{a}{R}\sin(\theta)\right) \,. \tag{5.3}$$

Figure 5.6 shows the fracture-source displacement field overlain with the tip arrival time (in purple) computed from Equation (5.3). Just as in Figure 5.5, the theoretical time for a radius $a_{fP} = 3.3$ mm agrees well with the arrival time of the fP wave, and the observed size in Figure 3.8. The good agreement with the visually estimated radius confirms that the whole visually fractured area is mechanically discontinuous and capable of being excited by elastic waves.

5.3 Conclusions

Laser-based ultrasonic techniques can not only excite and detect elastic waves at the surface, but can also be used to directly excite heterogeneities (such as fractures) inside an optically transparent sample. This result opens up possibilities for diagnosing the mechanical properties of fractures by directly exciting them. Here, we estimate the effective elastic size of the excited fracture. By scanning the fracture

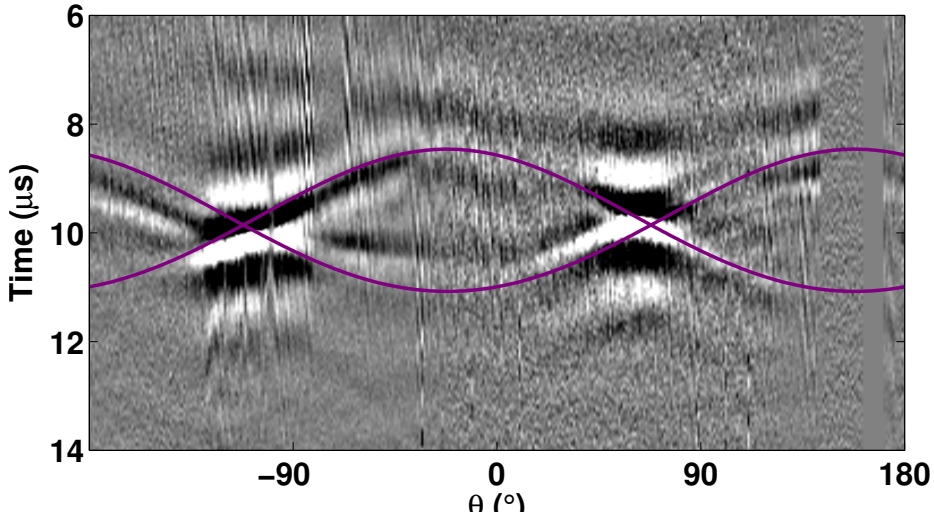

Figure 5.6: Detailed view of the direct fracture excitation arrival. The purple curves represent the tip arrival times computed from Equation (5.3).

with a focused IR laser beam, it may be possible to measure spatial variations in the fracture properties and delineate barriers and asperities. These concepts are of great importance in earthquake dynamics, although hard to investigate in the field or numerically.

CHAPTER 6:

MEASUREMENTS OF THE ELASTIC PROPERTIES OF SHALES

6.1 Introduction

Shale formations comprise about seventy-five percent of the clastic fill of sedimentary basins and recent interest to exploit shales as potential reservoirs requires better understanding of their elastic behavior. Accurate estimation of elastic moduli has implications in understanding response and distribution of stress in shales (Dewhurst and Siggins, 2006; Holt *et al.*, 2011), as well as in hydraulic fracturing (Suarez-Rivera *et al.*, 2006). Shales can be represented as thin isotropic layers with a symmetry axis, also called transversely isotropic (TI), or hexagonal. Wave propagation in a transversely isotropic medium can be described with five elastic constants, and the ratios among these parameters quantify the rock anisotropy (Thomsen, 1986; Tsvankin, 2001).

Shale anisotropy in the laboratory has been widely studied with transducer ultrasonic systems at variable saturation and pressure conditions (Jones and Wang,

1981; Vernik and Nur, 1992; Johnston and Christensen, 1995; Hornby, 1998; Wang, 2002; Dewhurst and Siggins, 2006; Bayuk *et al.*, 2009; Sondergeld and Rai, 2011; Holt *et al.*, 2011). Three directions of wave propagation on core samples are the minimum requirement to estimate the five elastic constants of the stiffness tensor. For measurements with transducers, this is achieved by cutting three samples at 0°, 45° and 90° from the shale layers (Vernik and Nur, 1992; Hornby, 1998; Sondergeld and Rai, 2011) or by using one core plug with transducers attached at these three angles (Wang, 2002; Dewhurst and Siggins, 2006). Frequency dependence of the elastic constants has recently been the topic of stress-strain and ultrasonic laboratory experiments. Results are mixed, probably due to sample heterogeneity and saturation conditions. Duranti *et al.* (2005) conclude that the measured West Africa shales display frequency dispersion while Sarker and Batzle (2010) observe no changes in the elastic stiffness constants with frequency in an organic rich shale. The measurements described above have been mostly performed on saturated shales, whereas the measurements presented in this dissertation are currently only recorded on dry samples. Recently, Miller *et al.* (2012) show that for fast anisotropic formations, sonic logs measure the group velocity, and that measurements at different angles from a deviated well can be used to directly estimate all the elastic constants.

We propose a new methodology to measure the directional dependence of elastic velocity and amplitude on one horizontal shale core plug by acquiring dense and high-quality velocity data. The method, described in details in Chapter 2, uses a non-contacting laser source and receiver, which has the following advantages over transducer acquisition: 1) transducer coupling and ringing do not affect the data, 2) sampling is as dense as one trace every 0.25 mm, 3) acquisition is fast and auto-

mated, and 4) for the case of transversely isotropic media, the fast and slow velocity directions do not need to be known or assumed before acquisition. The current system measures the sample properties at room conditions; however, our laboratory is developing capabilities to measure rock samples under pressure.

Guilbaud and Audoin (1999) and Ogi *et al.* (2003) use laser ultrasonics to measure the elastic properties of anisotropic materials. Scales and Malcolm (2003) observe directional P-wave velocity anisotropy in a fractured granite sample by using laser sources and receivers. Velocity (Dewangan *et al.*, 2006), as well as amplitude (Zhu *et al.*, 2007), or polarization (Lebedev *et al.*, 2011) measurements in phenolic materials are studied using transducer sources and a laser receiver. In this chapter we outline the procedure and summarize observations of source-receiver laser ultrasonic measurements on horizontally cored shales, and compare these data to transducer ultrasonic measurements.

Figure 6.1 is a photograph of the two horizontal shale samples measured in this study. Sample MSH is an oil shale from an outcrop in Montana with a density of 1.70 g/cm^3 and shale SHC has a density of 2.40 g/cm^3. Because the samples are measured dry and at room conditions, the anisotropy estimates do not represent that of shales *in situ*. However, the purpose of this chapter is to describe a new methodology to estimate elastic constants, which can be implemented on preserved samples and under reservoir conditions in future work.

6.2 Theoretical Description

A medium is called vertical transversely isotropic (VTI) if the symmetry axis is defined in the vertical direction for a specific coordinate system (x_3 in our study). The stiffness

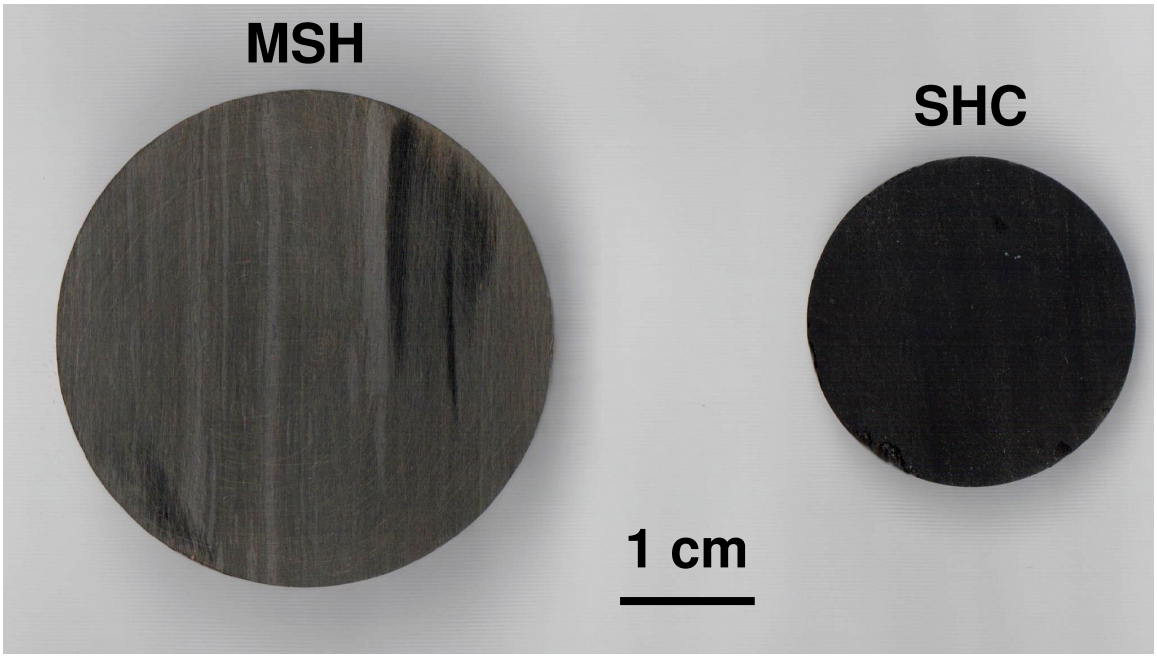

Figure 6.1: Top view of the two shale samples measured in this study. Lamination is clearly observed in sample MSH, while sample SHC has visible cracks, but these are not captured in this photograph.

tensor for a VTI media has five independent elastic constants, namely $c_{11}, c_{13}, c_{33}, c_{55}$, and c_{66} (Rudzki, 1911; Helbig, 1958; Tsvankin, 2001). The velocity of a P- (V_{P0}) and two polarized S- (V_{SV0} and V_{SH0}) waves propagating along the symmetry axis (x_3, θ=0°, see Figure 6.2) are defined as

$$V_{P0} = \sqrt{\frac{c_{33}}{\rho}},\ V_{SV0} = \sqrt{\frac{c_{55}}{\rho}},\ V_{SH0} = \sqrt{\frac{c_{55}}{\rho}}, \tag{6.1}$$

where ρ is the rock's bulk density. For propagation parallel to the symmetry plane ($\theta = 90°$), the velocities correspond to

$$V_{P90} = \sqrt{\frac{c_{11}}{\rho}},\ V_{SV90} = \sqrt{\frac{c_{55}}{\rho}},\ V_{SH90} = \sqrt{\frac{c_{66}}{\rho}}. \tag{6.2}$$

The P-wave anisotropy of a VTI medium can be described with Thomsen's parameters ϵ and δ (Thomsen, 1986). ϵ quantifies the velocity difference for wave propagation along and perpendicular to the symmetry axis, while δ controls the P-wave propagation for angles near the symmetry axis:

$$\epsilon = \frac{c_{11} - c_{33}}{2c_{33}}, \tag{6.3}$$

$$\delta = \frac{2(c_{13} + c_{55})^2 - (c_{33} - c_{55})(c_{11} + c_{33} - 2c_{55})}{2c_{33}^2}. \tag{6.4}$$

These expressions are general and δ has not been simplified for the weak anisotropy case ($\delta \ll 1$). The P-wave phase velocity as a function of phase angle (θ) and elastic constants for a VTI medium is (Tsvankin, 2001)

$$V_P(\theta) = \sqrt{\frac{(c_{11} + c_{55})\sin^2\theta + (c_{33} + c_{55})\cos^2\theta + \mathrm{D}}{2\rho}}\,, \tag{6.5}$$

where

$$\begin{aligned} \mathrm{D} = \Big\{ &\left[(c_{11} - c_{55})\sin^2\theta - (c_{33} - c_{55})\cos^2\theta\right]^2 \\ &+ 4(c_{13} + c_{55})^2 \sin^2\theta \cos^2\theta \Big\}^{1/2}\,, \end{aligned} \tag{6.6}$$

and the constant c_{13} is physically bound by the following relation (Tsvankin, 2001):

$$c_{13,\max} = \sqrt{c_{33}c_{11}}\,. \tag{6.7}$$

Although most transducer experiments measure the phase velocity (Dellinger and Vernik, 1994; Hornby, 1998), our experimental setup, described in the following sec-

tion, measures the propagation along a straight line between source and receiver. This results in a measurement of the group velocity as a function of group angle. Tsvankin (2001) shows that the P-wave group velocity U_P is given as a function of phase angle θ by

$$U_P(\theta) = V_P(\theta)\sqrt{1 + \left(\frac{1}{V_P(\theta)}\frac{dV_P}{d\theta}\right)^2}, \tag{6.8}$$

and the group angle ψ is given by

$$\tan\psi = \tan\theta\left(1 + \frac{\frac{1}{V_P(\theta)}\frac{dV_P}{d\theta}}{\sin\theta\cos\theta\left(1 - \frac{\tan\theta}{V_P(\theta)}\frac{dV_P}{d\theta}\right)}\right). \tag{6.9}$$

Equations 6.8 and 6.9 highlight that for $\theta = 0°$ and $\theta = 90°$ (the "slow" and "fast" directions, respectively), we have $\psi = \theta$ and $U_P = V_P$. Thus, of the five independent elastic constants, c_{13} is the only parameter sensitive to whether we measure phase or group velocity. We estimate c_{13} from Equations 6.5 and 6.6, but because we measure group angles and velocities we use Equations 6.8 and 6.9 to compare the measured group velocity data to predicted phase velocity.

6.3 Laboratory Setup

In this chapter, we use the partially focused laser source beam on the shale samples and get a circular source with a diameter of approximately 6 mm. We measure the resulting waves with the two-component laser ultrasonic receiver described in Chapter 2. Since our shale samples are dark materials, reflective tape on the sample enhances the amount of light reflected back to the laser receiver. We use aluminum tape that is 90 μm thick. The effect of the tape on the measurement is described in

Appendix B. We will consider here that it introduces a phase delay of ~ 0.02 μs for the out-of-plane channel, and of ~ 0.16 μs for the in-plane channel, both accounted for during data processing.

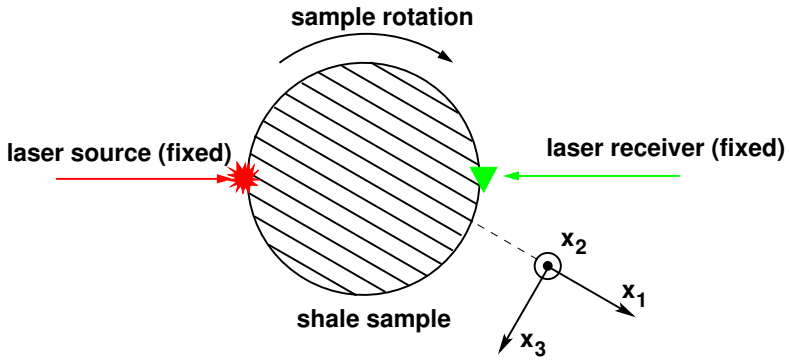

Figure 6.2: Top view schematic of the experimental setup, with the directions used here. x_3 is the axis of rotational symmetry, and the plane (x_1, x_2) is parallel to the beddings. The phase and group angles (θ and ψ, respectively) are zero when the source and receiver are aligned with x_3.

As sketched in Figure 6.2, the shale plug is mounted in the center of a rotational stage and the source and receiver beams are aligned on antipodes for a transmission experiment. The lasers and the sample are positioned on an optical bench with vibration isolation, and a photograph of the experimental setup is presented in Figure 6.3. The rotational stage is computer-controlled and the output of the interferometer is acquired at 10 MegaSamples/s and digitized at 16-bit precision. By using a PCI digital oscilloscope card, we are able to fully automate the data acquisition. In order to increase the signal-to-noise ratio, 200 measurements are summed for each angular position. The acquisition time is approximately 4 hours per sample. This experimental setup provides a direct measurement of the propagation along the ray direction, and hence leads to an estimation of the group velocity as a function of the group angle, as shown in Figure 1.1 of Tsvankin (2001).

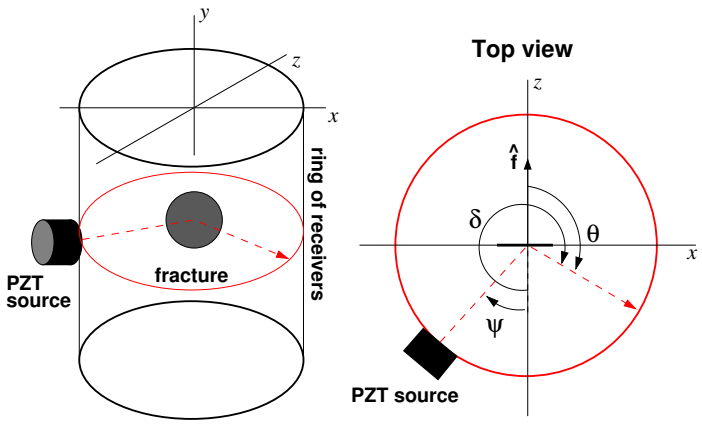

Figure 6.3: Photograph of the experimental setup from the top. The source laser beam arrives from the upper left corner of the picture and reflects off a mirror pointing towards the sample, while the laser receiver is at the bottom of the photo.

6.4 Results

Wavefields as a function of group angle are presented in Figure 6.4 and 6.5 for sample MSH and SHC, respectively. The amplitudes represent absolute particle motion and data are filtered between 50 kHz and 5 MHz. The dominant frequency of the measured waves is 500 kHz in the fast direction, and approximately 250 kHz in the slow direction. The observed events correspond to the direct P-wave followed by surface waves and scattered P- and S-waves. It is clear from Figures 6.4 and 6.5 that both samples have significant P-wave velocity anisotropy, and based on the acquisition geometry, there is data symmetry every 180°. The data also show a significant decrease in amplitude in the direction perpendicular to the layering compared to the direction parallel to the layering. Next, we analyze these travel time and amplitude variations.

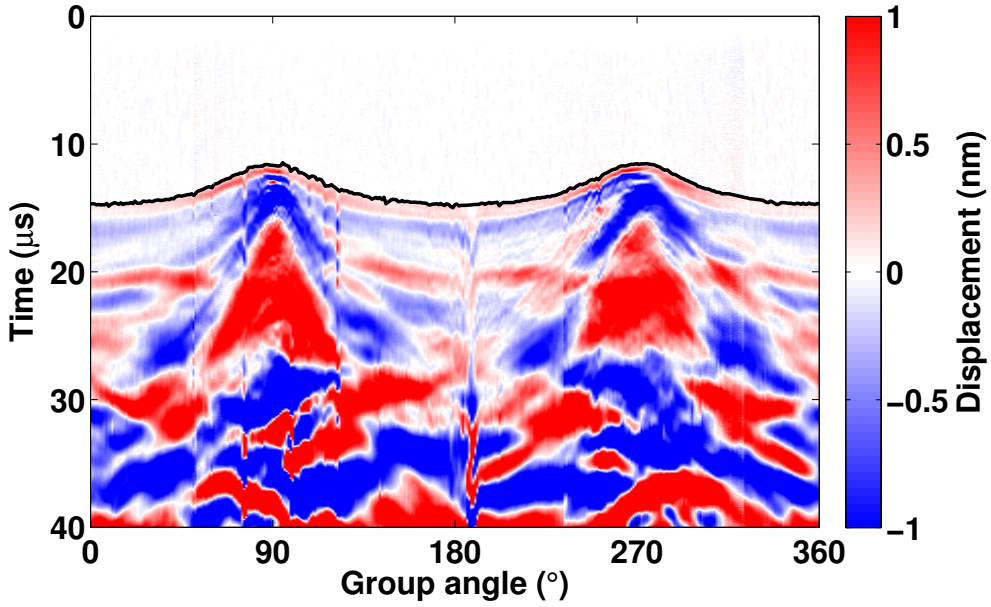

Figure 6.4: Laser ultrasonic waveforms for the MSH sample after normalization and band-pass filtering between 50 kHz and 5 MHz. The black line marks our first break picks. It is already apparent in this figure that the central frequency of the first arrival increases from the slow to the fast direction (group angle going from 0° to 90°), while the attenuation simultaneously decreases.

6.4.1 Travel Time Analysis

Direct P-wave arrivals are automatically picked when the signal exceeds more than 1% of the maximum direct wave amplitude. Dividing travel time picks by the distance traveled, we estimate the velocities plotted in Figures 6.6 and 6.7. Because of the dense spatial sampling, the slow ($\theta = \psi = 0°$) and fast ($\theta = \psi = 90°$) directions can be accurately estimated to provide good estimates of c_{11} and c_{33}.

Once the slow direction is defined, we measure the in-plane (horizontal) component of the wavefield at that location on the sample with the laser light that is reflected off-axis (see Chapter 2).

The horizontal component of the waveform is used to estimate the shear wave

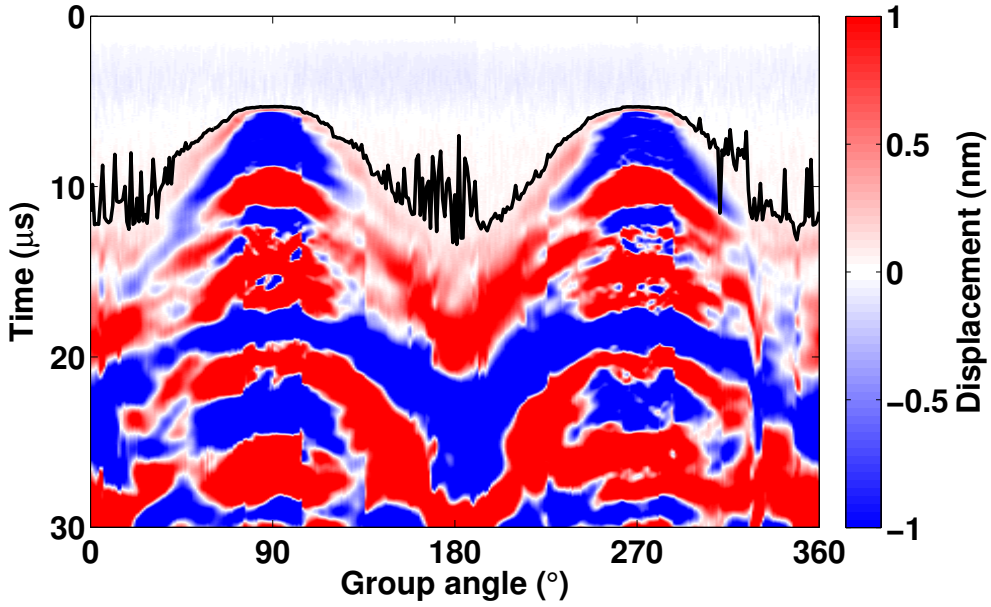

Figure 6.5: Laser ultrasonic waveforms for the SHC sample after normalization and band-pass filtering between 50 kHz and 5 MHz. The black line marks our first break picks. The attenuation is high enough along x_3 (corresponding to a zero group angle) that picking the first break becomes difficult. For this sample, variations in attenuation and frequency content as a function of angle are even more obvious than for sample MSH.

velocity along the axis of symmetry, V_{SV0}, from which we estimate c_{55} with Equation 6.1. As described in Appendix A, the measurement of the in-plane component is very sensitive to the focal position of the laser receiver. For this reason, we perform a careful measurement of both components in the slow direction ($\theta = 0$). The measured waveforms on sample MSH are shown in Figure 6.8.

After the relatively straightforward estimation of c_{11}, c_{33}, and c_{55}, we invert for c_{13} by performing a least squares fit to our measured group velocity data with the theoretical group velocity for a VTI medium using Equations 6.8 and 6.9. To obtain realistic values for c_{13}, we bound our inversion to the theoretical maximum value for c_{13} obtained with Equation 6.7. This procedure is successfully applied to sample

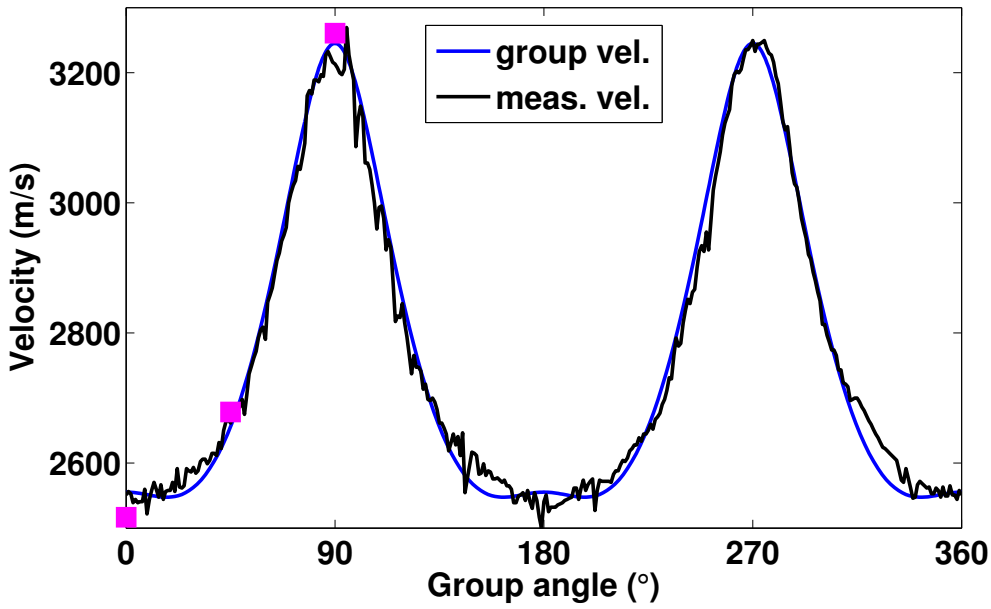

Figure 6.6: Measured laser ultrasonic P-wave velocity for MSH shale (black line). The blue line represents the best group velocity fit to the data for a c_{13}=3.8 GPa. Squares are data acquired with transducers at three angles.

MSH, giving the parameters shown in Table 6.1. However, the strong attenuation at $\psi = 0$ is preventing us from estimating c_{55} for sample SHC. Because we were unable to estimate c_{55} with laser data on this sample, we perform a joined least square fit to estimate both c_{13} and c_{55}. Although the density seems to play a role in the fit of Equation 6.5, it is not the case for velocity data, as measured velocities are converted to c_{ij}'s and then back into velocity, resulting in density cancellation.

We estimate the uncertainties of the measured physical quantities, and propagate them to the elastic constants. The uncertainties for the constants, estimated by a least square fit (c_{13} for both samples, and c_{55} for SHC), correspond to the 95% confidence interval. Figures 6.6 and 6.7 show the experimental and theoretical velocities, where the black line is the data and the blue line is the best group velocity fit to the data for samples MSH and SHC. We observe that the velocity prediction is good for almost

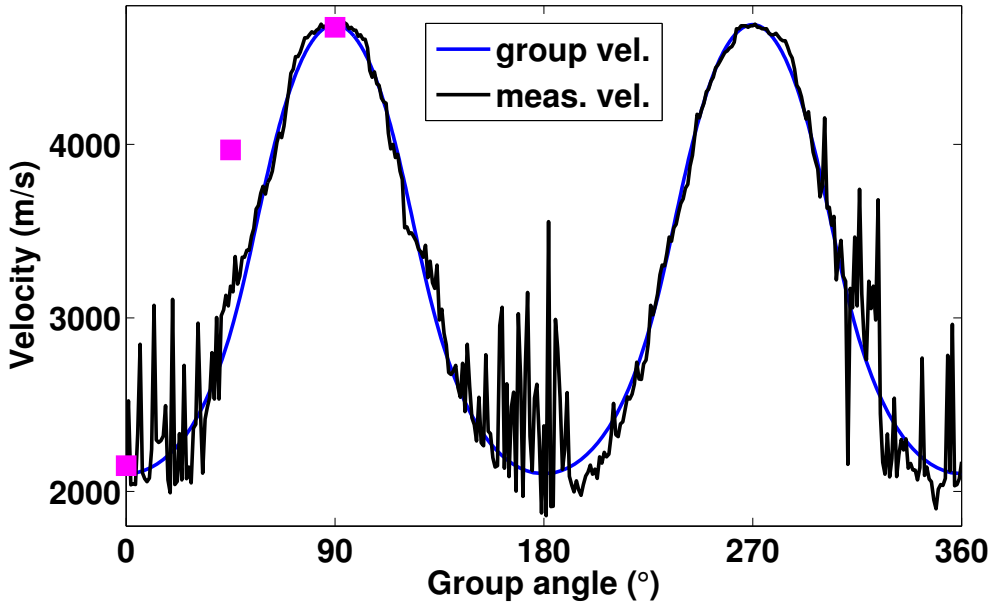

Figure 6.7: Measured laser ultrasonic P-wave velocity for MSH shale (black line). The blue line represents the best group velocity fit to the data for a c_{13}=11.6 GPa and c_{55}=10.6 GPa. Squares are data acquired with transducers at three angles.

every direction. Estimates of the elastic constants for samples MSH and SHC are summarized in Table 6.1.

Table 6.1: Summary of the elastic coefficients (in GPa) and corresponding anisotropy Thomsen parameters (unitless) for each sample.

Sample	c_{11}	c_{33}	$c_{13,\text{est}}$	$c_{13,\text{max}}$
MSH	18.0 ± 0.4	11.1 ± 0.2	4.1 ± 1.9	14.2
SHC	52.8 ± 2.6	8.8 ± 0.3	9.5 ± 0.6	21.5
Sample	c_{55}	ϵ	δ	
MSH	3.3 ± 0.1	0.31 ± 0.02	-0.27 ± 0.22	
SHC	11.7 ± 0.5	2.52 ± 0.19	6.62 ± 0.43	

We also use transducers to measure the compressional wavefield at 0°, 45°, and 90°. The resulting velocities are marked with squares in Figures 6.6 and 6.7. For

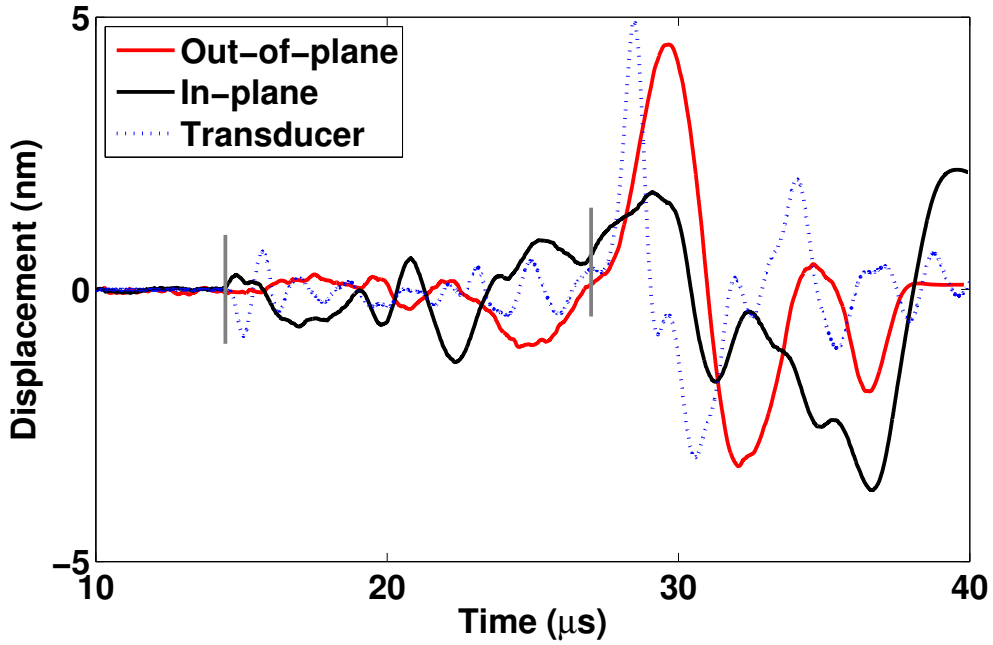

Figure 6.8: Displacement field along the vertical (black) and horizontal (red) components, measured in the slow direction ($\theta = \psi = 0$). The gray bars mark the first break pick for each component. The dotted blue line is a signal acquired using shear transducers as source and receiver for comparison.

sample SHC, the transducer velocity for $\psi = 45°$ is 34% higher than the measured laser ultrasonic velocity.

6.4.2 Amplitude Analysis

We also study the wave attenuation anisotropy for sample MSH. Figure 6.9 is the extracted absolute amplitude of the trough following the first break, after band-pass filtering the processed laser ultrasonic data between 150 and 250 kHz. In order to get a qualitative analysis of the attenuation anisotropy, we compare the experimental amplitudes to the theoretical expression derived in the weak-attenuation anisotropy

approximation from Equation 36 in Zhu and Tsvankin (2006):

$$\mathcal{A}_P = \mathcal{A}_{P0}\left(1 + \delta_Q \sin^2\theta\cos^2\theta + \epsilon_Q \sin^4\theta\right) , \tag{6.10}$$

where $\mathcal{A}_{P0}$ is the normalized attenuation coefficient giving the decay per wavelength in the symmetry direction (x_3). δ_Q and ϵ_Q are unitless Thomsen-style parameters defined in Zhu and Tsvankin (2006), where "the parameter δ_Q is responsible for the attenuation coefficient in near-vertical directions, while ϵ_Q controls $\mathcal{A}$ near the horizontal plane." The attenuation coefficient is often estimated using the spectral-ratio method, requiring an additional amplitude measurement under identical conditions for a non-attenuative reference sample (Zhu *et al.*, 2007). However, our laser source characteristics depend on the sample properties, and would be different on a reference sample. This prevents us from estimating $\mathcal{A}_{P0}$ and thus from getting absolute attenuation. Instead, we fit the relative attenuation coefficient to estimate the Thomsen-style attenuation parameters. We use the symmetry of the setup to average the two halves of the amplitude data, and then apply a smoothing running average normalized by the group wavenumber. Finally, a least-square inversion gives the best-fitting parameters with a 95% confidence interval as $\delta_Q = -0.80 \pm 0.23$ and $\epsilon_Q = -0.67 \pm 0.03$, and the resulting fit is shown in Figure 6.10.

6.5 Discussion

Laser-based ultrasonic measurements of shale (or other VTI media) anisotropy offer several advantages over a traditional setup with contacting transducers. The technique presented requires only one core drilled perpendicular to the axis of symmetry

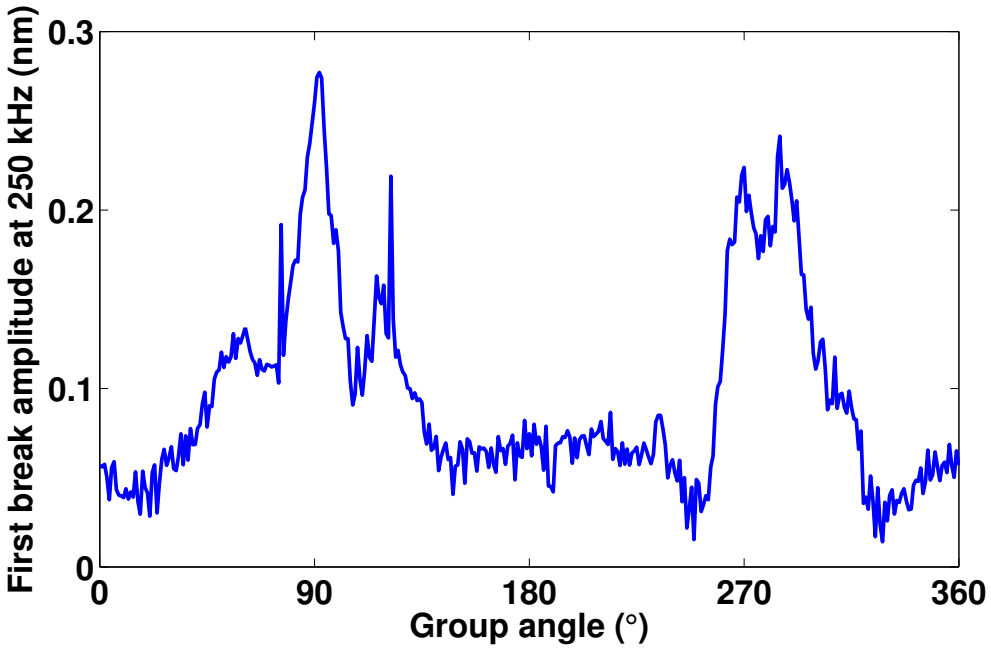

Figure 6.9: Amplitude of the first break for sample MSH. The lack of smoothness of the curve is due to the uncertainties in the amplitude measurement. We can, however, distinctly identify two high-amplitude peaks for group angles around 90° and 270°, corresponding to the x_1 direction and consistent with velocity anisotropy observations.

of the shale. Moreover, the measurements are non-contacting with a small receiver footprint. This allows us to record densely-spaced waveforms under computer control. The resulting waveforms provide estimates of the group velocity. Dellinger and Vernik (1994) discuss whether transducer transmission experiments are more likely to measure group or phase velocity. They conclude — based on geometrical arguments — that velocity measurements on core *should* yield the phase velocity, when the ratio of travel distance H to transducer width D is $\frac{H}{D} < 3$; while the measurements yield the group velocity when $\frac{H}{D} > 20$. Unlike contacting transducers, our ultrasonic laser receiver has a small footprint on the order or 50 μm, resulting in a $\frac{H}{D} \gg 100$ for both samples, clearly yielding the group velocity from this criterion. Note that with the

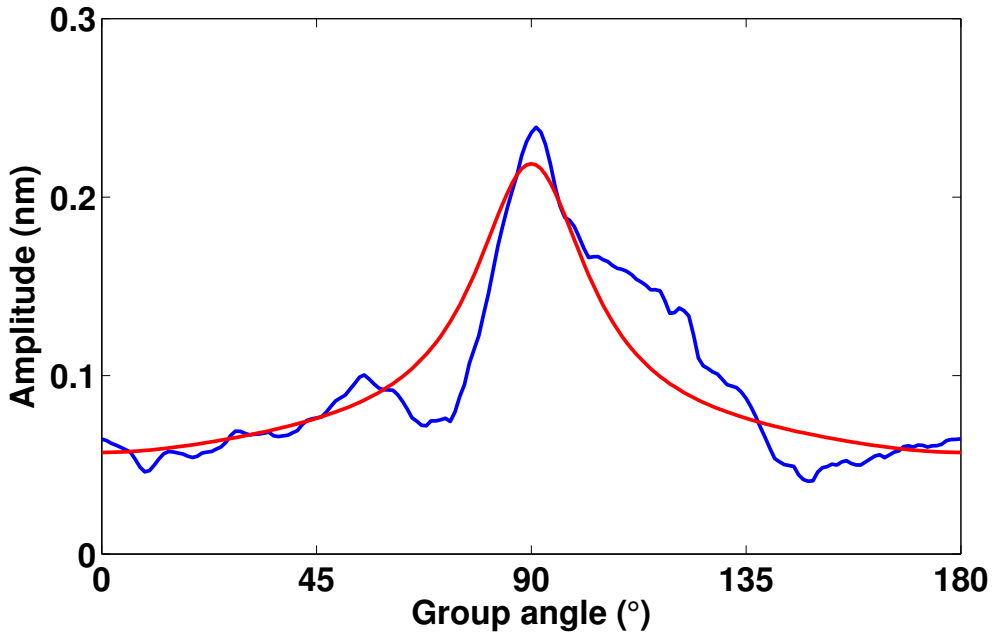

Figure 6.10: Experimental amplitude smoothed with a running average (blue), and wave attenuation anisotropy least-square fit (red) for sample MSH, using Equation (6.10). The best fit is obtained for $\delta_Q = -0.80 \pm 0.23$ and $\epsilon_Q = -0.67 \pm 0.03$.

small laser receiver spot size, we avoid the "gray zone" $3 < \frac{H}{D} < 20$ encountered by many transducer experiments on core. This zone poses difficulty in the interpretation of our transducer measurements. The transducer setup for sample SHC has a $\frac{H}{D} \approx 4$, close to the transition from group to phase velocity. As a result, the velocity estimated from the transducer at $\theta = 45°$ is close to the expected phase velocity, but deviates from our group velocity estimation with the laser method. For sample MSH, the ratio $\frac{H}{D} \approx 6$ is also in the transition zone, but we do not observe significant velocity difference at $\theta = 45°$ when comparing laser and ultrasonic data. This may be because the anisotropy of this sample is weaker, so that phase and group velocity differ less than for sample SHC.

We checked if our samples are *truly* VTI materials with the symmetry axis corre-

sponding to our laboratory acquisition coordinate system. We measure the P-wave velocity propagation on the x_2-axis by placing the laser source and receiver on the sides of the samples parallel to the (x_1, x_3) plane (see Figure 6.2). If the sample is described by a VTI media in the acquisition coordinate system, the x_2-velocity should be equal in magnitude to the fast P-wave velocity observed in Figures 6.6 and 6.7. For both samples, the measurements match closely, confirming that in this case, a VTI representation is an accurate approximation of shale anisotropy.

The observed velocity and amplitude anisotropy in shales can be due to clay mineral composition and alignment (Jones and Wang, 1981; Johnston and Christensen, 1995; Wang, 2002; Dewhurst and Siggins, 2006), layered or lenticular distribution of organic mater and kerogen (Vernik and Nur, 1992; Mba and Prasad, 2010; Sondergeld and Rai, 2011); and the negative value of the δ parameter can be theoretically explained by the alignment and distribution of clay platelets and compliance of the regions between them (Sayers, 2004). The magnitude of our velocity and attenuation anisotropy are almost surely enhanced by delamination and the formation of microfractures parallel to the bedding, resulting from samples drying and in situ stress being released at the surface (Sondergeld and Rai, 2011). In particular, sample SHC has a visible crack parallel to the bedding. As such, the measurements in this publication are meant to illustrate the data acquisition method, and not to be taken as a proper in-situ analysis of these particular shale samples.

P-wave amplitude anisotropy is more difficult to measure than velocity anisotropy, but is shown here to be stronger than velocity anisotropy. In it lies a growing realization that amplitude information has strong potential in understanding the subsurface, even though reliable amplitude information is typically harder to obtain.

The attenuation of waves in the direction perpendicular to layering is observed by Deng *et al.* (2009) and modeled by Carcione (2000), in agreement with our observations. Moreover, Zhu *et al.* (2007) also report large negative values for δ_Q and ϵ_Q in a laboratory study of an anisotropic phenolic sample. We note here that we do not truly satisfy the weak anisotropy conditions assumed in Equation 6.10, since none of $\delta, \epsilon, \delta_Q,$ or ϵ_Q is $\ll 1$ in modulus. They are, however, small enough to give us a qualitative idea of the attenuation anisotropy using the weak anisotropy assumptions.

The data summarized in Table 6.1 agree with published data at room conditions and on dry core (Vernik and Nur, 1992; Bayuk *et al.*, 2009). With these current results in hand, we aim to expand the methodology to preserved shale cores with minimal alteration to the preserving jacket (wax), while keeping the shale from drying. After that, we will address the problem of making these measurements under *in situ* conditions.

6.6 Conclusions

Non-contacting laser ultrasonics allows us to obtain computer-controlled measurements of the wavefields in shales. These measurements are densely sampled in space and time. This technique reduces problems with cutting samples at angles with *a priori* unknown symmetry axes, provides robust estimates of the fast and slow direction of group velocity. In addition to rock properties obtained from travel times, measured amplitudes are absolute and provide attenuation estimates that also relate to the internal structure of the rock. Here, we report anisotropy estimates in velocity and relative attenuation in dry shales, but this is merely a starting point for measurements on preserved samples, and eventually under reservoir conditions.

CHAPTER 7:

CONCLUSION

7.1 Overview

Laser ultrasonic measurements provide a powerful tool to study rock properties and wave propagation in scattering media. The small source and receiver size, as well as the non-contacting characteristics provides numerous advantages over traditional transducer techniques. Throughout this dissertation, we report advances in laser ultrasonics that allows us to test new scattering theory, and develop new paradigms to probe fractures and study rock physics. These datasets are obtained via automatic scans set up under computer control, and are free from ringing and coupling issues common to contacting measurements. We are also able to directly get the absolute displacement field in two component (vertical and horizontal), without need to recalibrate the sensor for each measurement.

We first present a novel laser-based sensor design, adding the capability to record two components of the wavefield simultaneously. After detailing the principles of the method, we demonstrate its use by retrieving the (known) ellipticity of the Rayleigh wave in a homogeneous medium. Although the amplitude of the in-plane component

is more sensitive to the sensor focus than the out-of-plane one, it can be successfully used to measure in-plane displacements on the order of tens of nanometers.

We then apply this laboratory technique to the measurement of scattered waves. We derive a new analytic expression of the scattering amplitude from a single fracture, based on the linear slip model. In an initial step, we use a laser receiver only to test the theoretical results, and find that they are in good agreement with the experimental amplitudes. The estimation of the normal compliance is in the same magnitude range as previously published results for different materials. By modifying the experimental setup, we acquire and analyze both components of the displacement. The in-plane component provides additional information about the SV-SV scattering from the fracture, and, combined with a well-chosen acquisition geometry, improves the estimation of the tangential compliance η_T. A joint-inversion of data from both components then yields estimates of the orientation, size, and compliances of the fracture. By also performing measurements under uniaxial load, we demonstrate the potential of the technique for measurements of rocks undergoing changes in their stress field.

While we first cover applications of the laser receiver, optically-generated elastic waves also presents advantages over traditional sources. We demonstrate one of those in Chapter 5, by directly focusing the source laser inside the sample at the fracture location, effectively turning the fracture into a source of elastic waves. We confirm this by looking at the displacement generated from the tips of the fracture, and compare it to the scattered displacement as studied before. This technique opens the way to localized buried sources for laboratory experiments, with potential applications in earthquake dynamics and material testing.

A classical rock property measurement also illustrates the advantages of laser-based ultrasonic measurements. While elastic constants for VTI materials are typically estimated by using transducer measurements on rocks cut at three different angles, in Chapter 6 we obtain the group traveltime for every degree between the fast and slow direction. The dense velocity data allow for a better estimation of the elastic constants. We simultaneously estimate the attenuation anisotropy from the absolute amplitude of the displacement.

7.2 Future Directions

The non-contacting laboratory setup described in the applications above presents numerous advantages over traditional contacting techniques. The small size of the source and receiver, as well as the absence of ringing issues make it a well-suited tool for the investigation of elastic scattering, since the instrumentation cannot act as a scatterer itself. The non-contacting property allows to perform computer-controlled scans with dozens of source and/or receiver locations, effectively mimicking active seismic surveys, in relatively short acquisition times (on the order of hours to few tens of hours for two-dimensional laboratory surveys). Such a remote-sensing technique is in principle ideally suited to be applied to measurements in hostile conditions, in particular under extreme temperatures and/or pressures. Using optical windows in pressure vessels, it would be possible to measure the elastic properties at reservoir conditions for rocks such as (preserved) shales. It could also be used to further investigate the influence of stress changes on fractures. In a similar fashion, we could apply laser ultrasonics to the characterization of elastic properties of ice at very low temperatures without the need to submit the sensors to these temperatures. I foresee

these advantages opening a realm of geophysical laboratory applications for laser-based elastic wave propagation and detection.

REFERENCES

Aki, K, and Richards, P. G. 2002. *Quantitative Seismology*. 2nd edn. Sausalito, CA: Univ. Science Books.

Arfken, G. B, and Weber, H. 2001. *Mathematical methods for physicists*. 5th edn. Amsterdam: Harcourt.

Bayuk, I. O, Chesnokov, E, Ammerman, M, and Dyaur, N. 2009. Elastic properties of four shales reconstructed from laboratory measurements at unloaded conditions. *SEG Technical Program Expanded Abstracts*, **28**, 241–245.

Ben-David, O, Cohen, G, and Fineberg, J. 2010. The Dynamics of the Onset of Frictional Slip. *Science*, **330**(6001), 211 –214.

Blum, T. E, van Wijk, K, Pouet, B, and Wartelle, A. 2010. Multicomponent wavefield characterization with a novel scanning laser interferometer. *Rev. Sci. Instrum.*, **81**(7), 073101.

Blum, T. E, van Wijk, K, Snieder, R, and Willis, M. E. 2011a. Laser Excitation of a Fracture Source for Elastic Waves. *Phys. Rev. Lett.*, **107**, 275501.

Blum, T. E, Snieder, R, van Wijk, K, and Willis, M. E. 2011b. Theory and laboratory

experiments of elastic wave scattering by dry planar fractures. *J. Geophys. Res.*, **116**, B08218.

Blum, T. E, Adam, L, and van Wijk, K. 2013. Noncontacting benchtop measurements of the elastic properties of shales. *GEOPHYSICS*, **78**(3), C25–C31.

Brandsdóttir, B, and Einarsson, P. 1979. Seismic activity associated with the September 1977 deflation of the Krafla central volcano in northeastern Iceland. *Journal of Volcanology and Geothermal Research*, **6**(3-4), 197–212.

Bretaudeau, F, Leparoux, D, Durand, O, and Abraham, O. 2011. Small-scale modeling of onshore seismic experiment: A tool to validate numerical modeling and seismic imaging methods. *Geophysics*, **76**(5), T101–T112.

Brie, A, Nurmi, R. D, and Johnson, D. L. 1985. Effect of spherical pores on sonic and resistivity measurements. *In: 26th Annual Logging Symposium.* Society of Petrophysicists and Well-Log Analysts.

Cand, A, Monchalin, J, and Jia, X. 1994. Detection of in-plane and out-of-plane ultrasonic displacements by a two-channel confocalFabry-Perot interferometer. *Appl. Phys. Lett.*, **64**(4), 414.

Carcione, J. M. 2000. A model for seismic velocity and attenuation in petroleum source rocks. *Geophysics*, **65**(4), 1080–1092.

Coates, R. T, and Schoenberg, M. A. 1995. Finite-difference modeling of faults and fractures. *Geophysics*, **60**, 1514–1526.

Collettini, C, Niemeijer, A, Viti, C, and Marone, C. 2009. Fault zone fabric and fault weakness. *Nature*, **462**, 907–911.

Crampin, S. 1981. A review of wave motion in anisotropic and cracked elastic media. *Wave Motion*, **3**, 343–391.

Dellinger, J, and Vernik, L. 1994. Do traveltimes in pulse-transmission experiments yield anisotropic group or phase velocities? *Geophysics*, **59**(11), 1774.

Deng, J, Wang, S, and Han, D. 2009. The velocity and attenuation anisotropy of shale at ultrasonic frequency. *Journal of Geophysics and Engineering*, **6**(3), 269.

Dewangan, P, Tsvankin, I, Batzle, M, van Wijk, K, and Haney, M. 2006. PS-wave moveout inversion for tilted TI media: A physical-modeling study. *Geophysics*, **71**(4), D135–D143.

Dewhurst, D. N, and Siggins, A. F. 2006. Impact of fabric, microcracks and stress field on shale anisotropy. *Geophysical Journal International*, **165**(1), 135–148.

Duranti, L, Ewy, R, and Hofmann, R. 2005. Dispersive and attenuative nature of shales: multiscale and multifrequency observations. *SEG Technical Program Expanded Abstracts*, **24**, 1577–1580.

Fang, X, Fehler, M, Chen, T, and Burns, D. R. 2010. Sensitivity analysis of fracture scattering. *SEG Technical Program Expanded Abstracts*, **29**, 2340–2345.

Groenenboom, J, and Falk, J. 2000. Scattering by hydraulic fractures: Finite-difference modeling and laboratory data. *Geophysics*, **65**, 612–622.

Groenenboom, J, and Fokkema, J. T. 1998. Monitoring the width of hydraulic fractures with acoustic waves. *Geophysics*, **63**, 139–148.

Groenenboom, J, and van Dam, D. 2000. Monitoring hydraulic fracture growth: Laboratory experiments. *Geophysics*, **65**, 603–611.

Gross, S. P, Fineberg, J, Marder, M, McCormick, W. D, and Swinney, H. L. 1993. Acoustic emissions from rapidly moving cracks. *Phys. Rev. Lett.*, **71**(19), 3162–3165.

Gu, B, Nihei, K. T, Myer, L. R, and Pyrak-Nolte, L. J. 1996. Fracture interface waves. *J. Geophys. Res.*, **101**(B1), 827–835.

Gubernatis, J, Domany, E, and Krumhansl, J. 1977a. Formal aspects of the theory of scattering of ultrasound by flaws in elastic materials. *J. Appl. Phys.*, **48**, 2804–2811.

Gubernatis, J, Domany, E, Krumhansl, J, and Huberman, M. 1977b. The Born approximation in the theory of the scattering of elastic waves by cracks. *J. Appl. Phys.*, **48**, 2812–2819.

Gudmundsson, A. 2006. How local stresses control magma-chamber ruptures, dyke injections, and eruptions in composite volcanoes. *Earth-Science Reviews*, **79**(1–2), 1–31.

Guilbaud, S, and Audoin, B. 1999. Measurement of the stiffness coefficients of a viscoelastic composite material with laser-generated and detected ultrasound. *The Journal of the Acoustical Society of America*, **105**(4), 2226–2235.

Haney, M. M, Snieder, R, Sheiman, J, and Losh, S. 2005. Geophysics: A moving fluid pulse in a fault zone. *Nature*, **437**(7055), 46.

Helbig, K. 1958. Elastischen Wellen in anisotropen Medien. *Gerlands Beitr. Geophys.*, **67**, 256–288.

Holt, R. M, Bhuiyan, M. H, Kolstø, M. I, Bakk, A, Stenebraten, J. F, and Fjær, E. 2011. Stress-induced versus lithological anisotropy in compacted claystones and soft shales. *The Leading Edge*, **30**(3), 312–317.

Hornby, B. E. 1998. Experimental laboratory determination of the dynamic elastic properties of wet, drained shales. *Journal of Geophysical Research*, **103**(B12), 945–964.

Hsu, C.-J, and Schoenberg, M. 1993. Elastic waves through a simulated fractured medium. *Geophysics*, **58**(7), 964–977.

Hudson, J. A. 1981. Wave speeds and attenuation of elastic waves in materials containing cracks. *Geophys. J. R. Astron. Soc.*, **64**, 133–150.

Hudson, J. A, Liu, E, and Crampin, S. 1997. The mean transmission properties of a fault with imperfect facial contact. *Geophysical Journal International*, **129**(3), 720–726.

Johnston, J. E, and Christensen, N. I. 1995. Seismic anisotropy of shales. *Journal of Geophysical Research*, **100**(B4), 5991–6003.

Jones, L. E. A, and Wang, H. F. 1981. Ultrasonic velocities in Cretaceous shales from the Williston basin. *Geophysics*, **46**(3), 288–297.

Kachanov, M, and Sevostianov, I. 2005. On quantitative characterization of microstructures and effective properties. *Int. J. of Solids and Structures*, **42**, 309–336.

Keller, J. 1978. Rays, Waves and Asymptotics. *Bull. Am. Math. Soc.*, **84**, 727–750.

Langenberg, K, Marklein, R, and Mayer, K. 2002. Applications to nondestructive testing with ultrasound. *Pages 594–617 of:* Sabatier, P, and Pike, E (eds), *Scattering and inverse scattering in pure and applied science*. Academic Press, San Diego.

Larose, E, Planes, T, Rossetto, V, and Margerin, L. 2010. Locating a small change in a multiple scattering environment. *Appl. Phys. Lett.*, **96**(20), 204101.

Lebedev, M, Bona, A, Pevzner, R, and Gurevich, B. 2011. Elastic anisotropy estimation from laboratory measurements of velocity and polarization of quasi-P-waves using laser interferometry. *Geophysics*, **76**(3), WA83–WA89.

Liu, E, Hudson, J. A, and Pointer, T. 2000. Equivalent medium representation of fractured rock. *Journal of Geophysical Research*, **105**(B2), 2981–3000.

Lubbe, R, Sothcott, J, Worthington, M, and McCann, C. 2008. Laboratory estimates of normal and shear fracture compliance. *Geophysical Prospecting*, **56**(2), 239–247.

Malischewsky, P. G, and Scherbaum, F. 2004. Love's formula and H/V-ratio (ellipticity) of Rayleigh waves. *Wave Motion*, **40**(1), 57–67.

Martin, P. 2006. *Multiple scattering*. Encyclopedia of mathematics and its applications, vol. 107. Cambridge, UK: Cambridge Univ. Press.

Masserey, B, and Mazza, E. 2005. Analysis of the near-field ultrasonic scattering at a surface crack. *J. Acoust. Soc. Am.*, **118**(6), 3585.

Mba, K, and Prasad, M. 2010. Mineralogy and its contribution to anisotropy and kerogen stiffness variations with maturity in the Bakken Shales. *SEG Technical Program Expanded Abstracts*, **29**, 2612–2616.

Meadows, M. A, and Winterstein, D. 1994. Seismic detection of a hydraulic fracture from shear wave VSP data at Lost Hills Field, California. *Geophysics*, **59**, 11–26.

Merzbacher, E. 1970. *Quantum Mechanics*. 2nd edn. New York: Wiley.

Miller, D. E, Horne, S. A, and Walsh, J. 2012. Precise inversion of logged slownesses for elastic parameters in a gas shale formation. *Geophysics*, **77**(4), B197–B206.

Nakahara, H, Sato, H, Nishimura, T, and Fujiwara, H. 2011. Direct observation of rupture propagation during the 2011 off the Pacific coast of Tohoku, Japan, earthquake (Mw 9.0) using a small seismic array. *Earth Planets Space*, **63**(Sept.), 589–594.

Nishizawa, O, Satoh, T, and Lei, X. 1998. Detection of shear wave in ultrasonic range by using a laser Doppler vibrometer. *Rev. Sci. Instrum.*, **69**(6), 2572–2573.

Ogi, H, Nakamura, N, Sato, K, Hirao, M, and Uda, S. 2003. Elastic, anelastic, and piezoelectric coefficients of langasite: resonance ultrasound spectroscopy with laser-Doppler interferometry. *IEEE Transactions on Ultrasonics, Ferroelectrics and Frequency Control*, **50**(5), 553 –560.

Pouet, B, and Rasolofosaon, P. N. J. 1990. Seismic physical modeling using laser ultrasonics. *SEG Technical Program Expanded Abstracts*, **9**, 841–844.

Pyrak-Nolte, L. J. 2000. Monitoring fracture evolution with compressional-mode interface waves. *J. Geophys. Res.*, **27**, 3397–3400.

Pyrak-Nolte, L. J, and Nolte, D. D. 1992. Frequency dependence of fracture stiffness. *Geophys. Res. Lett.*, **19**, 325–328.

Pyrak-Nolte, L. J, Myer, L. R, and Cook, N. G. W. 1990a. Anisotropy in Seismic Velocities and Amplitudes From Multiple Parallel Fractures. *Journal of Geophysical Research*, **95**(B7), 11345–11358.

Pyrak-Nolte, L. J, Myer, L. R, and Cook, N. G. W. 1990b. Transmission of seismic waves across a single natural fracture. *J. Geophys. Res.*, **95**(B6), 8617–8638.

Pyrak-Nolte, L. J, Xu, J, and Haley, G. 1992. Elastic Interface Waves Along a Fracture: Theory and Experiment. *Pages 999–1007 of:* Tillerson, and Wawersik (eds), *Proc. 33rd U.S. Rock. Mech. Symp.* Rotterdam: Balkema.

Pyrak-Nolte, L. J, Roy, S, and Mullenbach, B. 1996. Interface waves propagated along a fracture. *J. Appl. Geophys.*, **35**, 79–87.

Roy, S, and Pyrak-Nolte, L. J. 1997. Observation of a distinct compressionalmode interface wave on a single fracture. *Geophys. Res. Lett.*, **24**(2), 173–176.

Rudzki, M. P. 1911. Parametrische Darstellung der elastischen Wellen in anisotropischen Medien. *Bull. Acad. Cracovie*, 503.

Saleh, A. A, and Castagna, J. P. 2004. Revisiting the Wyllie time average equation in the case of near-spherical pores. *Geophysics*, **69**(1), 45–55.

Sánchez-Sesma, F. J, and Iturrarán-Viveros, U. 2001. Scattering and diffraction by SH waves by a finite crack: an analytical solution. *Geophys. J. Int.*, **145**, 749–758.

Sarker, R, and Batzle, M. 2010. Anisotropic elastic moduli of the Mancos B Shale- An experimental study. *SEG Technical Program Expanded Abstracts*, **29**, 2600–2605.

Sawazaki, K, and Snieder, R. 2013. Time-lapse changes of P- and S-wave velocities and shear wave splitting in the first year after the 2011 Tohoku earthquake, Japan: shallow subsurface. *Geophys. J. Int.*, Jan.

Sayers, C. M. 2004. Seismic anisotropy of shales: What determines the sign of Thomsen's delta parameter? *SEG Technical Program Expanded Abstracts*, **23**, 103–106.

Scales, J. A, and Malcolm, A. E. 2003. Laser characterization of ultrasonic wave propagation in random media. *Physical Review E*, **67**(4), 046618.

Schoenberg, M. A. 1980. Elastic Wave Behavior Across Linear Slip Interfaces. *J. Acoust. Soc. Am.*, **68**, 1516–1521.

Schoenberg, M. A, and Douma, J. 1988. Elastic wave propagation in media with parallel fractures and aligned cracks. *Geophys. Prosp.*, **36**, 571–590.

Schoenberg, M. A, and Sayers, C. M. 1995. Seismic anisotropy of fractured rock. *Geophysics*, **60**, 204–211.

Scholz, C. 1990. *The Mechanics of Earthquakes and Faulting*. Cambridge UK: Cambridge Univ. Press.

Scruby, C. B, and Drain, L. E. 1990. *Laser Ultrasonics Techniques and Applications*. 1st edn. Taylor & Francis.

Smyshlyaev, V, and Willis, J. 1994. Linear ad nonlinear scattering of elastic waves by microcracks. *J. Mech. Phys. Solids*, **42**, 585–610.

Snieder, R. 2009. *A Guided Tour of Mathematical Methods: For the Physical Sciences*. 2nd edn. Cambridge University Press.

Sondergeld, C. H, and Rai, C. S. 2011. Elastic anisotropy of shales. *The Leading Edge*, **30**(3), 324–331.

Stein, S, and Wysession, M. 2002. *An Introduction to Seismology, Earthquakes and Earth Structure*. 1st edn. Wiley-Blackwell.

Suarez-Rivera, R, Green, S, McLennan, J, and Bai, M. 2006. Effect of Layered Heterogeneity on Fracture Initiation in Tight Gas Shales. *SPE Annual Technical Conference and Exhibition Proceedings*, Sept.

Thompson, B. D, Young, R. P, and Lockner, D. A. 2009. Premonitory acoustic emissions and stick-slip in natural and smooth-faulted Westerly granite. *J. Geophys. Res.*, **114**, B02205.

Thomsen, L. 1986. Weak elastic anisotropy. *Geophysics*, **51**(10), 1954–1966.

Tsvankin, I. 2001. *Seismic Signatures and Analysis of Reflection Data in Anisotropic Media, Volume 29*. 1 edn. Pergamon.

Vernik, L, and Nur, A. 1992. Ultrasonic velocity and anisotropy of hydrocarbon source rocks. *Geophysics*, **57**(5), 727–735.

Wang, Z. 2002. Seismic anisotropy in sedimentary rocks, part 1: A singleplug laboratory method. *Geophysics*, **67**(5), 1415–1422.

Wills, P, DeMartini, D, Vinegar, H, Shlyapobersky, J, Deeg, W, Woerpel, J, Fix, J, Sorrelis, G, and Adair, R. 1992. Active and passive imaging of hydraulic fractures. *The Leading Edge*, **11**(7), 15–22.

Worthington, M. 2007. The compliance of macrofractures. *The Leading Edge*, **26**, 1118–1121.

Wu, C, Harris, J. M, Nihei, K. T, and Nakagawa, S. 2005. Two-dimensional finite-difference seismic modeling of an open fluid-filled fracture: Comparison of thin-layer and linear-slip models. *Geophysics*, **70**(4), T57.

Wu, R, and Aki, K. 1985. Scattering Characteristics of Elastic Waves by an Elastic Heterogeneity. *Geophysics*, **50**, 582–595.

Zadler, B. J, and Scales, J. A. 2008. Monitoring crack-induced changes in elasticity with resonant spectroscopy. *J. Appl. Phys.*, **104**(2), 023536–4.

Zhu, Y, and Snieder, R. 2002. Reflected and transmitted waves from fault zones. *SEG Technical Program Expanded Abstracts*, **21**, 2273–2276.

Zhu, Y, and Tsvankin, I. 2006. Plane-wave propagation in attenuative transversely isotropic media. *Geophysics*, **71**(2), T17.

Zhu, Y, Tsvankin, I, Dewangan, P, and van Wijk, K. 2007. Physical modeling and analysis of P-wave attenuation anisotropy in transversely isotropic media. *Geophysics*, **72**(1), D1.

APPENDIX A:

IN-PLANE FOCUS CHARACTERIZATION

Summary

In order to better characterize the in-plane measurement sensitivity to focus of the interferometer described in Chapter 2, we present here a study of noise versus focus, and how it affects the Raleigh wave ellipticity measurement.

A.1 Focus Sensitivity

We first measure the noise level for both channels as function of focus. Figure A.1 shows how quickly the in-plane noise level increases, and therefore the signal-to-noise ratio (SNR) degrades, when moving out of focus. The focus positioning accuracy is not as critical for the out-of-plane detection, therefore we still get a good SNR on the out-of-plane when out-of-focus.

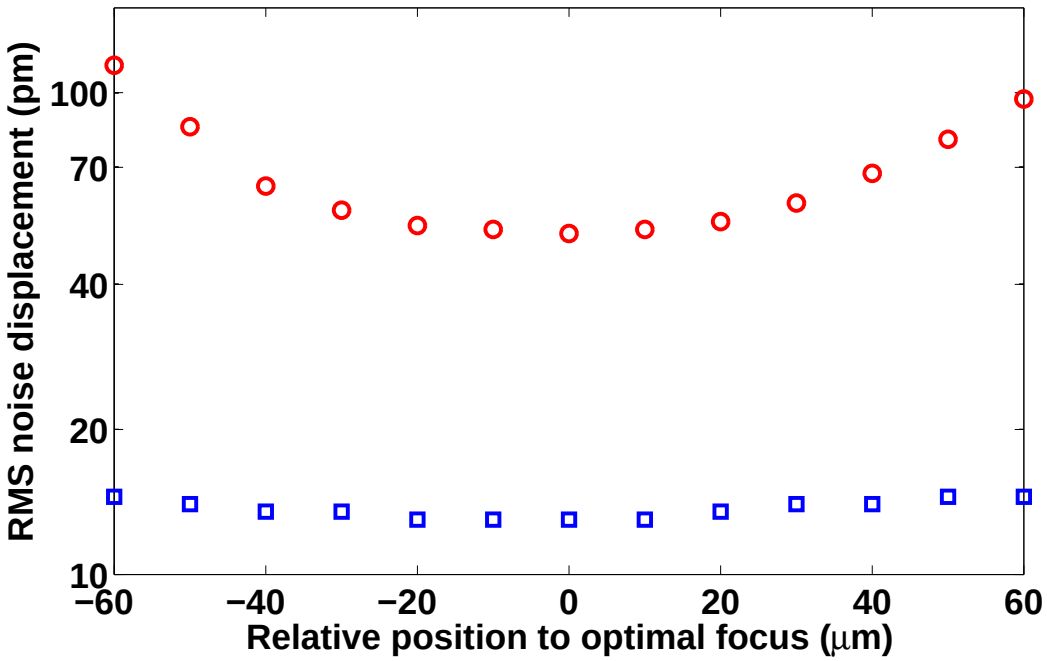

Figure A.1: RMS noise displacement (in picometer) measured on the in-plane (circles) and out-of-plane (squares) channels as the beam looses focus. The RMS value is taken over the 0-20 MHz bandwidth.

A.2 Effect on H/V Ratio and Phase

To understand one source of the variance in the amplitude and phase measurements, we investigate the focus of the light at a single source-detector distance of 50 mm. For each focus setting, we record the RMS value of the noise on the in-plane channel. We consider the measurement with the least amount of noise as the best focus, and present other points by their relative RMS noise increase compared to the best focus in percent. Furthermore, negative values of RMS noise increase represent measurements for which the focal plane is ahead of the sample surface. Conversely, measurements with a focal plane behind the sample surface are noted with a positive RMS noise increase. The signal is filtered as in Section 2.4. The results are presented in Fig-

ure A.2. We see here that the value of the ratio for the measurement considered optimally focused is 0.64 ± 0.02, but quickly changes with the focal position. The phase difference, on the other hand, does not seem to be affected by the noise level (and therefore focal position), and stays between 96° and 100° for the range of focal positions covered here. In conclusion, a focal error of 10 μm or more is enough to get a wrong estimate of the in-plane displacement amplitude.

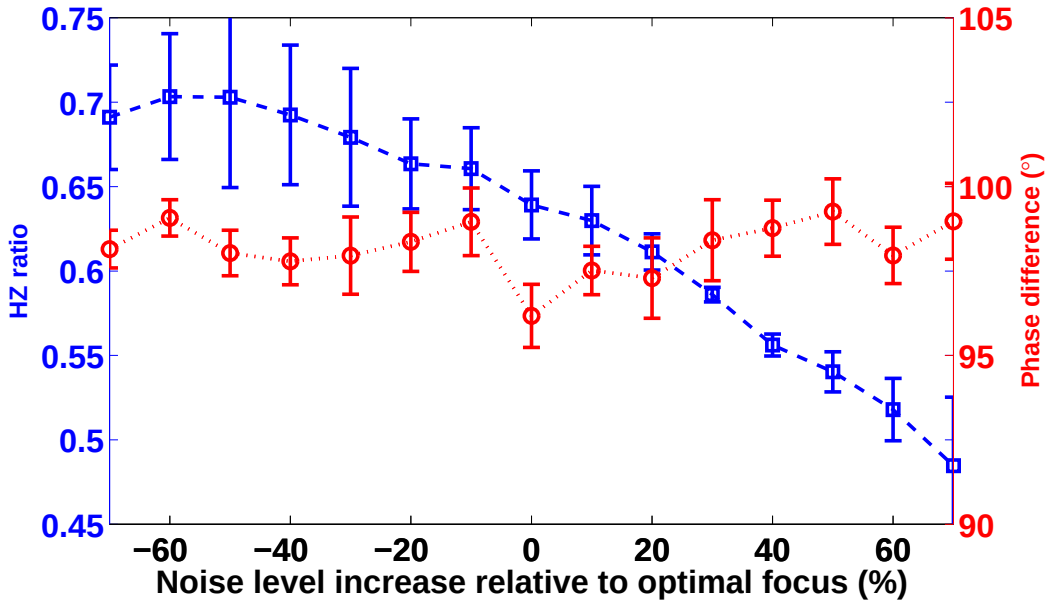

Figure A.2: Ratio (squares) and phase difference (circles) dependency versus focus quality for a Rayleigh wave detection at 50 mm offset.

APPENDIX B:

EFFECTS OF REFLECTIVE TAPE ON LASER ULTRASONICS MEASUREMENTS

Summary

For most of the laboratory measurements presented in this work, we use metallic tape in order to reflect the receiver laser light from dark or transparent samples, but also for the latter to absorb the source infrared light. While the description of laser ultrasonic sources is out of the scope of this work, we seek to characterize the influence of the tape on the receiver side. We compare two tapes: a copper tape and an aluminum tape. Both tapes have a metal layer 50 μm thick for a total thickness with adhesive backing of 90 μm. In our laboratory measurements, we do not encounter wavelengths shorter than one millimeter. Therefore, the tape thickness is always less than a tenth of the wavelength, and should not act as an interface for elastic waves. The added thickness can however bring a time-delay. We investigate this effect here, and show that the aluminum tape has small effects on the amplitude, and introduces a short time-delay taken in account during processing steps.

B.1 Influence of Tape

We use a piezolectric transducer as a source, which generates a central frequency of 500 kHz. The transducer is coupled to a piece of aluminum, 145 mm thick; it is thick enough to assume an incoming plane wave. We compare the two tapes by recording signal without any tape, and then separately with each kind of tape. We first use a compressional transducer to measure the P-wave response of the tapes, and measure the response on the out-of-plane signal of the interferometer. The comparison between each surface is shown in Figure B.1. We see that both tapes introduce a small delay and we estimate it by measuring the time of the maximum in the cross-correlation of a signal with tape and the signal with the bare sample. We get a delay of 0.02 μs for the aluminum tape and 0.06 μs for the copper tape.

We then perform a similar measurement with a shear transducer and measure the S-wave arrival on the in-plane channel. The resulting comparison is shown in Figure B.2. The delays are in this case 0.02 μs for the aluminum tape and 0.06 μs for the copper tape.

We also notice that the presence of tape changes the amplitude of the signal. For the out-of-plane component measured with the P-wave source, the aluminum tape increases the amplitude of the signal by approximately 8%, and the copper tape by 23%. For the in-plane component measured using the S-wave transducer, the changes are higher. The signal amplitude is increased by 48% with the aluminum tape, and decreased by 18% with the copper tape.

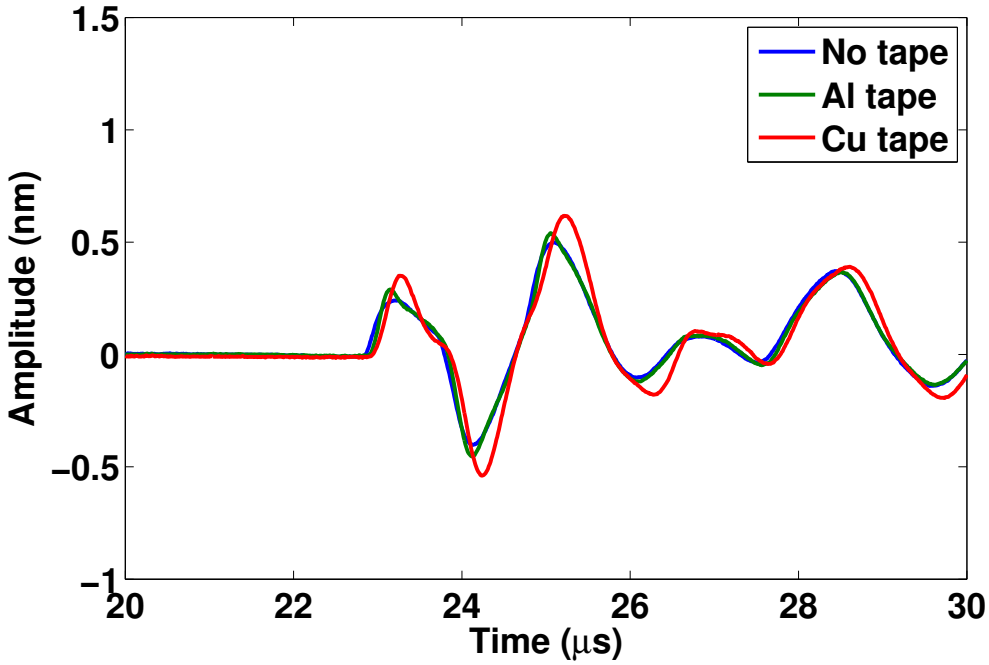

Figure B.1: Time arrivals of a direct P-wave measured on an aluminum sample with different tapes. The addition of copper or aluminum tape does not modify the amplitudes, but adds a delay of 0.02 μs for the aluminum tape and 0.06 μs for the copper tape.

B.2 Conclusion

The aluminum tape introduces minimal delays compared to the period of the signals of interests. We opt to use this tape and nonetheless compensate for the introduced delay during the processing steps. The wide amplitude variations for the S-wave arrival can be explained by the high sensitivity of the in-plane channel to the focal position, as shown in Appendix A. The amplitude of the in-plane component is solely used in Chapter 4. In that case, we normalize the scattered arrival by the reflected arrival, and assume that the bias in amplitude stays the same for both events.

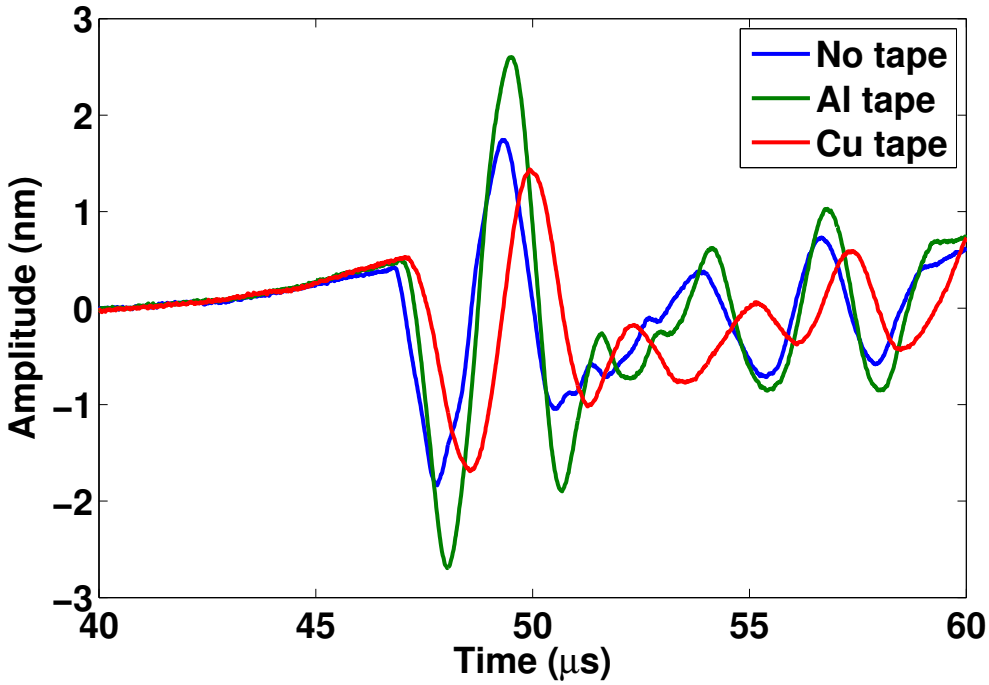

Figure B.2: Time arrivals of a direct S-wave measured on an aluminum sample with different tapes. The addition of copper or aluminum tape does not modify the amplitudes, but adds a delay of 0.16 μs for the aluminum tape and 0.67 μs for the copper tape.

APPENDIX C:

DETAILS OF THE SCATTERING AMPLITUDE DERIVATION

Summary

In this appendix, we give in detail three steps of the derivation of the scattering amplitude. We first show how to get the N_{ijkl} used in Equation (3.9). We then show how to derive the scattering amplitudes in Expressions (3.27)–(3.30). Finally, we describe the simplification of $F(\mathbf{k})$ for a circular crack.

C.1 Derivation of N_{ijkl} for an Isotropic Medium

Inserting the expression for the elasticity tensor for an isotropic medium and Equation (3.8) into definition (3.7) of N_{ijkl} gives

$$N_{ijkl} = \{\eta_N f_p f_i + \eta_T(\delta_{pi} - f_p f_i)\}\, f_j f_q \left\{\lambda\delta_{pq}\delta_{kl} + \mu\delta_{pk}\delta_{ql} + \mu\delta_{pl}\delta_{qk}\right\} \ . \tag{C.1}$$

Carrying out the multiplication and summing over the variables of the delta functions gives

$$\begin{aligned} N_{ijkl} =& \lambda\delta_{kl}\left\{\eta_N f_p f_i f_j f_p + \eta_T f_j f_i - \eta_T f_p f_i f_j f_p\right\} \\ &+ \mu\left\{\eta_N f_k f_i f_j f_l + \eta_T \delta_{ik} f_j f_l - \eta_T f_k f_i f_j f_l\right\} \\ &+ \mu\left\{\eta_N f_l f_i f_j f_k + \eta_T \delta_{il} f_j f_k - \eta_T f_l f_i f_j f_k\right\} \ . \end{aligned} \tag{C.2}$$

Since the vectors $\hat{\mathbf{f}}$, $\hat{\mathbf{n}}$, $\hat{\mathbf{p}}$, $\hat{\mathbf{m}}$ and $\hat{\mathbf{q}}$ are unit vectors

$$f_j f_j = n_j n_j = p_j p_j = m_j m_j = q_j q_j = 1 \ . \tag{C.3}$$

Using this in Equation (C.2), and combining terms, leads to Expression (3.9).

C.2 Derivation of the Scattering Amplitude

In order to derive f_{PP}, the stress (3.13) of an incoming P wave and Equation (3.9) combine to give

$$\begin{aligned} \sigma_{ij}^{(P)} N_{ijkl} m_k m_l =& \, i k_\alpha e^{i k_\alpha (\hat{\mathbf{n}}\cdot\mathbf{s})} \\ &\times \left\{\lambda^2 \eta_N f_i f_i m_k m_k + 2\lambda\mu(\eta_N - \eta_T) f_i f_i f_k f_l m_k m_l \right. \\ &+ \lambda\mu\eta_T f_i f_l m_i m_l + \lambda\mu\eta_T f_i f_k m_k m_i + 2\lambda\mu\eta_N n_i n_j f_i f_j m_k m_k \\ &+ 4\mu^2(\eta_N - \eta_T) n_i n_j f_i f_j f_k f_l m_k m_l + 2\mu^2 \eta_T n_i n_j f_j f_l m_i m_l \\ &\left. + 2\mu^2 \eta_T n_i n_j f_j f_k m_i m_k \right\} \ . \end{aligned} \tag{C.4}$$

Combinations, such as $n_i f_i$, are dot products and reduce to $(\hat{\mathbf{n}} \cdot \hat{\mathbf{f}})$. Using this, and the normalization (C.3) in Expression (C.4), gives after combining terms

$$\begin{aligned}\sigma_{ij}^{(P)} N_{ijkl} m_k m_l = & ik_\alpha e^{ik_\alpha(\hat{\mathbf{n}}\cdot\mathbf{s})} \times \Big\{ \lambda^2 \eta_N + 2\lambda\mu\eta_N \left((\hat{\mathbf{n}} \cdot \hat{\mathbf{f}})^2 + (\hat{\mathbf{m}} \cdot \hat{\mathbf{f}})^2 \right) \\ & + 4\mu^2 (\eta_N - \eta_T)(\hat{\mathbf{n}} \cdot \hat{\mathbf{f}})^2 (\hat{\mathbf{m}} \cdot \hat{\mathbf{f}})^2 \\ & + 4\mu^2 \eta_T (\hat{\mathbf{n}} \cdot \hat{\mathbf{m}})(\hat{\mathbf{n}} \cdot \hat{\mathbf{f}})(\hat{\mathbf{m}} \cdot \hat{\mathbf{f}}) \Big\} . \end{aligned} \tag{C.5}$$

Inserting this in Equation (3.24), using that $k_\alpha = \omega/\alpha$ and definition (3.26) for $F(\mathbf{k})$, gives Expression (3.27).

Similar steps for P to S scattering give

$$\begin{aligned}\sigma_{ij}^{(P)} N_{ijkl} q_k m_l = & ik_\alpha e^{ik_\alpha(\hat{\mathbf{n}}\cdot\mathbf{s})} \\ & \times \left\{ \lambda^2 \eta_N f_i f_i q_k m_k + 2\lambda\mu\eta_N f_i f_j n_i n_j q_k m_k \right. \\ & + 2\lambda\mu(\eta_N - \eta_T) f_i f_i f_k f_l q_k m_l \\ & + 4\mu^2 (\eta_N - \eta_T) n_i n_j f_i f_j f_k f_l q_k m_l \\ & + \lambda\mu\eta_T f_i f_l q_i m_l + 2\mu^2 \eta_T n_i n_j f_j f_l q_i m_l \\ & \left. + \lambda\mu\eta_T f_i f_k q_k m_i + 2\mu^2 \eta_T n_i n_j f_j f_k q_k m_i \right\} . \end{aligned} \tag{C.6}$$

The polarization of the outgoing S wave is perpendicular to the direction of propagation, hence

$$q_k m_k = (\hat{\mathbf{q}} \cdot \hat{\mathbf{m}}) = 0 , \tag{C.7}$$

hence the first two terms in the right hand side of Expression (C.6) vanish. Using

this, and the normalization (C.3), gives

$$\begin{aligned}\sigma_{ij}^{(P)} N_{ijkl} q_k m_l = & ik_\alpha e^{ik_\alpha(\hat{\mathbf{n}}\cdot\mathbf{s})} \\ & \times \Big\{ 2\lambda\mu\eta_N(\hat{\mathbf{m}}\cdot\hat{\mathbf{f}})(\hat{\mathbf{q}}\cdot\hat{\mathbf{f}}) + 4\mu^2(\eta_N-\eta_T)(\hat{\mathbf{n}}\cdot\hat{\mathbf{f}})^2(\hat{\mathbf{m}}\cdot\hat{\mathbf{f}})(\hat{\mathbf{q}}\cdot\hat{\mathbf{f}}) \\ & +2\mu^2\eta_T(\hat{\mathbf{n}}\cdot\hat{\mathbf{f}})(\hat{\mathbf{m}}\cdot\hat{\mathbf{f}})\left((\hat{\mathbf{n}}\cdot\hat{\mathbf{q}})+(\hat{\mathbf{n}}\cdot\hat{\mathbf{m}})\right)\Big\} \ . \end{aligned} \tag{C.8}$$

Using this in Expression (3.25) leads, with definition (3.26), to Equation (3.28).

For S to P scattering, we use Expression (3.16) for the stress, hence

$$\begin{aligned}\sigma_{ij}^{(S)} N_{ijkl} m_k m_l = & ik_\beta e^{ik_\beta(\hat{\mathbf{n}}\cdot\mathbf{s})} \\ & \times \{\lambda\mu\eta_N n_i p_j f_i f_j m_k m_k + \lambda\mu\eta_N n_j p_i f_i f_j m_k m_k \\ & + 2\mu^2(\eta_N-\eta_T) n_i p_j f_i f_j f_k f_l m_k m_l \\ & + 2\mu^2(\eta_N-\eta_T) n_j p_i f_i f_j f_k f_l m_k m_l \\ & + \mu^2\eta_T n_i p_j f_j f_l m_i m_l + \mu^2\eta_T n_j p_i f_j f_l m_i m_l \\ & +\mu^2\eta_T n_i p_j f_j f_k m_i m_k + \mu^2\eta_T n_j p_i f_j f_k m_i m_k\} \ . \end{aligned} \tag{C.9}$$

Using Expression (C.3), this can be reorganized as

$$\begin{aligned}\sigma_{ij}^{(S)} N_{ijkl} m_k m_l = & ik_\beta e^{ik_\beta(\hat{\mathbf{n}}\cdot\mathbf{s})} \\ & \times \Big\{ 2\lambda\mu\eta_N(\hat{\mathbf{n}}\cdot\hat{\mathbf{f}})(\hat{\mathbf{p}}\cdot\hat{\mathbf{f}}) + 4\mu^2(\eta_N-\eta_T)(\hat{\mathbf{n}}\cdot\hat{\mathbf{f}})(\hat{\mathbf{p}}\cdot\hat{\mathbf{f}})(\hat{\mathbf{m}}\cdot\hat{\mathbf{f}})^2 \\ & +2\mu^2\eta_T(\hat{\mathbf{m}}\cdot\hat{\mathbf{f}})\Big((\hat{\mathbf{n}}\cdot\hat{\mathbf{m}})(\hat{\mathbf{p}}\cdot\hat{\mathbf{f}})+(\hat{\mathbf{p}}\cdot\hat{\mathbf{m}})(\hat{\mathbf{n}}\cdot\hat{\mathbf{f}})\Big)\Big\} \ . \end{aligned} \tag{C.10}$$

Inserting this in Equation (3.24) leads with Expression (3.26) to the S to P scattering amplitude (3.29).

Finally, the S to S scattering amplitude follows from the same steps:

$$\begin{aligned}\sigma_{ij}^{(S)} N_{ijkl} q_k m_l = & ik_\beta e^{ik_\beta(\hat{\mathbf{n}}\cdot\mathbf{s})} \\ & \times \left\{ \lambda^2 \mu \eta_N n_i p_j f_i f_j q_k m_k + \lambda^2 \mu \eta_N n_j p_i f_i f_j q_k m_k \right. \\ & + 2\mu^2 (\eta_N - \eta_T) \left(n_i p_j f_i f_j f_k f_l q_k m_l + n_j p_i f_i f_j f_k f_l q_k m_l \right) \\ & + \mu^2 \eta_T n_i p_j f_j f_l q_i m_l + \mu^2 \eta_T n_j p_i f_j f_l q_i m_l \\ & \left. + \mu^2 \eta_T n_i p_j f_j f_k q_k m_i + \mu^2 \eta_T n_j p_i f_j f_k q_k m_i \right\} \ . \end{aligned} \tag{C.11}$$

The polarization vector $\hat{\mathbf{q}}$ of the outgoing S wave is perpendicular to the direction of propagation, hence $q_k m_k = (\hat{\mathbf{m}} \cdot \hat{\mathbf{q}}) = 0$, and the terms proportional to λ vanish. The remaining terms are, in vector notation, given by

$$\begin{aligned}\sigma_{ij}^{(S)} N_{ijkl} q_k m_l = & ik_\beta e^{ik_\beta(\hat{\mathbf{n}}\cdot\mathbf{s})} \mu^2 \\ & \times \Big\{ 4(\eta_N - \eta_T)(\hat{\mathbf{n}} \cdot \hat{\mathbf{f}})(\hat{\mathbf{p}} \cdot \hat{\mathbf{f}})(\hat{\mathbf{m}} \cdot \hat{\mathbf{f}})(\hat{\mathbf{q}} \cdot \hat{\mathbf{f}}) \\ & + \eta_T (\hat{\mathbf{n}} \cdot \hat{\mathbf{q}})(\hat{\mathbf{p}} \cdot \hat{\mathbf{f}})(\hat{\mathbf{m}} \cdot \hat{\mathbf{f}}) + \eta_T (\hat{\mathbf{n}} \cdot \hat{\mathbf{f}})(\hat{\mathbf{p}} \cdot \hat{\mathbf{q}})(\hat{\mathbf{m}} \cdot \hat{\mathbf{f}}) \\ & + \eta_T (\hat{\mathbf{n}} \cdot \hat{\mathbf{m}})(\hat{\mathbf{p}} \cdot \hat{\mathbf{f}})(\hat{\mathbf{q}} \cdot \hat{\mathbf{f}}) + \eta_T (\hat{\mathbf{n}} \cdot \hat{\mathbf{f}})(\hat{\mathbf{p}} \cdot \hat{\mathbf{m}})(\hat{\mathbf{q}} \cdot \hat{\mathbf{f}}) \Big\} \ . \end{aligned} \tag{C.12}$$

Using this, and definition (3.26), in Expression (3.25) gives Equation (3.30).

C.3 $F(\mathbf{k})$ for a Circular Crack

Following definition (3.26), the form factor for a circular crack with radius a is given by

$$F(\mathbf{k}) = A^{-1} \iint_\Sigma e^{i(\mathbf{k}\cdot\mathbf{s})} d^2 s = A^{-1} \int_0^a \int_0^{2\pi} e^{ik_\parallel s \cos\xi} d\xi s ds \ , \tag{C.13}$$

where ξ is the angle between the projection of $\mathbf{k}$ on the fracture and the integration variable $\mathbf{s}$. The integral representation of the Bessel function as given in Expression (11.30c) of Arfken and Weber (2001) $\left(2\pi J_0(x) = \int_0^{2\pi} e^{ix\cos\xi} d\xi\right)$ reduces Expression (C.13) to

$$F(\mathbf{k}) = A^{-1} \iint_{\Sigma} e^{i(\mathbf{k}\cdot\mathbf{s})} d^2 s = \frac{2\pi}{A} \int_0^a s J_0(k_\parallel s) ds \ , \tag{C.14}$$

where J_0 is the Bessel function of order zero. We next use the recursive relation

$$d(x^n J_n(x))/dx = x^n J_{n-1}(x) \tag{C.15}$$

(Equation (11.15) of Arfken and Weber (2001)). Setting $n = 1$ and $x = k_\parallel s$ gives

$$s J_0(k_\parallel s) = k_\parallel^{-1} \frac{d}{ds} \left(s J_1(k_\parallel s)\right) \ . \tag{C.16}$$

Inserting this in expression (C.14) yields

$$F(\mathbf{k}) = \frac{2\pi}{k_\parallel A} \int_0^a \frac{d}{ds} \left(s J_1(k_\parallel s)\right) ds = \frac{2\pi}{k_\parallel A} a J_1(k_\parallel a) \ . \tag{C.17}$$

Using that $A = \pi a^2$ gives Equation (3.33).

APPENDIX D:

TIP-DIFFRACTION TIMES FROM FORM FACTOR

Summary

This appendix shows how we obtain the tip-diffraction times used in Chapter 5, from the form-factor introduced in Chapter 3.

D.1 Derivation of the Tip-Diffraction Times

Equation (3.27) shows that the P to P scattered amplitude for a planar fracture in a linear-slip model under the Born approximation is

$$f_{P,P}(\hat{\mathbf{n}};\hat{\mathbf{m}}) = \frac{\omega^2}{4\pi\rho\alpha^4} AF\left(k_\alpha(\hat{\mathbf{n}}-\hat{\mathbf{m}})\right)\Big\{\lambda^2\eta_N + 2\lambda\mu\eta_N\left((\hat{\mathbf{n}}\cdot\hat{\mathbf{f}})^2 + (\hat{\mathbf{m}}\cdot\hat{\mathbf{f}})^2\right) + 4\mu^2(\eta_N-\eta_T)(\hat{\mathbf{n}}\cdot\hat{\mathbf{f}})^2(\hat{\mathbf{m}}\cdot\hat{\mathbf{f}})^2 + 4\mu^2\eta_T(\hat{\mathbf{n}}\cdot\hat{\mathbf{m}})(\hat{\mathbf{n}}\cdot\hat{\mathbf{f}})(\hat{\mathbf{m}}\cdot\hat{\mathbf{f}})\Big\}, \quad \text{(D.1)}$$

where ω is the angular frequency, α the P-wave velocity, ρ the density of the material, λ and μ the Lamé parameters, A the surface area of the fracture, and η_N and η_T the normal and tangential compliances, respectively, for the linear-slip model. The unit vectors $\hat{\mathbf{n}}$ and $\hat{\mathbf{m}}$ denote the directions of incoming and outgoing waves, respectively, and $\hat{\mathbf{f}}$ is the unit vector normal to the fracture (see Figure 5.3).

The prefactor $(\omega^2/4\pi\rho\alpha^4)A$ does not carry time information. The factor in curly brackets contains the angular dependence of the scattering amplitude, and depends only on the mechanical properties of the fracture η_N and η_T of the sample material, and on the directions of the incoming and outgoing waves relative to the fracture orientation. The form factor $F\left(k_\alpha(\hat{\mathbf{n}}-\hat{\mathbf{m}})\right)$ depends on the fracture size and shape, and contains travel time information. For the case of a circular fracture, the form factor can be expressed as Equation (3.33):

$$F\left(k_\alpha(\hat{\mathbf{n}}-\hat{\mathbf{m}})\right) = \frac{2}{k_\parallel a} J_1(k_\parallel a)\,, \tag{D.2}$$

where a is the radius of the fracture, $k_\parallel$ the projection of the wavenumber change during the scattering onto the fracture plane, and J_1 the first order Bessel function. According to Equation (20.53) of Snieder (2009), the asymptotic development of the Bessel function is

$$J_m(x) = \sqrt{\frac{2}{\pi x}}\cos\left(x-(2m+1)\frac{\pi}{4}\right) + O(x^{-3/2})\,, \tag{D.3}$$

For the geometry described in Figure 5.3, the wavenumber change can be expressed as

$$k_\parallel = \frac{\omega}{\alpha}\left(\sin\theta(1+\cos\delta)+\sin\delta\cos\theta\right)\,. \tag{D.4}$$

Inserting Equations (D.3) and (D.4) into Expression (D.2), and expanding the cosine in exponentials gives

$$F(\mathbf{k}) \propto \left(e^{i\pi/4} e^{i\omega T} + e^{-i\pi/4} e^{-i\omega T} \right), \tag{D.5}$$

where $T = (a/\alpha)\left(\sin\theta(1+\cos\delta) + \sin\delta\cos\theta\right)$. T and $-T$ quantify the delay time of the tip diffraction arrivals relative to the arrival time $t = 2R/\alpha$ for a ray reflecting at the center of the fracture. Therefore, the total tip diffraction travel times for the scattered arrival are given by Equation (5.1). Note that this expression predicts a phase shift $\exp(\pm i\pi/4)$ for these waves that is characteristic of edge diffracted waves (Keller, 1978).